

KAUNAS UNIVERSITY OF TECHNOLOGY

IEVA BARAUSKIENĖ

**SYNTHESIS, STRUCTURE AND
ELECTROCHEMICAL PROPERTIES OF
COBALT OXIDE FILMS**

Doctoral dissertation
Physical Sciences, Chemistry (03P)

2018, Kaunas

This doctoral dissertation was prepared at Kaunas University of Technology, Faculty of Chemical Technology, Department of Physical and Inorganic Chemistry during the period of 2012–2018.

Scientific Supervisor:

Prof. Dr. Eugenijus VALATKA (Kaunas University of Technology, Physical Sciences, Chemistry, 03P).

Doctoral dissertation has been published in:

<http://ktu.edu>

Editor:

Armandas RUMŠAS (Publishing Office “Technologija”)

© I. Barauskienė, 2018

ISBN 978-609-02-1540-1

The bibliographic information about the publication is available in the National Bibliographic Data Bank (NBDB) of the Martynas Mažvydas National Library of Lithuania

KAUNO TECHNOLOGIJOS UNIVERSITETAS

IEVA BARAUSKIENĖ

KOBALTO OKSIDINIŲ DANGŲ SINTEZĖ,
STRUKTŪRA IR ELEKTROCHEMINĖS
SAVYBĖS

Daktaro disertacija
Fiziniai mokslai, chemija (03P)

2018, Kaunas

Disertacija rengta 2012–2018 metais Kauno technologijos universiteto Cheminės technologijos fakultete, Fizikinės ir neorganinės chemijos katedroje.

Mokslinis vadovas:

Prof. dr. Eugenijus VALATKA (Kauno technologijos universitetas, Fiziniai mokslai, Chemija, 03P).

Interneto svetainės, kurioje skelbiama disertacija, adresas:

<http://ktu.edu>

Redagavo:

Armandas RUMŠAS (leidykla „Technologija“)

© I. Barauskienė, 2018

ISBN 978-609-02-1540-1

Leidinio bibliografinė informacija pateikiama Lietuvos nacionalinės Martyno Mažvydo bibliotekos Nacionalinės bibliografijos duomenų banke (NBDB)

Contents

INTRODUCTION.....	8
1. Literature Review	10
1.1. Cobalt and Nickel Oxide Compounds	10
1.1.1. Cobalt (hydro)oxides	10
1.1.2. Nickel (hydro)oxides	14
1.1.3. Cobalt and Nickel Oxide Coatings Synthesis by Electrodeposition	15
1.2. Electrochemical Water Splitting	16
1.2.1. Basic Information about Hydrogen Production	16
1.2.2. Alkaline Water Electrolysis	17
1.2.3. Electrocatalysts for OER	18
1.2.4. Electrocatalytic Properties of Transition Metal Oxides	21
1.3. Electrochemical Capacitance	25
1.3.1. Basic Principles of Electrochemical Capacitance	25
1.3.2. Main Types of Electrochemical Supercapacitors	27
1.3.3. Determination of Capacitive Parameters	35
2. Experimental Part	37
2.1. Electrodeposition of Cobalt Oxide Coatings.....	37
2.2. Synthesis of Nickel-Cobalt Oxides	38
2.3. Analytical Techniques.....	38
2.3.1. Structure Analysis.....	38
2.3.2. Electrochemical Behavior.....	39
3. Results and Discussion	40
3.1. Structure and Electrochemical Behavior of Cobalt Oxide Coatings....	40
3.1.1. Synthesis of Cobalt (hydro)oxide Coatings by Electrodeposition ..	40
3.1.2. Structure Analysis of Cobalt Oxide Coatings.....	42
3.1.3. Electrochemical Behavior.....	47
3.2. Structure and Electrochemical Properties of Cobalt-Nickel Oxide Coatings.....	60
3.2.1. Electrochemical Synthesis of Layered Nickel-Cobalt (hydro)oxide.....	61
3.2.2. Structure Analysis of Nickel-Cobalt Oxide Coatings.....	67
3.2.3. Electrochemical Characterization	73

CONCLUSIONS	96
REFERENCES	98

Symbols and Abbreviations

b – Tafel slope constant
AAS – atomic absorption spectroscopy
a.u. – arbitrary units
CV – cyclic voltammetry
E – electrode potential
 e^- – electron
EDLC – electrochemical double-layer capacitor
EDS – energy dispersive X-ray spectroscopy
ESA – electroactive surface area
FT-IR – Fourier transform infrared spectroscopy
FTO – fluorine-doped tin oxide
GCPL – galvanostatic cycling with potential limitation
HER – hydrogen evolution reaction
I – current
j – current density
OER – oxygen evolution reaction
RHE – reversible hydrogen electrode
SEM – scanning electron microscopy
SMFF – sintered metal fiber filter
SS – stainless steel
TG-DSC – thermogravimetry and differential scanning calorimetry
XRD – X-ray powder diffraction
XPS – X-ray photoelectron spectroscopy
wt. % – weight percentage
 η – overpotential
 θ – Bragg diffraction angle
 λ – wavelength

Introduction

Relevance of the work. The ever increasing energy demands along with sustainable consumption and environmental concerns require searching for alternative energy sources. Hydrogen, as a clean fuel, is one of the most promising materials to fulfill all of these requirements, especially if synthesized during water electrolysis while using renewable energy. The oxygen evolution reaction (OER) is a half reaction of electrochemical water splitting coupled with hydrogen production. However, these reactions are kinetically sluggish in nature and typically require overpotential of thermodynamically calculated potential for water splitting (1.23 eV), therefore, an effective electrocatalyst is needed. So far, RuO₂ and IrO₂ are the most effective catalysts for OER, but the high price and limited natural sources lead to the search for alternative materials. The transition metal-based OER catalysts, especially cobalt and nickel containing spinel-type oxide, hydroxide and oxyhydroxide, are a reasonable choice due to their photo- and electrocatalytic activity in OER, good stability and relative abundance. α -cobalt and nickel oxide compounds having a layered structure with large interlayer spacing show not only significant catalytic activity in OER but are also distinguished with good pseudocapacitive properties. The ability to store energy by charge transfer between the electrode and the electrolyte arises from the Faradaic reactions occurring on the surface of the active material. As the surface area is one of the most important parameters in the design of electrocatalytic cells or supercapacitors, the formation of a 3D structure of the active substance on different conductive supports increases the activity in the oxygen evolution reaction as well as the specific capacitance. Electrodeposition, as an easy, environmentally friendly and relatively cheap synthesis technique, enables to form thin and evenly distributed layers of active materials having a large surface area.

The **aim of the work** was to synthesize cobalt oxide and nickel-cobalt oxide coatings on stainless steel and electroconductive glass substrates and to investigate their structure, morphology and electrochemical properties in aqueous solutions.

In order to achieve the aim, the following tasks had to be implemented:

1. To prepare nanostructured cobalt (hydro)oxide coatings on *Bekipor ST 20AL3* stainless steel mesh by electrochemical deposition and to investigate their structure and morphology;
2. To study the effects of the electrodeposition time and cobalt(II) precursor on the electrocatalytic activity in the oxygen evolution reaction and the capacitive behavior of the prepared cobalt (hydro)oxide coatings;
3. To form layered nickel-cobalt (hydro)oxide films on AISI304 stainless steel plates, *Bekipor ST 20AL3* stainless steel mesh and fluorine-doped tin oxide (FTO) glass by electrodeposition and to analyze their structure and composition;
4. To determine the influence of the synthesis conditions on the electrocatalytic activity and pseudocapacitive performance of the nickel-cobalt (hydro)oxide films.

Scientific novelty of the dissertation.

Cobalt (hydro)oxide and cobalt-nickel (hydro)oxide coatings on various substrates (3D stainless steel mesh, steel plates electroconductive glass) were formed via electrodeposition and characterized in a systematic way. The influence of synthesis parameters, such as the electrodeposition time, electrolysis bath composition and annealing temperature on the structure, composition, electrocatalytic activity and pseudocapacitive properties was investigated.

Practical significance of the dissertation.

The presented results are relevant for the practical application of earth-abundant metal (hydro)oxides in water anodic oxidation and charge storage devices. The prepared oxide materials were found to be promising candidates for the replacement of the most active but high-cost and relatively rare ruthenium and iridium compounds. It was demonstrated that Co_3O_4 on SS mesh and layered nickel-cobalt oxide films on AISI304 act as effective and stable electrocatalysts in OER, whereas nickel-cobalt oxide coatings on FTO glass demonstrate significant pseudocapacitive performance.

Approval and publication of research results.

The results of the research work are presented in 5 publications: 2 of them have been presented in journals included in the *Clarivate Analytics Web of Science* database, and 3 have been delivered in the proceedings of international and national conferences.

Structure and content of the dissertation.

The dissertation consists of the introduction, literature review, experimental part, results and discussion, conclusions, a list of references and a list of publications on the dissertation topic. The list of references includes 284 bibliographic sources. The main results are discussed on 117 pages and are illustrated in 16 tables and 56 figures.

Statements presented for the defense:

1. The electrochemical properties of cobalt (hydro)oxide coatings on *Bekipor ST 20AL3* depend on the cobalt(II) precursor used during electrodeposition.
2. The electrochemical activity of layered nickel-cobalt oxide coatings depends on the nature of the supporting substrate and their annealing temperature.
3. Annealed layered nickel-cobalt oxide coatings are more active in catalyzing the OER and storing charge than separate Co_3O_4 and NiO.

1. Literature Review

1.1. Cobalt and Nickel Oxide Compounds

1.1.1. Cobalt (hydro)oxides

Cobalt is one of the first-row transition metal elements of group VIII of the periodic table. Cobalt occurs in trace quantities in many rocks, soils, plants as well as in seawater and manganese-rich marine nodules. Pure metallic cobalt has few applications, but its use as an alloying element and as a source of chemicals makes it a strategically important metal [1]. Cobalt-containing alloys have many industrial applications, such as superalloys for aircraft engines, magnetic alloys for powerful permanent magnets, hard metal alloys for cutting tool materials, cemented carbides, wear-resistant alloys, corrosion-resistant alloys and electrodeposited alloys to provide wear and corrosion-resistant metal coatings [1]. Cobalt compounds are mainly used as pigments for glass, ceramic and paint industries, and also as catalysts in environmental applications [2]. The most important commercially available compounds are oxides, hydroxide, chloride, sulphate, nitrate, phosphate, carbonate, acetate and oxalate [1].

Cobalt hydroxide Co(OH)_2 . Two phases of cobalt hydroxide are reported in the literature: α - Co(OH)_2 and β - Co(OH)_2 . The pink β phase has a brucite-like layered hexagonal structure ($a=3.177 \text{ \AA}$, $c=4.653 \text{ \AA}$) with water molecules intercalated in the sheet structure $(\text{M(OH)}_2)_x(\text{H}_2\text{O})_x^{x+}$ [3,4]. Meanwhile, the structure of α - Co(OH)_2 is denoted by a net positive charge between brucite-like layers and the charge compensation balanced by anions, such as nitrate, carbonate, chloride in the interlayer space [3-5]. The net charge imbalance in α - Co(OH)_2 can be established by two mechanisms: hydroxyl deficiencies or polyvalent cobalt ions in the layers [6,7]. They are isostructural varieties of the hydrotalcite-like compounds [6,8]. Commercially, cobalt hydroxide is produced by employing the precipitation method from cobalt(II) salts solution with NaOH, although other methods do exist as well, such as sol-gel synthesis [9], chemical and physical vapor deposition [10,11], laser ablation [12], and electrochemical deposition [3,13,14]. Cobalt hydroxide shows relatively good catalytic and pseudocapacitive activity.

Cobalt oxide exists in two main types: grey cobalt(II) oxide CoO (75–78% of cobalt) and black cobalt(II) dicobalt(III) oxide Co_3O_4 (70–74% of cobalt). CoO is usually prepared by oxidizing the metallic cobalt above 1173 K, and then cooling it in a protective atmosphere to prevent partial oxidation to Co_3O_4 [1]. It has a cubic structure, dissolves only in strong acids, and absorbs a large amount of oxygen at room temperature. Co_3O_4 is a normal spinel containing Co^{2+} and Co^{3+} ions in tetrahedral and octahedral sites [2,15] with the general formula $\text{Co}^{2+}[\text{Co}_2^{3+}]\text{O}_4$. It is a p-type semiconductor presenting excellent redox properties and showing one of the lowest oxygen bond strength [16] and the highest rate of oxygen binding [2,17]. p-type semiconductors have deficiency of electrons in the lattice and conduct electrons by means of positive ‘holes’. These types of oxides are usually very active in catalytic applications [2,18]. The high reactivity of a p-type semiconducting metal is related to the straightforward adsorption of oxygen on their surface as electrons can be easily

removed from metal cations to form active species such as O^- [2]. The main industrial processes including cobalt oxides as catalysts are the removal of sulphur from various petroleum-based feedstocks (the process is called *hydrodesulfurization*), selective liquid-phase oxidation, catalytic combustion of alkanes, CO oxidation to CO_2 , oxidation of volatile organic compounds, activation of hydrocarbons at room temperature, and catalytic reduction of NO_x . Cobalt oxide compounds also show significant activity in the oxygen evolution reaction (OER) and, due to the ability to store charge, these compounds find their application as supercapacitors.

Co_3O_4 for environmental applications is usually prepared by using thermal decomposition of cobalt salts (nitrate or oxalate). Unfortunately, this method does not provide a sufficient surface area for catalytic applications. To solve this problem, some other methods are employed, such as the soft reactive grinding [19,20], solid state reaction [21], coprecipitation [22,23], the sol-gel method [24,25], the hydrothermal process [26,27], and electrochemical deposition [28,29].

In the course of implementing previous works [30,31], cobalt oxide coatings were prepared by using the galvanostatic electrodeposition method from an electrolyte consisting of 0.05 M $Co(CH_3COO)_2$ + 0.1 M KNO_3 . Mechanically and chemically stable cobalt hydroxide and cobalt oxide thin films were formed on AISI 304 stainless steel plates. The structure of as-deposited and annealed at 673 K coatings were investigated by conducting TG-DSC, XPS and FTIR analysis.

Fig. 1.1 shows thermogravimetric (TG) and differential scanning calorimetry (DSC) analysis results of an as-prepared cobalt hydroxide sample from cobalt acetate. The DSC curve reveals three endothermic effects in the temperature range of 323–620 K. They are accompanied by the weight loss of about 43%. The first endothermic effect at 323–433 K is due to the evaporation of physically adsorbed and interlayer water molecules. The endothermic effect at 470–535 K can be associated with the decomposition of the hydrotalcite-like structure of cobalt hydroxide. The third endothermic peak observed at 606 K can be related to the decomposition of intercalated CH_3COO^- groups. These results are consistent with the TG data reported in the scholarly literature [32,33].

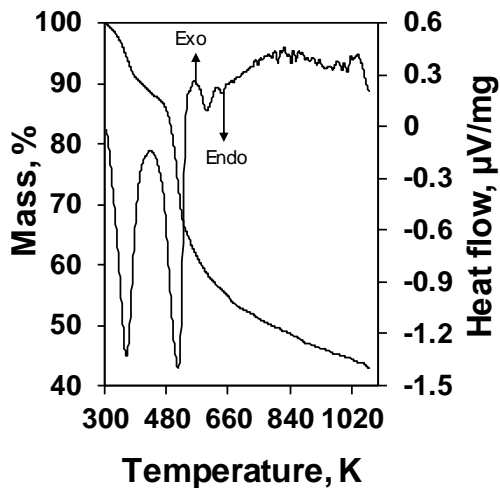


Fig. 1.1. TG–DSC patterns of deposited cobalt hydroxide deposited from acetate electrolyte [30]

The chemical composition of cobalt hydroxide and oxide films was characterized by using XPS. High resolution Co2p and O1s spectra were obtained for both films and are shown in Fig. 1.2. The quantification was performed in terms of O1s/Co2p ratio and was found to be 1.56 for the as-deposited sample and 1.35 for the annealed sample. The latter value was very close to the theoretical value of 1.33 for Co₃O₄. The Co2p region had doublets with a Co2p_{3/2} peak at 781.2 and 780.1 eV for as-deposited and annealed samples, respectively. The Co2p_{3/2} peak at 779.5–780.1 eV has previously been attributed to the Co₃O₄ phase of cobalt oxide [34,35], though its value is close to that of the CoO phase [36]. The Co2p_{3/2} peak at 780.7 eV, on the other hand, has previously been attributed to Co(OH)₂ [37].

Satellite peaks are also present in Co2p spectra for both samples, but they are of much lower intensity in the annealed sample than in the as-deposited one. The suppression of the shake-up satellite peaks was observed for the Co₃O₄ phase as opposed to the CoO phase [38], thus corroborating the previous attribution of Co₃O₄ to the annealed sample. Satellite peaks have also been observed to be more prominent in Co₃O₄ as opposed to Co(OH)₂ samples [37].

O1s spectra shown for both samples are comprised of several components. Namely, peaks at 530.1, 531.3 and 531.5 eV can be observed. These can be attributed to oxygen atoms in Co–O, Co(OH)₂ and adsorbed water [37]. The peak due to the cobalt-hydroxy bonds is the main peak in the as-deposited sample, whereas in the annealed sample it constitutes roughly 34% of all the O1s region. This, as well as the XPS spectral analysis of the Co2p region discussed above, unambiguously shows that the as-deposited sample is cobalt hydroxide, whereas the annealed sample is Co₃O₄ with some hydroxy groups adsorbed on the surface.

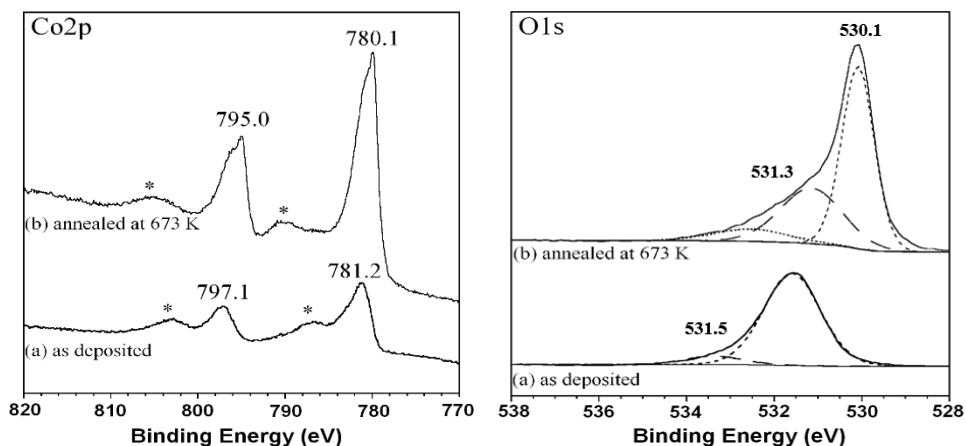


Fig. 1.2. High resolution XPS spectra of Co2p and O1s regions of (a) as-deposited and (b) annealed at 673 K films. The satellites in the Co2p spectrum are denoted with asterisks [30]

As-deposited and annealed samples of cobalt oxide coatings were investigated with Fourier transform infrared spectroscopy (Fig. 1.3). While analyzing the spectra of as-deposited cobalt hydroxide (Fig. 1.3, a), a wide absorption band in the high wavenumber region ($3600\text{--}3700\text{ cm}^{-1}$) where the peak at 3442 cm^{-1} is observed was related to the stretches of hydroxyl groups. The incorporation of acetate ions in the as-prepared samples can be confirmed by analyzing the intermediate wavenumber region having two absorption bands at 1578 and 1385 cm^{-1} which are attributed to the stretching C=O and C–O vibrations of the free acetate ions. The absorption band at 666 cm^{-1} can be ascribed to Co–OH vibrations. Other peaks at 1474 , 1020 and 458 cm^{-1} show the presence of CH_3 groups.

The FTIR spectrum of annealed cobalt hydroxide is shown in Fig.1.3, b. Two distinctive bands can be seen which are characteristic for cobalt oxide Co_3O_4 [39]. The first band at 565 cm^{-1} is associated with the Co(III) ions in the octahedral position, whereas the second band at 661 cm^{-1} is attributed to the Co(II) ions in the tetrahedral position. Small but wide absorption bands at 3422 and 1633 cm^{-1} can be assigned to the stretching and bending vibrations of hydroxyl groups, respectively. A small sharp absorption peak at 1384 cm^{-1} is associated with the vibrations of C–O groups and proves that small quantities of carbon compounds still remain after heat treatment.

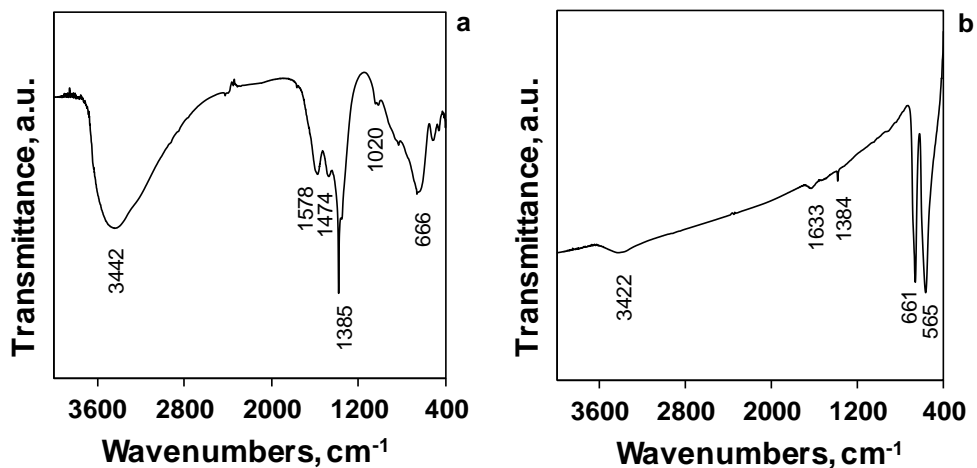


Fig. 1.3. FTIR spectra of as-deposited (a) and annealed at 673 K (b) cobalt oxide coatings [30]

1.1.2. Nickel (hydro)oxides

Nickel is one of the metals of the first row of VIII group in the periodic table. The great importance of nickel lies in its ability, when alloyed with other elements, to increase a metal's strength, toughness and corrosion resistance over a wide temperature range [40]. Nickel is widely used in the iron and steel industry; nickel-containing alloys are important constituents of materials in the aerospace industry. Nickel coatings are used to provide hard-wearing decorative and engineering coatings. Furthermore, nickel is a key part of several rechargeable battery systems, of which, the most important is nickel-metal hydride (NiMH). As a catalyst, nickel is used in the hydrogenation of vegetable oils and reforming of hydrocarbons, as well as in the production of fertilizers, pesticides and fungicides. Industrial cells for water splitting by electrolysis include nickel plates as catalysts for HER and OER [41].

Nickel hydroxide Ni(OH)₂. As well as cobalt hydroxide, nickel hydroxide exists in two known polymorphs: α -Ni(OH)₂ and β -Ni(OH)₂ [42]. The β phase is isostructural with brucite, Mg(OH)₂ [43]; it occurs naturally as the mineral *theophrastite* [42]. The α -phase consists of nickel hydroxide layers intercalated by water molecules [44]. The degree of hydration varies within the range of $0.41 \leq x \leq 0.7$ [43]. The interlayer spacing usually contains anionic impurities [42]. There are many methods to prepare nickel hydroxide materials according to the desired properties: phase, crystallinity, product morphology, and the general form [42]. In general, α -Ni(OH)₂ may be prepared by chemical precipitation [45], electrodeposition [46], sol-gel synthesis [47], hydrothermal [48] or solvothermal synthesis [49], microwave-assisted synthesis [50]. β -Ni(OH)₂ is usually produced by chemical ageing of alpha phase [51], and hydrothermal [52] or solvothermal synthesis [53]. Nickel hydroxide finds some use as an intermediate in the catalyst production, but its main use is as the active mass in the positive electrode in nickel-cadmium batteries [40].

Nickel oxide NiO is green, with a cubic rock-salt structure. It occurs in the nature as the mineral *bunsenite*. Nickel(II) oxide has a defect structure Ni_{1-y}O which is responsible for its p-type semiconductor properties [40]. The green nickel oxide can be produced by calcining nickel compounds (nitrate, oxalate, hydroxide) in air at 1273 K, whereas black nickel oxide is synthesized commercially by the calcination of nickel carbonate at 823 K, although other methods also exist [54], such as sol-gel synthesis [55], coprecipitation [56], microemulsion synthesis [57], hydrothermal reaction [58], as well as laser ablation [59]. Nickel oxide is used in the production of catalysts, in the enamel industry, glass and ceramics industries and in manufacturing ferrites for the electronics industry [40].

1.1.3. Cobalt and Nickel Oxide Coatings Synthesis by Electrodeposition

Although many methods of cobalt and nickel oxide coatings exist, electrodeposition is of great interest due to its relatively easy and accurate control of the surface microstructure of the deposited films by changing the deposition variables, such as the electrolyte, the deposition potential, or the bath temperature [60,61]. Electrochemical synthesis is performed by passing electric current between two or more electrodes separated by an electrolyte at the electrode/electrolyte interface [62]. It is a low temperature technique which is easy to perform, and inexpensive instruments are used.

Some of the most noteworthy works published lately investigate the properties of nickel-cobalt oxide coatings prepared by electrochemical methods. A composite of Ni-Co layered double hydroxide nanosheets on rGO/nickel foam was synthesized by cyclic voltammetry while applying the potential window of $0 \div -1.5$ V for 10 cycles [63]. The authors achieved a high value of the specific capacitance of $2133 \text{ F}\cdot\text{g}^{-1}$. The same cyclic voltammetry was used by Coviello *et al.* [64] with the objective to construct a composite of nickel-cobalt oxides, graphene and polyvinyl alcohol scanning in the potential window of $-0.45 \div +0.245$ V for 35 times. Pulsed electrodeposition was chosen by Adan-Mas *et al.* [65] to synthesize a complex of amorphous α -Ni-Co hydroxides and reduced graphene oxide on stainless steel in order to investigate their capacitive behavior (SC value $96 \text{ mAh}\cdot\text{g}^{-1}$). Unfortunately, the complex loses 38% of its capacitance after 5000 cycles. Galvanostatic electrodeposition was employed by Jiang *et al.* [66] to obtain a composition of nickel-cobalt layered double hydroxide on nickel foam@rGO substrate which demonstrated a specific capacitance of $125 \text{ F}\cdot\text{g}^{-1}$. Another electrochemical synthesis method – electrophoresis – was chosen by Balram, Zhang and Santhanagopalan [67] to deposit amorphous α -nickel-cobalt hydroxides on the stainless steel foil and nickel by applying the voltage of 200 V for 60 s. The obtained complex demonstrated reasonable activity in the oxygen evolution reaction with the overpotential of 255 mV. Despite the variety of electrochemical methods, potentiostatic deposition is one of the most commonly used techniques aiming to synthesize nickel-cobalt hydroxides [68-72] by applying one constant potential (usually the one between -0.85 and -1 V). Zeng *et al.* [73] deposited layered nickel-cobalt hydroxide from nitrosyl complexes at -1 V from separate cobalt and nickel electrolytes and obtained an SC value of $670 \text{ F}\cdot\text{g}^{-1}$.

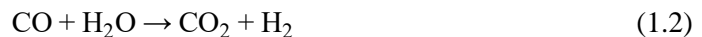
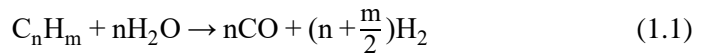
1.2. Electrochemical Water Splitting

1.2.1. Basic Information about Hydrogen Production

Hydrogen is the secondary form of energy produced by using three different energy supply system classes: fossil fuels (coal, petroleum, natural gas, shale oil), nuclear reactors and renewable energy sources (hydroelectric power, wind power, ocean thermal energy, biomass production, photovoltaic energy conversion, solar thermal systems) [74-77]. 96% of hydrogen is produced directly from fossil fuels whereas about 4% is produced indirectly by using electricity generated from fossil fuels [74]. As the climate change and the reduction of CO₂ concerns are increasing, ways of producing hydrogen without emitting greenhouse gases are urgently needed.

1.2.1.1. Hydrogen Production from Conventional Sources

The production of hydrogen from fossil fuels as a conventional source embraces three methods: (1) steam reforming from natural gas, (2) partial oxidation of hydrocarbons and (3) coal gasification [74,77]. At present, **natural gas steam reforming** today is the main path of hydrogen production. It is an endothermic catalytic process carried out in the temperature range of 970–1100 K and a pressure up to 3.5 MPa while using nickel as a catalyst [74]. The reaction involves two steps:



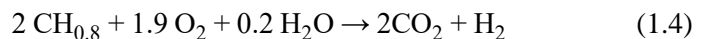
Although it is a relatively cheap and simple process, the emission of large quantities of CO₂ into the atmosphere and the usage of fossil fuels both in the production and as a heat source force scientists to develop more environmentally friendly H₂ production ways.

Partial oxidation of hydrocarbons is an exothermic reaction with oxygen and steam at a moderately high pressure with or without a catalyst according to the raw materials and process selected [74,77,78]. The basic reaction of the process is expressed as follows:



The disadvantage of the partial oxidation process is that it also emits carbon monoxide and carbon dioxide [74].

Another conventional H₂ production way is **coal gasification**. The basic reaction is as follows:

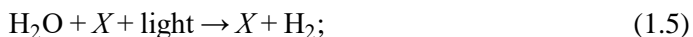


Production from coal is carried out by employing two methods: the synthane process and the CO₂ acceptor process. During the synthane process, CO, CO₂ and methane gases are formed as side products, and the purity of the produced H₂ is only 97–98%. Meanwhile, when using the CO₂ acceptor process, lime is included when coal reacts with steam, thus binding side-product CO₂ to calcium carbonate [74].

1.2.1.2. Hydrogen Production from Renewable Sources

Due to the finite life of fossil fuels and the global environment damage caused by fossil fuels, hydrogen generated from renewable sources is playing an important role as an energy carrier in the future energy supply [74,78-80]. Electrolysis is considered as the only process which does not need fossil fuels, generates a high-purity product and is feasible on small and large scales [74]. Carbon dioxide is emitted only when fossil fuels are used to generate the so-much-needed electricity. The emission can be reduced to zero by employing biomass, solar or wind energy. The three main energy sources for hydrogen production are as follows: (1) solar photovoltaic power, (2) wind power and (3) hydropower.

Solar energy can be exploited to produce hydrogen directly or as an energy source for electrolysis. When used directly, the ultraviolet radiation or the visible light of the appropriate wavelengths and intensity is absorbed by water molecules to liberate hydrogen gases:



Here, X is a photocatalyst, such as some compound salts, semi-conductor compounds, photosynthetic dyes, or photosynthetic bacteria.

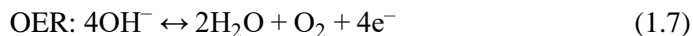
Solar energy can be used in the photovoltaic-electrolysis system called *photoelectrolyzer*, in which, sunlight is converted into electricity by photovoltaic cells, and hydrogen is produced by electrolysis.

Hydrogen can be produced by electrolysis while using **wind** turbines as the source of electricity. Of all the renewable energy sources, wind power is considered as having the greatest potential for producing pollution-free hydrogen [74]. Electricity production from **hydropower** is also the source of hydrogen production. This energy is further used in the splitting of water molecules when producing emission-free hydrogen [74].

The electrochemical decomposition of water into its constituents is reliable and clean. It is capable of producing ultra-pure (>99.999%) hydrogen. At 100% efficiency, 39 kWh of electricity and 8.9 liters of water are required to produce 1 kg of hydrogen at 25 °C and 1 atmosphere pressure [78]. The efficiency of a typical commercial electrolyzer is 56–73%. There are two basic types of low-temperature electrolyzers: the alkaline and the polymer electrolyte membrane [78].

1.2.2. Alkaline Water Electrolysis

The main advantage of alkaline water electrolysis over other water electrolysis technology lies in the fact that alkaline electrolyzers can be made of abundant and inexpensive materials: simple iron or nickel steel electrodes are used to produce hydrogen, and nickel is used to produce oxygen. The electrodes are immersed in a concentrated alkaline aqueous solution (usually, 6 M KOH), and a diaphragm that allows transportation of OH^- ions is placed between the anode and the cathode to effectively separate the produced gases thus avoiding the mixing of the electrolyte [41]. The alkaline water splitting reaction is composed of two half-reactions: the hydrogen evolution (HER) and the oxygen evolution (OER) reactions [81]:



At standard conditions, the equilibrium or the reversible potential for water electrolysis is 1.23 V. Generally, the accepted mechanisms for water oxidation include four electron transfer steps. Each electron transfer is coupled with a proton transfer [81]. Unfortunately, water electrolysis is greatly constrained by the kinetically sluggish OER because it is thermodynamically and kinetically unfavorable for the removal of four electrons to form the oxygen-oxygen double bond [82]. The OER intermediate products are stabilized by the catalysts, for example, surface-bound peroxy- or oxo-species. The relative stability of these intermediate complexes, and the activation barriers between them determine which step is rate-limiting and thus define the overall rate of water oxidation [81]. When explaining the basic working principles of OER catalysts, the Sabatier principle has become the generally acceptable theory [83]. The theory says that surface metal cations (M) are the active sites for the OER as the reaction proceeds through a series of intermediate products based on the bond M–O, e.g., M–OH, M–O, M–OOH, M–OO.

The best materials for the hydrogen evolution reaction (HER) are noble metals, such as platinum, palladium, rhodium or iridium. Trasatti [84] determined that, in acid solutions, Pt is distinguished for its best activity in the HER due to the highest strength of the M–H bond. As noble metals are prohibitively expensive, an alternative with a similar activity and lower costs is most appreciable. Kelly, Lee and Chen [85] synthesized an HER catalyst by supporting one monolayer of Pt on a molybdenum carbide (Mo₂C) substrate showing Pt-like activity and excellent stability. Low cost electrocatalysts for HER with high activity have been developed by using molybdenum disulphide MoS₂ [86,87], nanostructured WS₂ [88], nickel phosphide (Ni₂P) [89], cobalt sulphide [90], cobalt phosphide (CoP) [91], and graphitic-carbon nitride (g-C₃N₄) [92].

Compared to HER, OER is thermodynamically and kinetically unfavorable. Therefore, considerable research efforts have been devoted to the development and design of OER catalysts with the purpose to achieve high electrocatalytic activity and stability [82].

1.2.3. Electrocatalysts for OER

1.2.3.1. Metal Oxides

For the electrochemical water splitting by the catalyzing oxygen evolution reaction, it is convenient to classify the transition metal electrodes into three groups: (1) activated metal anodes (commonly known as Dimensionally Stable Anodes, DSA), (2) hydrous oxide electrodes and (3) bulk oxide/hydroxide electrodes [93].

Activated metal anodes consist of an underlying inert metal, such as titanium, coated with electrocatalytically active oxides of the platinum group metals, such as Ti-supported RuO₂ or Ru-based mixed oxide films [94,95]. For a long period of investigations, these noble metal oxides showed significant enhancements in the electrolytical activity over that of the bare metal; however, recently, various non-noble metal oxides, including spinels and perovskites have also received considerable

attention [94]. The oxide materials used in activated metal anodes are usually prepared by thermal decomposition using metal salts as precursors, mostly nitrates and chlorides. Oxides synthesized by this method have the rutile, perovskite or spinel structure, where oxygen is present only as a bridging species between two metal cations, and ideal crystals constitute tightly packed giant molecules [94]. The annealing temperature plays a highly important role when forming oxide films with good composition, morphology and electrocatalytic properties. The temperature should be sufficiently high to allow the decomposition of the metal salt to the corresponding metal oxide thereby minimizing chloride/nitrate impurities [94]. However, excessively high temperature values may initiate the transition between the different phases of the materials, e.g., at temperatures higher than 673 K, NiCo_2O_4 decomposes to NiO and Co_3O_4 [96]. Another relevant parameter to electrocatalytic properties is the surface morphology as Trasatti and his team established that the Tafel slope is highly dependent on the surface compactness [97,98]. Compact (or low defect) films demonstrated a Tafel slope of 40 mV dec^{-1} , whereas more defective (or less compact) films showed a Tafel slope of around 30 mV dec^{-1} . This regularity can be explained by a higher concentration of active sites due to the more defective or cracked morphology [94]. Although the thermochemical method is dominant, other synthesis techniques, such as sol-gel, attract much attention due to fewer residual impurities and enhanced service lifetimes [99].

Hydrous oxide electrodes are almost invariably prepared in aqueous environments, which results in more hydrated and dispersed materials where oxygen is present not just as a bridging species between the metal ions but also as O^- , OH and OH_2 species in the coordinated terminal group form [94]. Due to the presence of strand, layer, cage or tunnel structures which enable the molecules of the entire solvent to permeate the oxide or hydroxide phase, dispersion refers to the molecular level. In many cases, the materials when in contact with aqueous media contain significant quantities of loose water or/and electrolyte [94,100].

Hydrous oxides can be prepared by simple chemical precipitation or electrodeposition (when using potentiostatic or galvanostatic techniques). Although chemical precipitation is probably the simplest way to synthesize these materials, electrochemical deposition, especially potential cycling, is more versatile and convenient. In this method, the potential of an electrode of the parent metal, which may be noble or non-noble, is cycled repetitively between the suitable lower and upper limits in an aqueous solution of the appropriate pH which is often alkaline [94]. The oxide/solution interface of such oxide layers consists of an inner compact anhydrous layer MO_x and an outer microdispersed hydrous layer of the general form $\text{MO}_a(\text{OH})_b(\text{OH}_2)_c$ [101,102].

Bulk oxide/hydroxide electrodes have been extensively developed recently. Transition metal oxides based on nickel, cobalt, manganese and iron are considered as possible electrode materials for electrochemical supercapacitors as well as effective catalysts for the electrochemical oxidation of water. The term *bulk oxide/hydroxide electrode* refers to a metal oxide or hydroxide film deposited on a conducting substrate. The materials can be more compact than the hydrous oxide materials, but they often lack the long-range bonding order of the more crystalline materials used in

activated metal electrodes [94,103]. The preparation of this type of electrodes includes many different synthesis techniques, such as sol-gel processes [104], hydrothermal synthesis [105], chemical precipitation [106], vacuum evaporation [107], mechanical grinding [108], pyrogenation [109], electrostatic spray deposition [110], electron beam deposition [111], sputtering [112], and vapor deposition [113]. However, the simplest and the most versatile method is that of electrochemical deposition when the conducting substrate is coated with a metal oxide or hydroxide film either anodically or cathodically from an electrolyte solution containing the appropriate metal salt [94]. Various experimental techniques including potentiostatic [114], galvanostatic [115,116], potentiodynamic [117] and pulse deposition [116] have been used to synthesize different nanostructures, such as nanoparticles [118], nanoneedles [119], and nanorods [120].

If we consider the practical appearance, the discovery of a self-repairing mechanism operating at the neutral pH when the CoO_x cathodes are used in a phosphate (P_i) electrolyte renewed interest in metal oxides as water oxidation catalysts [121,122]. These complexes were referred to as ‘ CoP_i ’ although the role of the phosphate ions is structural as they help stabilize the CoO_x catalytic domains to avoid Co leaching [122,123] and facilitate rapid proton transfer [124] as well as improve the kinetics of the whole process [125]. CoP_i catalysts can be described as layered CoO_x with molecular dimensions that are stabilized in the neutral electrolyte by phosphate groups [126]. Nanostructured Co_3O_4 and $\text{Co}(\text{OH})_2$ exhibit enhanced catalytic performance by increasing the surface-to-volume ratio [127,128]. Marsh *et al.* [129] deposited a single cobalt monolayer on gold electrodes to obtain an effective electrocatalyst.

Thin catalyst films with electrocatalytic water oxidation properties similar to those of a Co-based catalyst can be electrodeposited from dilute Ni^{2+} solutions in borate electrolyte at pH 9.2 [130,131]. NiO_x Tafel behavior is unique due to exhibiting a 60 mV dec^{-1} slope at low overpotentials and a higher 120 mV dec^{-1} one at high overpotentials, which indicates a different mechanism [122,132]. This Tafel slope can be reduced by designing nanostructures [133].

Table 1.1 reveals important kinetic parameters of some metal oxide catalysts in the OER in alkaline media. It can be seen that FTO as a substrate has an advantage over GCE as the coatings on it demonstrate lower overpotentials.

Table 1.1. Kinetic parameters of some metal oxide electrocatalysts for OER in 0.1 M KOH (NaOH)

Active material	Substrate	Tafel slope, $\text{mV} \cdot \text{dec}^{-1}$	Overpotential at specific current density, mV	Ref.
CaFeO_3	GCE	47	390 at $10 \text{ mA} \cdot \text{cm}^{-2}$	[134]
SrFeO_3	GCE	63	410 at $10 \text{ mA} \cdot \text{cm}^{-2}$	
LaFeO_3	GCE	77	500 at $10 \text{ mA} \cdot \text{cm}^{-2}$	[135]
$\text{La}_{0.5}\text{FeO}_{3-\delta}$	GCE	48	400 at $10 \text{ mA} \cdot \text{cm}^{-2}$	
MnFe_2O_4	GCE	114	470 at $10 \text{ mA} \cdot \text{cm}^{-2}$	[136]
CoFe_2O_4	GCE	82	370 at $10 \text{ mA} \cdot \text{cm}^{-2}$	
NiFe_2O_4	GCE	98	440 at $10 \text{ mA} \cdot \text{cm}^{-2}$	
CuFe_2O_4	GCE	94	410 at $10 \text{ mA} \cdot \text{cm}^{-2}$	

Co ₃ O ₄ nanooctahedron	GCE	60	530 at 10 mA·cm ⁻²	[137]
Co ₃ O ₄ nanocube	GCE	60	580 at 10 mA·cm ⁻²	
LiCoO ₂	CFP	48	>520 at 5 mA·cm ⁻²	[138]
a-Fe ₃₆ Co ₆₄ O _x	FTO	40	270 at 1 mA·cm ⁻²	
a-Fe ₄₀ Ni ₆₀ O _x	FTO	34	250 at 1 mA·cm ⁻²	
a-Fe ₄₀ Co ₃₉ Ni ₂₂ O _x	FTO	40	280 at 1 mA·cm ⁻²	
a-Co ₄₁ Ni ₅₉ O _x	FTO	73	270 at 1 mA·cm ⁻²	

1.2.3.2. Carbon Nanotubes-Based Electrocatalysts

One of the practical issues associated with the application of metal oxides as electrocatalysts for water electrolysis is their relatively high resistance as most of the metal oxides are semiconductors [82,139]. One strategy is to combine the electronically conducting carbon materials, such as carbon nanotubes (CNTs), with metal oxides [82], such as NiO [140], Co₃O₄ [141], MnO_x [142]. CNTs have been studied as an excellent substrate material due to the high surface area, high conductivity and corrosion resistance. An important objective of metal oxide-CNTs hybrids is to functionalize CNTs with a suitable degree of functional groups for nucleating and anchoring nanocrystals without damaging the electronic properties [82]. Wu *et al.* [141] composed a hybrid of Co₃O₄ nanocrystals on single-walled CNTs by mixing cobalt oxide, CNTs and toluene. The developed hybrid showed enhanced catalytic activity and superior stability for OER in neutral and alkaline electrolytes compared to bare Co₃O₄ which performs well in alkaline solutions. An important target for metal oxide-CNTs hybrids is to functionalize CNTs with a suitable degree of functional groups for nucleating and anchoring nanocrystals without damaging their electronic properties [82]. Lu and Zhao [143] densely and strongly anchored crystalline cobalt oxide nanoparticles onto mildly oxidized multi-walled carbon nanotubes (Co₃O₄/mMWCNT) and applied them as electrocatalysts for highly efficient water oxidation. This complex showed a high Faraday efficiency and long-term stability as well as excellent electrocatalytic performance.

Recently, heteroatom doped carbon materials have been investigated as potential metal-free OER catalysts [82]. Zhao *et al.* synthesized nitrogen-doped carbon nanomaterials for OER in the alkaline media and obtained a low overpotential value and good stability [144]. Graphitic carbon nitride (g-C₃N₄) hybridized with CNTs was designed by Chen *et al.* [145] by using cyanamide as the precursor. Ma *et al.* developed graphitic carbon nitride nanosheet-carbon nanotubes three-dimensional porous composites as high-performance OER catalysts [146]. Nitrogen and oxygen dual-doped graphene-CNT hydrogel film was synthesized by Chen *et al.* [147]; it was exhibiting high OER activity, which has been attributed to the dual active-sites mechanism originating from the synergy of the chemically converted graphene and CNTs.

1.2.4. Electrocatalytic Properties of Transition Metal Oxides

1.2.4.1. Interfacial Redox Chemistry of Transition Metal-Based Electrodes in Alkaline Solution

Generally, the mechanism of redox reactions occurring on the surface of transition metals in alkaline solutions is complex. Redox switching in this sense refers to the potential-induced change in the oxidation state of linked oxy-metal groups which constitute the metal oxide film [94]. The charge storage and the supercapacitive behavior of transition metal oxides arises from various redox transitions which depend on a range of factors: the composition and the structure of the oxide, the preparation method and the available oxidation states of the metal [94]. When exploring the metal oxide redox chemistry, the surface oxy groups are known to hydrate or hydroxylate in an aqueous solution [148,149]. When immersed into aqueous alkaline solutions, the metal oxide surface becomes hydrophilic; the solvent molecules can become bonded to the metal cations, which results in the transfer of a proton to a neighboring oxygen site [94]. Therefore, the surface oxy groups, termed *surfaquo groups*, can become extensively hydrated or hydroxylated and undergo rapid redox transformations involving simultaneous loss or gain of electrons, protons and hydroxide ions [94].

The interfacial redox chemistry of **nickel hydroxide** is one of the most extensively studied systems in electrochemistry. It is a complex and variable system with many depending factors, such as electrode preparation and history, therefore its analysis is complicated [94]. The oxygen evolution on the nickel (hydro)oxide surface is dictated by the redox processes Ni(II)/Ni(III) occurring in the anodic potential area [94]. Bode, Dehmelt and Witte [44] described the redox behavior of Ni(II)/Ni(III) in terms of four phases, as shown in Fig. 1.4. The discharged or reduced Ni(OH)₂ material can exist as a largely anhydrous phase designated as β-Ni(OH)₂ or as a hydrated phase denoted as α-Ni(OH)₂. The oxidation of the β-Ni(OH)₂ material is predicted to produce a phase referred to as β-NiOOH, while the oxidation of the α-Ni(OH)₂ produces γ-NiOOH [94]. Therefore, two distinct oxidation/reduction transitions exist: β/β and α/γ [94].

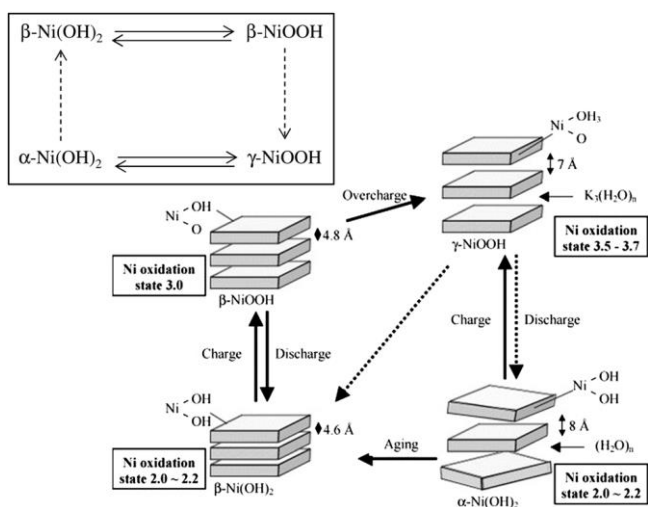


Fig. 1.4. Schematic representation of the Bode cycle for the Ni(II)/Ni(III) redox transition in Ni hydroxide layers [94]

The mechanism of interfacial redox reactions of cobalt-based electrodes in alkaline solutions was also studied by Bode, Dehmelt and Witte [44] and is presented in Fig. 1.5. In an analogous manner to the situation for divalent Ni hydroxides, both hydrous α -Co(OH)₂ and largely anhydrous β -Co(OH)₂ exist as well: the α phase contains excess H₂O and has an approximate composition range of Co(OH)₂·0.9–1.4H₂O [94]. When oxidised by anodic polarisation, Co(OH)₂ is transformed to a phase similar to the γ -NiOOH, meanwhile chemical oxidation in air yields the formation of β -CoOOH [150].

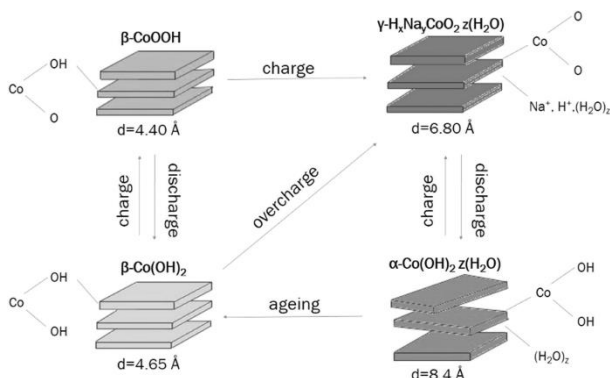


Fig.1.5. Bode scheme of squares for cobalt hydroxides and oxyhydroxide species [151]

1.2.4.2. Mechanism of OER

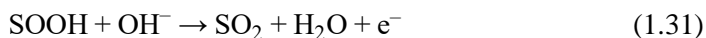
Considerable research efforts have been devoted to determining the exact mechanism of the oxygen evolution reaction at the transition metal oxide surfaces. The major difficulties lie in the fact that OER is a complex process involving the transfer of four electrons [94]. Table 1.2 presents the five most common OER mechanistic pathways. The kinetic parameters such as Tafel slopes are not unique for a given pathway; therefore, it is fairly complicated to predict the possible mechanism for a particular system. Furthermore, the surface coverage of the reaction intermediates may vary with the potential, further making the thermodynamic and kinetic analysis of the OER more complex [94].

Bockris and Otagawa [152,153] suggested that the catalytic activity of the active materials in OER correlates with the surface bond energy of OH. According to the authors, the rate determining step might be the desorption of OH or oxygenated species from the surface, and the regularity exists in the sense that the weaker the metal-OH bond is, the greater is the rate of desorption at a given overpotential [94]. Rossmeisl *et al.* [154] proposed the surface binding energy as a suitable descriptor for the OER activity with the formation of a surface adsorbed OOH species being rate determining at rutile-type oxides, such as RuO₂, IrO₂ and TiO₂. In terms of interpreting mechanisms from the molecular point of view rather than the solid state point of view, similar intermediate species, such as M–OH, M=O, M–OOH (where M is a catalytically active metal center), are proposed to participate [155,156].

Table 1.2. The most common mechanisms of OER

OER pathway	Mechanism
Bockris's oxide path [152,153]	$M + OH^- \rightarrow MOH + e^-$ (1.8)
	$2MOH \rightarrow MO + M + H_2O$ (1.9)
	$2MO \rightarrow 2M + O_2$ (1.10)
Bockris's electrochemical path [152,153]	$M + OH^- \rightarrow MOH + e^-$ (1.11)
	$MOH + OH^- \rightarrow MO + H_2O + e^-$ (1.12)
	$2MO \rightarrow 2M + O_2$ (1.13)
Krasil'shchikov's path [94]	$M + OH^- \rightarrow MOH + e^-$ (1.14)
	$MOH + OH^- \rightarrow MO^- + H_2O$ (1.15)
	$MO^- \rightarrow MO + e^-$ (1.16)
	$2MO \rightarrow 2M + O_2$ (1.17)
O'Grady's path [94]	$M^z + OH^- \rightarrow M^zOH + e^-$ (1.18)
	$M^zOH \rightarrow M^{z+1}OH + e^-$ (1.19)
	$2M^{z+1}OH + 2OH^- \rightarrow M^z + H_2O + O_2$ (1.20)
Kobussen's path [157,158]	$M + OH^- \rightarrow MOH + e^-$ (1.21)
	$MOH + OH^- \rightarrow MO + H_2O + e^-$ (1.22)
	$MO + OH^- \rightarrow MO_2H^-$ (1.23)
	$MO_2H^- + OH^- \rightarrow MO_2^- + H_2O + e^-$ (1.24)
	$MO_2^- \rightarrow M + O_2 + e^-$ (1.25)

Although there are many mechanisms of metal hydroxide/oxide participation in OER, the following general mechanism was proposed to rationalize the OER kinetic data observed for metal hydrous oxide films in an alkaline solution [93,132]:



Here, *S* represents a *surfaquo* group attached to the hydrous oxide surface by bridging oxygen ligands [94]. A schematic illustration is presented in Fig. 1.6. Octahedrally coordinated oxymetal *surfaquo* groups are identified as the catalytically active species and are located within the hydrous layer. This layer contains considerable quantities of water molecules which facilitate the hydroxide ion discharge at the metal catalytic site [94,154].

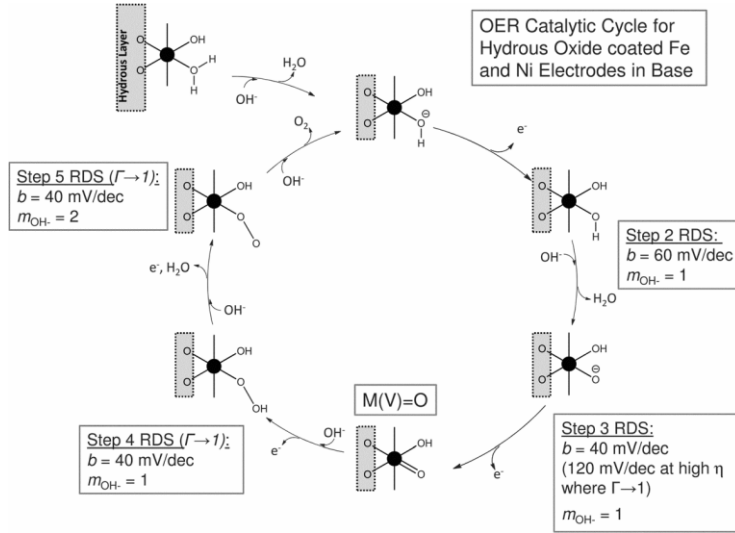


Fig.1.6. Mechanism for the OER at hydrous oxide coated Fe and Ni electrodes in alkaline solution [94]

1.3. Electrochemical Capacitance

1.3.1. Basic Principles of Electrochemical Capacitance

A conventional capacitor consists of two conducting electrodes (plates) separated by a dielectric material [159,160]. The capacitor is charged by applying voltage across the electrodes: this causes positive and negative charges to migrate toward the surface of electrodes of the opposite polarity. When charged, a capacitor will act as a voltage source for some time connected in a circuit [159]. One of the main parameters of the capacitor is its capacitance (C), measured in Farads (F), and described as the ratio of the electric charge in each electrode (Q) to the potential difference between them (V):

$$C = \frac{Q}{V} \quad (1.33)$$

The capacitance of a conventional capacitor is proportional to the surface area of each electrode (A) and inversely proportional to the distance between them (D):

$$C = \frac{\epsilon_0 \epsilon_r A}{D} ; \quad (1.34)$$

Here, ϵ_0 is the dielectric constant (or permittivity) of free space, and ϵ_r is the dielectric constant of the insulating material between the electrodes.

Along the specific capacitance, energy density and power density are the main quantitative parameters, both of which can be expressed as a quantity per unit mass (specific energy and specific power) or per unit volume. The energy (E) is directly proportional to the specific capacitance, and its highest value is achieved when the potential difference V is at its maximum which is usually limited by the breakdown strength of the dielectric [159]:

$$E = \frac{1}{2} CV^2 \quad (1.35)$$

Power (P), in general, is the rate of energy delivered per time unit. To determine this parameter for a certain capacitor, the resistance of the internal components (electrode materials, dielectric separators, and electrolyte) must be taken into account. The resistance is usually measured in aggregate and referred as the equivalent series resistance (ESR). The ESR determines the highest voltage of the capacitor during discharge and therefore limits the maximum energy and power of a capacitor. The measurement of power for capacitors is often measured at matched impedance, which corresponds to the maximum power P_{max} , given by [159]:

$$P_{max} = \frac{V^2}{4ESR} \quad (1.36)$$

The conventional electrostatic capacitor is denoted by relatively high-power density and can deliver the energy very quickly; however, its energy density is rather low comparing with that of the electrochemical battery which can store more energy but, on the other hand, cannot provide a high-power impulse. This means that its power density is relatively low. Supercapacitors (or ultracapacitors) are governed by the same principles as conventional capacitors, but they incorporate electrodes with a much higher surface area (up to $2500 \text{ m}^2 \cdot \text{g}^{-1}$) and thinner dielectrics which are defined by the thickness of the double layer (approx. 0.1 nm). Moreover, by maintaining the low ESR characteristic, supercapacitors are able to achieve significant values of power density. Therefore, supercapacitors have several advantages over batteries and fuel cells, such as a higher power density, a shorter charging time ($\sim 0.6 \text{ s}$), a longer lifecycle ($\sim 10^6$) and a longer shelf life [161-163]. The performance advantages of supercapacitors are presented in a Ragone plot (Fig. 1.7) and in Table 1.3.

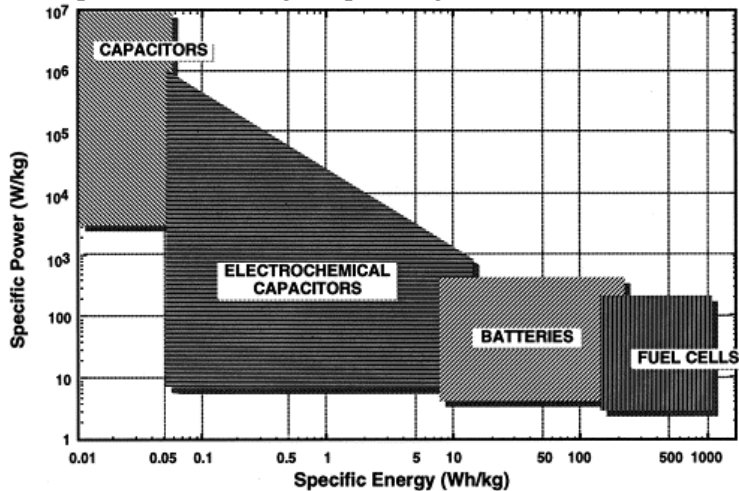


Fig. 1.7. Ragone plot of energy storage devices [163]

Table 1.3. Comparison of quantitative characteristics of typical capacitor and battery [159]

Characteristics	Capacitor (Al, Ta oxide, condenser)	Carbon EDLC (activated carbon)	Battery (lead acid, Ni-Cd, Ni-MH)
Storage mechanism	Electrostatic	Electrostatic	Chemical
E (Wh·kg ⁻¹)	<0.1	1–10	~20–150
P (W·kg ⁻¹)	>>10 000	500–10 000	<1000
Discharge time (t_D)	10 ⁻⁶ –10 ⁻³ s	Seconds to minutes	0.3–3 h
Charging time (t_C)	10 ⁻⁶ –10 ⁻³ s	Seconds to minutes	1–5 h
Efficiency (t_D/t_C)	~1.0	0.85–0.99	0.7–0.85
Cycle life (cycles)	>>10 ⁶	>10 ⁶	~1500

1.3.2. Main Types of Electrochemical Supercapacitors

Electrochemical capacitors (ECs) are based on charging and discharging at the electrode-electrolyte interface of high surface materials, such as porous carbons, conductive polymers or some metal oxides. There are two distinctly different charge mechanisms of ECs to develop capacitance: electric double-layer capacitance through electrostatic charge development between the electrode/electrolyte interfaces, and pseudocapitance developed from highly reversible Faradaic reactions occurring at specific potentials [163,164]. The resulting capacitors are called electric double-layer capacitors (EDLCs) and pseudocapacitors. The systems incorporating combinations of a double layer and pseudocapitance are called hybrid capacitors.

1.3.2.1. Electric Double-Layer Capacitors

The concept of the double layer has been under development since the nineteenth century when German physicist Hermann von Helmholtz first modeled and introduced the double-layer conception in his work on colloidal suspensions in *Annals of Physics* in 1853. The first commercial double-layer supercapacitors, presented in 1970, consisted of carbon paste electrodes formed by soaking porous carbon in an electrolyte separated by an ion-permeable separator. Carbon is still the most commonly used active material in commercial devices due to its low cost and availability; however, research and development is highly focused on creating new electrode materials, such as graphene, mesoporous or hierarchical templated carbons, and carbon nanotubes.

The capacitance of EDLCs arises from the electrostatic charges accumulated from the electrolyte/electrode interface, and their storage mechanism is based on charge separation similar to a traditional capacitor. However, EDLCs can store considerably more energy due to the increased surface area and the small thickness of the double layer at the interface of the electrode/electrolyte. A typical EDLC is composed of two electrodes immersed in an electrolyte which are separated with an ion-permeable layer located between the electrodes to avoid electrical contact (Fig. 1.8). In the charge state, the electrolyte anions and cations move toward the positive and negative electrodes, respectively, thus giving rise to two double layers, one at each electrode/electrolyte interface. The separation of ions results in a potential

difference across the cell. As each electrode/electrolyte interface acts like a capacitor, the whole cell can be considered as two capacitors connected in a series [159].

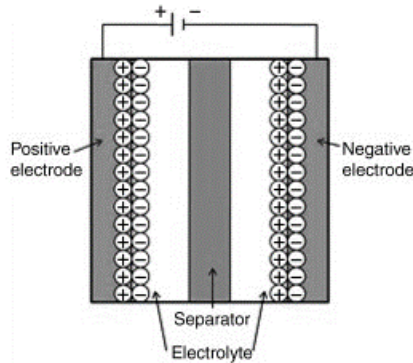


Fig. 1.8. An electrochemical double-layer supercapacitor [165]

A capacitive performance of an electrochemical double-layer capacitor is affected by a number of factors, from which, the most important ones are a high surface area, high electrical conductivity and distribution of pores of a controlled size, ideally chosen to match the size of the electrolyte ions to minimize the thickness of the double layer [164]. The types of electrolytes that can be used in EDLCs can be classified into three groups: (1) aqueous, (2) salts dissolved in organic solvents, and (3) ionic liquids. Aqueous electrolytes are distinguished by high conductivity, low viscosity, low costs and low toxicity; however, their electrochemical window usually does not exceed 1 V. A low value of the cell voltage poses a significant limitation if targeting high energy. Nevertheless, the higher conductivity of aqueous electrolytes reduces the internal resistance of the device and maximizes its specific power [159].

Nonaqueous electrolytes of various types allow the use of cell operating voltages up to 2.7 V [159,161,166]. The specific energy of supercapacitors is proportional to the square of the operating voltage; therefore, nonaqueous high-voltage devices are attractive for high-energy applications. The most common organic electrolyte for EDLCs is an alkyl ammonium salt dissolved in an aprotic solvent. However, nonaqueous electrolytes have some disadvantages, such as low conductivity, medium or high viscosity, higher costs and higher toxicity comparing to aqueous electrolytes.

While both aqueous and nonaqueous (or organic) electrolytes are commonly used in the market, the commercial application of the third group – ionic liquids – is still limited [167,168]. Ionic liquids (ILs) are a class of organic salts in which the ions are poorly coordinated, which results in these solvents being liquids at relatively low temperatures (<100 C or even at room temperature). Ionic liquids are promising alternatives to organic solvents in nonaqueous EDLCs as they help to avoid the flammability and volatility concerns of organic solvents. The operating voltage of ILs can reach 3–6 V, however, despite their advantages, the low conductivity and high viscosity complicates the commercial usage of this kind of electrolytes [159].

An important consideration when selecting an electrolyte for a porous material is the size of the electrolyte ions as they need to be able to access the electrode porosity

[159]. As mentioned above, to achieve the highest values of capacitance, the size of the pores should match the size of the electrolyte ions. Aqueous electrolytes often feature a smaller ion size than organic solvents or ionic liquids, therefore, they provide generally higher values of specific capacitance.

1.3.2.2. Pseudocapacitors

Some materials employ fast and reversible redox reactions at their surface. This phenomenon represents a different kind of capacitance contribution to double-layer capacitance [161]. This capacitance is not electrostatic in its origin; therefore, the prefix ‘pseudo’ is used. The charge in this kind of materials is stored due to the occurring Faradaic reactions on the electrode/electrolyte interface. This is accomplished through electrosorption, oxidation-reduction reactions and intercalation processes [161]. These Faradaic processes may allow pseudocapacitors to achieve greater capacitances and energy densities than EDLCs [169-171]. The most commonly investigated classes of pseudocapacitive materials are the transition metal oxides (RuO_2 , NiO , MnO_2 , Co_3O_4) and conducting polymers (polyaniline, polypyrrole).

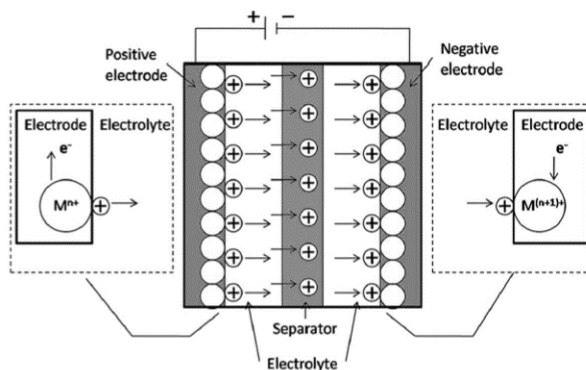


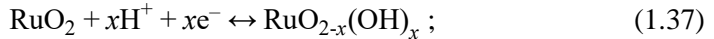
Fig. 1.9. A pseudocapacitor [165]

1.3.2.2.1 Metal oxides/hydroxides

Transition metal oxides and hydroxides, such as RuO_2 , MnO_2 , $\text{Ni}(\text{OH})_2/\text{NiO}_x$, $\text{Co}(\text{OH})_2/\text{Co}_3\text{O}_4$, and Fe_3O_4 , have a number of properties making them suitable for use as pseudocapacitors. They undergo fast reversible oxidation-reduction reactions at their surface while showing a strong pseudocapacitive behavior exceeding the double-layer capacitance achieved with carbon materials. The development of pseudocapacitors has been driven by the desire to increase the specific energy of the conventional EDLCs while retaining a comparably high power and the long-term cyclability of EDLCs. However, as their charge storage mechanism is based on the redox processes similar to those of batteries, these materials can also suffer from low a power density and a poor life cycle [159]. The low power density can be related to the poor electric conductivity of these materials, which decreases the electron transfer rates. Furthermore, the negative effect on the morphology caused by the swelling and shrinkage of the electrode materials during the charge/discharge processes leads to the lack of cycling stability. Therefore, in order to solve these problems, two main

methods involve combining metal oxides/hydroxides with conductive materials and developing porous nanostructures. The former can accelerate the reaction kinetics while the latter can buffer the stress from the swelling and shrinkage of the electrodes and provide more ion adsorption or active sites for the charge transfer reactions, as well as shorten the diffusion and transfer pathways of the electrolyte ions [172]. Selected materials and configurations are briefly discussed below.

Ruthenium oxide RuO₂ is recognized as one of the most promising electrode materials due to its high theoretical capacitance ($>1300 \text{ F}\cdot\text{g}^{-1}$), long cycle life, wide potential window, high electric conductivity, good thermal stability, long cycle life and high rate capability [172-174]. The pseudocapacitive behavior of RuO₂ in an acidic electrolyte comes from a highly reversible Faradaic reaction, according to the equation:



Here, $0 \leq x \leq 2$ [172]. In the acidic system, the oxidation states of ruthenium change from (II) to (IV). When the alkaline electrolyte is used, the oxidation states are different. Despite all the advantages, the high cost and toxicity of ruthenium has limited the utilization of RuO₂ in commercial devices. To reduce the costs, RuO₂ is often coupled with other metal oxides, such as SnO₂, MnO₂, NiO, TiO₂ and CaO to form composite oxide electrodes. Ideally, ruthenium should be replaced with these metal oxides, and recent studies indicate that these oxides are indeed promising alternatives for high performance capacitor applications [173].

Manganese oxide MnO₂, generally, offers relatively low cost, low toxicity and environmental safety, as well as a high theoretical capacitance up to $1300 \text{ F}\cdot\text{g}^{-1}$ [174]. The capacitance of manganese oxides mainly comes from pseudocapacitance. There are two suggested mechanisms to explain the MnO₂ charge storage behavior. The first one implies the adsorption of electrolyte cations (such as $C=\text{Li}^+, \text{Na}^+, \text{K}^+$) according to the following equation [175,176]:



The second reaction is based on the insertion of electrolyte cations into the bulk of the electrode [172]:

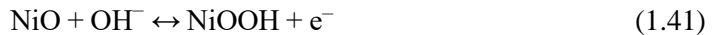
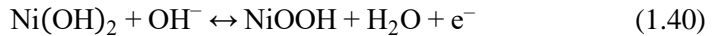


The synthesis of manganese oxides is largely performed by chemical [177,178] and electrochemical means [179] while using a variety of precursors [164]. The pseudocapacitive performance of MnO₂ is affected by both physical (microstructure and surface morphology) and chemical (the valence and the hydrous state of the oxide) factors [174]. To avoid the development of resistive aggregated particles and to provide a means of controlling the thickness of the film, electrodeposition has been proposed to be a superior method to obtain MnO₂ films [164].

Although the theoretical specific capacitance of MnO₂ is quite high, the practical values of unmodified MnO₂ are usually lower than $350 \text{ F}\cdot\text{g}^{-1}$ [172]. This is related to the poor electric conductivity and electrochemical dissolution during cycling. In order

to improve the conductivity and the charge storage capability, not only the incorporation of other metal elements into MnO₂ compounds but also the composing of MnO₂ nanostructured composites with well-conductive materials are feasible ways [172]. Cobalt doping can prevent the dissolution of MnO₂, vanadium doping can inhibit the crystal growth of MnO₂ and iron doping can improve the cycle stability due to the reduction of the concentration of unstable Mn³⁺ ions [180]. Based on the method, various composites with MnO₂ were synthesized, such as MnO₂/carbon nanotubes [181,182], MnO₂/graphene [183], MnO₂/carbon nanofibers [184], MnO₂/nanoporous gold [185], polyaniline-MnO₂ nanotubes [186]. Chen *et al.* constructed nanostructured MnO₂-carbon nanotube-sponge hybrid electrodes which achieved a specific capacity of 1230 F·g⁻¹ and were distinguished by excellent cycle stability as the degradation was only 4% after 10 000 cycles [187].

Nickel hydroxide and oxide Ni(OH)₂/NiO are promising materials for pseudocapacitors due to their ultrahigh theoretical capacitance (3650 F·g⁻¹ for Ni(OH)₂ and 3750 F·g⁻¹ for NiO), low costs and environmental friendliness [172]. The charge storage mechanism is based on the occurring Faradaic reactions according to the following equations involving Ni(OH)₂ (1.40) and NiO (1.41):



It is recognized that the electrochemical surface reactivity of nickel oxide is strongly dependent on its crystallinity [174]. As Cheng, Cao and Yang [188] determined in their work, the calcination temperature can significantly affect the crystalline structure of NiO_x, the value of *x* and the specific capacitance. At above 553 K, more crystallization takes place, and the value of *x* decreases. As a result, the highest specific capacitance of 696 F·g⁻¹ can be achieved at 523 K. The capacitance decreases significantly when the annealing temperature is over 573 K [174]. To improve the unsatisfactory porous structures of Ni oxides which can complicate the transportation of electrolyte ions, nickel oxide with its hierarchical porous texture, nanostructured NiO materials (nanobelts, nanorods, nanowires, nanoflowers) or nickel oxide composites with other materials have been developed. Porous NiO with macropores synthesized during electrophoresis and electrodeposition are denoted by much larger specific capacitance than the bare NiO film as they even reached 351 F·g⁻¹ [189]. Xia *et al.* [190] developed a hierarchically porous NiO film by chemical bath deposition with a colloidal crystal template and reached a SC of 309 F·g⁻¹ with a capacitance retention of 89% after 4000 cycles. Composing NiO with carbon materials or porous metals can efficiently enhance the electric conductivity, surface area and excellent rate capability [172]. Nam *et al.* [191] prepared the NiO_x/CNT (carbon nanotube) electrodes via electrochemical deposition with an ultrahigh SC value of 1701 F·g⁻¹. This value, achieved with 8.9 wt% NiO in the composite electrode, significantly drops to 671 F·g⁻¹ when the percentage of NiO is increased to 36.6%. This decrease can be attributed to high equivalent series resistance (ESR) for heavier deposits and a poorer ionic transportation stemming from the reduced pore size and pore clogging [172].

Ni(OH)_2 is a hexagonal-layered structure which has two polymorphs: $\alpha\text{-Ni(OH)}_2$ and $\beta\text{-Ni(OH)}_2$ corresponding to γ - and $\beta\text{-NiOOH}$ after oxidation [192-194]. $\alpha\text{-Ni(OH)}_2$ is a hydroxyl-deficient phase with interlayered anions and water molecules while $\beta\text{-Ni(OH)}_2$ possesses a brucite structure without water molecules [172]. The specific capacitance of the $\alpha\text{-Ni(OH)}_2/\gamma\text{-NiOOH}$ couple is higher than that of the $\beta\text{-Ni(OH)}_2/\beta\text{-NiOOH}$ couple due to the greater change in valence [195,196]. As the theoretical SC values of Ni(OH)_2 and NiO are quite similar, the practical values differ significantly as Ni(OH)_2 shows prominently higher capacitive abilities. The values of SC depend on the physical form of Ni(OH)_2 as well because powdered materials usually exhibit $500\text{--}600 \text{ F}\cdot\text{g}^{-1}$, and modified films can reach $3000 \text{ F}\cdot\text{g}^{-1}$, which is very close to their theoretical value. Yang, Xu and Li [197] formed porous $\alpha\text{-Ni(OH)}_2$ on Ni foam by electrodeposition and reached $3152 \text{ F}\cdot\text{g}^{-1}$ at $4 \text{ A}\cdot\text{g}^{-1}$, but the SC drops quickly as the current density increases. A $\text{Ni(OH)}_2/\text{graphene}$ electrode synthesized by Wang *et al.* [198] demonstrated $1335 \text{ F}\cdot\text{g}^{-1}$ specific capacitance at $2.8 \text{ A}\cdot\text{g}^{-1}$ with a good rate capability. Chen *et al.* [199] presented a composite of $\alpha\text{-Ni(OH)}_2$ nanosheets doped with low defect density carbon nanotubes (CNTs) synthesized via a facile soft chemistry route. This composite demonstrated a high specific capacitance of $1302 \text{ F}\cdot\text{g}^{-1}$, while individual components reached only $372 \text{ F}\cdot\text{g}^{-1}$ for Ni(OH)_2 and $101 \text{ F}\cdot\text{g}^{-1}$ for CNTs.

Despite all the advantages of nickel hydroxide and oxide, some issues, such as poor cycle performance and high resistivity (low electric conductivity), must be solved in order to compose more efficient materials with higher capacitive parameters. The conductivity of nickel oxide can be improved by introducing cobalt ions into the nickel oxide matrix [174].

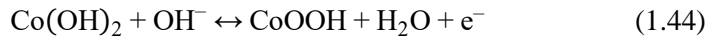
Cobalt hydroxide and oxide $\text{Co(OH)}_2/\text{Co}_3\text{O}_4$. Cobalt oxide Co_3O_4 has the spinel structure AB_2O_4 belonging to the cubic system [172]. Due to its advantages, such as the excellent reversible redox behavior, a large surface area, high conductivity, long-term performance and good corrosion stability, it has been considered as an alternative electrode material for electrochemical supercapacitors [200,201]. The theoretical value of specific capacitance of cobalt oxide is similar to that of NiO and reaches $3650 \text{ F}\cdot\text{g}^{-1}$. Furthermore, Co_3O_4 features a better cycle stability than NiO as well as good corrosion resistance [202,203]. The pseudocapacitance of Co_3O_4 arises from reversible oxidation/reduction reactions according to the following equations [204]:



Cobalt oxide Co_3O_4 is a *p*-type semiconductor with low electronic and ionic conductivity resulting in poor rate capability. It shows a large volume change, even with pulverization during the cycle process, which leads to a short lifecycle [204,205]. As the capacitive behavior of materials depends on their physical form and morphology, cobalt oxide is not an exception with nanoscale oxide having a higher SC value than bulk Co_3O_4 . Recent studies have been concentrating on Co_3O_4 with special morphology and microstructure. Microspheres, nanosheets, nanowires, nanorods, nanotubes as well as thin films have all been explored in the recent studies

on Co₃O₄ [205]. The nanosheet mesoporous Co₃O₄ arrays on Ni foam, as synthesized by Yuan *et al.* [206], exhibit a SC of 2735 F·g⁻¹ by electrodepositing Co(OH)₂ and then undergo a thermal transformation to Co₃O₄. Mesoporous Co₃O₄ nanowire arrays freely standing on the Ni foam substrate, as composed by Zhang *et al.* [207], were prepared via a two-step strategy: precipitating hydroxides followed by the calcination process. The SC value was estimated to be 1160 F·g⁻¹ with the degradation of only 9.6% after 5000 cycles. Ren *et al.* [208] fabricated hierarchically hollow Co₃O₄/polyaniline nanocages. This composite exhibited a large SC of 1301 F·g⁻¹ with a good cycling stability as 90% capacitance retention after 2000 cycles was achieved. The Co₃O₄ nanotubes were prepared by chemically depositing Co(OH)₂ into anodic aluminum oxide templates with heat treatment at 773 K [209]. This unique complex displayed a good supercapacitive performance with a SC of 574 F·g⁻¹.

Co(OH)₂-based materials are attractive due to their layered structure and a large interlayer spacing which promises a high surface area and a fast ion insertion/desertion rate [6,174,210]. Two reactions can occur, as expressed in (1.44) and (1.45) equations:



The theoretical SC value of Co(OH)₂ is about 3600–3700 F·g⁻¹. Its shortcomings are still the poor rate capability and cycle stability [172]. Zhou *et al.* [211] synthesized novel ordered mesoporous cobalt hydroxide films on the foamed nickel mesh and titanium plate via electrodeposition by using an aqueous domain *Brij 56*. The films demonstrated impressive results as the value of SC reached 2646 F·g⁻¹ for films on the Ni foam and 1018 F·g⁻¹ on the Ti plate. However, these values were achieved in a relatively narrow potential window from 0 V to +0.4 V. Another significant result of capacitance was demonstrated by Xia *et al.* [190] who presented a composite of Co(OH)₂ nanoflakes on 3D porous nano-Ni prepared by electrodeposition. This novel structure exhibited a high SC of 2028 F·g⁻¹ at 2 A·g⁻¹ and 1920 F·g⁻¹ at 40 A·g⁻¹ and maintained 94.7% capacitance after 2000 cycles. Jagadale *et al.* [212] potentiostatically deposited β-Co(OH)₂ nanoflakes on the stainless steel substrate. The film provided a SC of 890 F·g⁻¹ and a capacitance retention of 84% after 10,000 cycles.

In summary, Co(OH)₂-based electrodes can offer a much higher specific capacitance than Co₃O₄. However, such a high specific capacitance is only located in low potential ranges, which limits the materials' practical application in electrochemical supercapacitors [174].

1.3.2.2.2 Conducting polymers

Conducting polymers have been arousing great interest as a family of synthetic metals due to their rapid and reversible redox reactions and high doping levels [213]. Electronically conducting polymers (ECPs), such as polypyrrole (PPy), polyaniline (PANI), polythiophene (PTh), poly[3-methylthiophene] (PMTh) or poly[3,4-ethylenedioxythiophene] (PEDOT) can store and release charges through redox processes associated with the π-conjugated polymer chains [214,215]. ECPs can be p-doped with anions when oxidized and n-doped (or undoped) with cations when

reduced [159]. When oxidation occurs, ions from the electrolyte are transferred to the polymer backbone and, upon reduction, they are released back into the solution. Generally, *p*-dopable polymers are more stable than *n*-dopable ones. The doping/undoping process occurs throughout the bulk of the electrodes thus enabling the opportunity to achieve high values of specific capacitance [214]. An example of the occurring reaction could be expressed as follows:



The benefits of conducting polymers include their relatively high conductivity, low cost and ease of synthesis [216]. Such nanostructures of ECPs as nanotubes, nanowires and nanospheres can be produced via electrochemical deposition or chemical oxidation methods with the option of surfactant use [217]. Although ECPs possess a number of advantages that make them suitable for electrochemical supercapacitors, the insertion/desertion of counter ions during cycling causes volumetric changes of ECPs with progressive electrode degradation because of swelling, breaking and shrinkage being the origin of conductivity loss [214]. In addition to this, small working potential can be expected in order to avoid isolating states and/or polymer degradation due to overoxidation of the material [213]. These problems make it necessary to develop composite designs that utilize a carbon support structure with the polymer matrix, or through deposition of the polymer on a carbon surface to reduce these mechanical stresses and improve cyclability. Polymer/carbon composites obtained with high specific capacitance, respective cycle life and facile synthesis methods illustrate the effectiveness of incorporating carbon to help alleviate this problem. They have subsequently been shown to increase the porosity of the ECP [164]. Yan *et al.* [171] incorporated graphene with PANI, and this complex showed SC of $1046 \text{ F}\cdot\text{g}^{-1}$ in 6 M KOH. Furthermore, by the addition of approx. 1% of carbon nanotubes, a retention of 6% of the original capacitance after cycling remained. Khomenko, Frackowiak and Beguin [215] composed materials containing 20 wt% of multiwalled carbon nanotubes (MWNTs) and 80 wt% of chemically formed conducting polymers, such as PANI and PPy. The obtained values of specific capacitance varied from 250 to $1100 \text{ F}\cdot\text{g}^{-1}$. Multi-walled polypyrrole-coated carbon nanotube membranes were synthesized by Fang *et al.* [218] showing SC of $427 \text{ F}\cdot\text{g}^{-1}$. Electrochemical polymerization was applied to produce PANI nanotubes on a titanium nanotube template to exhibit $740 \text{ F}\cdot\text{g}^{-1}$ [219]. Another tube-covering-tube composite of carbon nanotubes and polyaniline was devised by Zhan *et al.* [220]. This PANI/CNTs composition yielded a relatively high SP value of $1030 \text{ F}\cdot\text{g}^{-1}$.

As the properties of conducting polymers can be significantly improved through preparing a CP-based composite, recent studies have mainly been focusing on such composites involving carbon, inorganic oxides/hydroxides and other metal compounds. Composite materials can provide a wide distribution of capacitance values which are also dependent on the parameters, such as the constituents of composites, the electrolytes in use, the scan rate, the current load, and the mass ratio of the components as well as cell the configuration [174]. Therefore, more investigations and developments are still needed to achieve the optimized

electrochemical properties of CP-based composites for electrochemical supercapacitor applications.

1.3.2.3. Hybrid Capacitors

Hybrid capacitors are designed to exploit the relative advantages and alleviate the relative disadvantages of electric double-layer and pseudocapacitors. By uniting both Faradaic and non-Faradaic processes to store charge, hybrid capacitors have achieved energy and power densities greater than EDLCs without losing the cycle stability and affordability that limits the success of pseudocapacitors. Research has focused on three different types of hybrid capacitors distinguished by their electrode configuration: composite, asymmetric and battery-type capacitors [160].

Composite electrodes integrate carbon-based materials with either conducting polymer or metal oxide/hydroxide materials and incorporate both physical and chemical charge storage mechanisms together in a single electrode [160]. Carbon-based materials provide a high surface area, which not only increases the contact between the pseudocapacitive material and the electrolyte but also facilitates a capacitive double layer of charge.

Asymmetric hybrid capacitors are constructed with a dissimilar anode and cathode to exploit the characteristic operating voltages of each material. In addition, materials with high hydrogen and oxygen evolution overpotentials are more suitable for these applications due to their ability to increase the operating window in aqueous electrolytes [164].

Battery-type hybrids couple two different electrodes like asymmetric hybrids. However, battery-type hybrid capacitors couple a supercapacitor electrode with a battery electrode. This configuration reflects the demand for higher energy supercapacitors and higher power batteries combining the energy characteristics of batteries with the power, cycle life and recharging times of supercapacitors [160].

1.3.3. Determination of Capacitive Parameters

The main parameters of supercapacitors are their specific capacitance, specific energy (or energy density), and specific power (or power density). There are several methods to measure and calculate these parameters. The value of a specific capacitance can be estimated theoretically for every active material according to the following equation [221]:

$$SC = n \frac{F}{\Delta V \cdot M}; \quad (1.47)$$

Here, n is the number of moles of charge transferred per mole of active material, F is Faraday's constant, M is the molar mass of the electroactive phase and ΔV is the potential sweep range.

However, charge-storing processes are complex and affected by a number of limiting factors; therefore, the theoretical values are difficult to achieve. A widely used technique to measure the practical value of specific capacitance is cyclic voltammetry (Fig. 1.10) because of its versatility, speed, scanning window determination and easy handling. However, this technique is more appropriate for application in laboratory cells as large devices lead to very large volumes of current

from several hundreds to thousands of amps [222]. At the laboratory level, it enables the investigation of active materials qualitatively and pseudo-quantitatively to study kinetic parameters by scanning a huge range of scan rates and to determine the voltage window [222].

The technique is based on applying a linear voltage ramp to an electrode between two potential values and measuring the resulting current. Usually, the measurements are carried out with active materials coated onto the inert electrode surface and immersed into a suitable electrolyte. The obtained results are employed to calculate the specific capacitance (SC) according to the following equation [223]:

$$SC = \frac{Q}{\Delta V \cdot \Delta m}; \quad (1.48)$$

Here, Q is the anodic charge, ΔV is the potential range and Δm is the electrode (active material) mass in grams.

The second method to estimate the capacitance from cyclic voltammograms is by integrating the area under $I-V$ curves and then dividing the value by the scan rate [212]:

$$SC = \frac{\int I dt}{dV/dt}; \quad (1.49)$$

Here, $\int I dt$ is the area under the curve, and dV/dt is the voltage scanning rate.

Cyclic voltammetry is useful to evaluate the cyclability of a supercapacitor (or an electrode) and the alterations of SC during cycling. However, usually, galvanostatic charging/discharging is better when performing such experiments [222].

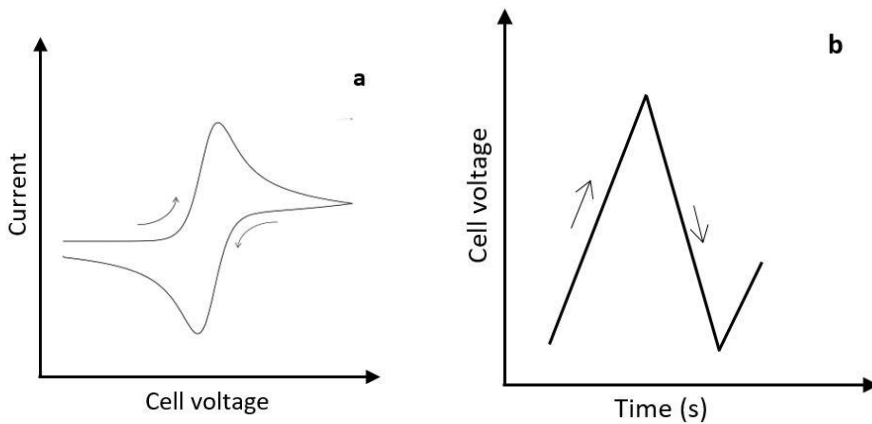


Fig. 1.10. Examples of a cyclic voltammogram (a) and a galvanostatic charge/discharge curve (b)

Galvanostatic cycling is a technique when, differently from cyclic voltammetry, the current is controlled, and the voltage is measured (Fig. 1.10). This method is also called chronopotentiometry, and it gives access to various parameters, such as capacitance, resistance and cyclability [222].

The specific capacitance ($F \cdot g^{-1}$) of a supercapacitor can be calculated from the slope of the curve $V-t$ (voltage-time); for a pseudo capacitor, when the $V-t$ curve profile is not strictly linear, the capacitance can be calculated according to the following equation [161,222]:

$$SC = \frac{I \cdot \Delta t}{\Delta V \cdot m}; \quad (1.50)$$

Here, I is the current at discharge time Δt , ΔV is the potential window, m is the mass of the electrode. Other energetic parameters, such as specific energy (SE , $Whkg^{-1}$) and specific power (SP , Wkg^{-1}), can be easily calculated from the SC by using the following formulas:

$$SE = \frac{1/2 \cdot SC \cdot \Delta V^2}{3.6} \quad (1.51)$$

$$SP = \frac{3600 \cdot SE}{t} \quad (1.52)$$

2. Experimental Part

2.1. Electrodeposition of Cobalt Oxide Coatings

Cobalt hydroxide films on stainless steel substrates were prepared by electrochemical deposition while using a standard three-electrode cell (volume: 100 mL). Two different supports were used during the synthesis: AISI304 stainless steel plates and *Bekipor ST 20AL3* mesh, which were cleaned chemically and ultrasonically. According to the manufacturer, the composition of AISI304 plates of 0.5 mm thickness is as follows: C: 0.08; Cr: 18–20; Ni: 8–10.5; Mn: 2.0; Si: 1.0; P: 0.045; S: 0.03; Fe: the balance. The sintered metal fibre filter (SMFF) *Bekipor ST 20AL3* in the form of a panel with a thickness of 0.49 mm was supplied by *Bekaert Fibre Technology* (Belgium). This material features a porosity of 81%.

All the solutions were prepared by using doubly distilled water and analytical grade reagents. Cobalt nitrate ($Co(NO_3)_2 \cdot 6H_2O$, >99% purity, *Chempur*, Poland), cobalt chloride ($CoCl_2 \cdot 6H_2O$, >99% purity, *Chempur*, Poland), cobalt acetate ($Co(CH_3COO)_2 \cdot 4H_2O$, >97% purity, *Reachim*, Russia), potassium nitrate (KNO_3 , purity >99%, *Lachema*, the Czech Republic) and sodium hydroxide ($NaOH$, >98% purity, *Lachema*, the Czech Republic) were used as received without further purification. Only freshly prepared solutions (the initial pH values are listed in Table 1.1) were used for the deposition. All the solutions were not deaerated during the experimental runs. The electrochemical synthesis was carried out at $291 K \pm 1 K$. The as-deposited samples were thoroughly washed with distilled water and dried to constant weight at room temperature. The electrodeposition process was carried out under galvanostatic conditions. The previously obtained results [31] showed that the most stable films were obtained at $0.5 mA \cdot cm^{-2}$ current density. Cobalt oxide coatings were prepared by temperature treatment of as-deposited coatings at 673 K for 1h.

Table 2.1. Initial pH values of the freshly prepared solutions for electrodeposition

Electrolyte bath	Initial pH
0.05 M Co(CH ₃ COO) ₂ + 0.1 M KNO ₃	7.05
0.05 M Co(NO ₃) ₂ + 0.1 M KNO ₃	3.93
0.05 M CoCl ₂ + 0.1 M KNO ₃	4.56

2.2. Synthesis of Nickel-Cobalt Oxides

Layered nickel-cobalt hydroxides were synthesized by using the potentiostatic electrodeposition method. AISI304 stainless steel plates (1×5 cm², 0.5 mm thick), FTO glass plates (1×4 cm², 2 mm thick, surface resistivity ~13 Ω cm⁻²) and SMFF *Bekipor ST 20AL3* (1×5 cm²) were cleaned chemically and ultrasonically and used as substrates. All the solutions were prepared by using doubly distilled water and analytical grade reagents. Cobalt nitrate (Co(NO₃)₂·6H₂O, >99% purity, *Chempur*, Poland), nickel nitrate (Ni(NO₃)₂·6H₂O, >98% purity, *Chempur*, Poland) and potassium nitrate (KNO₃, purity >99%, *Lachema*, the Czech Republic) were used as received without further purification. All the mixed cobalt-nickel hydroxides were deposited from an electrolyte bath containing 0.05 M Co(NO₃)₂·6H₂O, 0.05 M Ni(NO₃)₂·6H₂O and 0.1 M KNO₃ at 291 K ± 1 K. Only freshly prepared solutions (initial pH 3.66) were used for the synthesis without deaeration. The as-deposited samples were thoroughly washed with distilled water and dried to constant weight at room temperature. Nickel-cobalt oxide coatings were obtained after temperature treatment at 473–1073 K for 1h.

2.3. Analytical Techniques

2.3.1. Structure Analysis

X-ray powder diffraction (XRD) was performed with X-ray diffractometer *BRUKER AXS D8* (wave length $\lambda=1.54056 \times 10^{-10}$ m for Cu-K α radiation; Ni filter, detector position step 0.02°, anodic voltage 40 kV, current strength 40mA). The average crystallite size D_{hkl} was calculated from the line broadening by using the Scherrer's equation:

$$D_{hkl} = \frac{k\lambda}{B_{hkl} \cos\theta}; \quad (2.1)$$

Here, λ is the wavelength of Cu-K α radiation, θ is the Bragg diffraction angle, B_{hkl} is the full width at the half maximum intensity of the characteristic reflection peak, and k is a constant (the value used in this study was 0.94).

Differential scanning calorimetry and thermogravimetry (DSC–TG) analysis was performed on a *Netzsch STA 409 PC Luxx* (Netzsch GmbH, Germany) simultaneous thermal analyzer. The heating was carried out in air, the rate of temperature increase was 15 K min⁻¹, and the temperature range from 303 K to 1073 K was used.

Atomic absorption spectroscopy (AAS) analysis was performed with a *Perkin Elmer 403* spectrometer. The radiation source was a hollow cathode lamp.

Atomization was carried out in a flame by using the acetylene-air mixture. The coatings were scraped and dissolved in 50 mL of 0.1 M HNO₃. The content of nickel and cobalt in the coatings was determined by measuring the absorption at 232.0 and 240.73 nm, respectively.

Raman scattering measurements were performed by using a Raman microscope *inVia* (Renishaw). The excitation beam from a diode laser of 532 nm wavelength was focused on the sample by using a 50× objective (NA=0.75, *Leica*). The laser power at the sample surface was 1.75 mW. The integration time was 10 s, the signal was accumulated 1–5 times and then averaged. The Raman Stokes signal was dispersed with a diffraction grating (2400 grooves/mm), and the data was recorded by using a Peltier cooled charge-coupled device (CCD) detector (1024×256 pixels). This system yields a spectral resolution of about 1 cm⁻¹. Silicon was used to calibrate the Raman setup in both Raman wavenumber and spectral intensity.

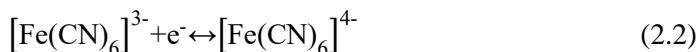
Scanning electron microscopy (SEM) images of all the coatings were investigated with a *Quanta FEG 200 (FEI)* high resolution scanning electron microscope. The images were obtained at 10–30 kV, the pressure in the chamber was set at 80 Pa, and up to ×100 000 magnification was employed depending on the sample. The samples were imaged without any conductive coating. *Bruker AXS Microanalysis GmbH QUANTAX energy dispersive X-Ray spectrometer* (EDS) was used to compose the element map and spectra. Samples were imaged without any conductive film.

The **pH** was measured by using a *Knick pH-Meter 766 Calimatic* device (Germany).

2.3.2. Electrochemical Behavior

Cyclic voltammetry (CV), linear sweep voltammetry (LSV) and galvanostatic charge/discharge (GCD) measurements were carried out by computer-controlled galvanostats/potentiostats *BioLogic SP-150* (France) and *Autolab PGSTAT12 (Ecochemie, The Netherlands)*. The *EC-Lab[®] V10.39* and *GPES[®] 4.9* software was used for the collection and treatment of the experimental data. A typical three-electrode system consisting of a platinum wire (geometric area of about 15 cm²) as a counter electrode, Ag,AgCl|KCl_(sat) as a reference electrode, and deposited oxide films as the working electrodes was employed. The GCDL tests were performed at current densities of 1–10 A·g⁻¹ in a 0.1 M NaOH electrolyte solution.

Potassium ferricyanide (purity >99%, *Reachim, Russia*) was used for the determination of the electroactive surface area of the coatings by using cyclic voltammetry. The oxidation-reduction system of ferricyanide/ferrocyanide exhibits nearly a fully reversible electrode reaction without any side reactions. The system can be illustrated by the reversible reaction below [224,225]:



The oxidation-reduction reaction generates peaks in the cyclic voltammograms. In this work, the calculation of the electroactive surface area was based on a comparison of the current peaks of an AISI 304 stainless steel plate with a definite surface area and *Bekipor ST 20AL3* mesh with a geometrically equal surface area. It

should be noted that the active surface area of AISI304 is not necessarily equal to the geometric area, but it served as a reference material. Each substrate was scanned for 10 times to assess the stability of the system and to avoid any possible deviations. The values of the electroactive surface area were calculated according to the Randles-Sevcik equation:

$$I_p = k \cdot n^3 \cdot A \cdot D^{1/2} \cdot C \cdot v^{1/2}; \quad (2.3)$$

Here, D (diffusion coefficient in cm^2), n (the number of electrons transferred per mole of electroactive species), v (potential scan rate, V/s), k (constant) and C (the solution concentration in moles/L) are the same for AISI304 and *Bekipor ST 20AL3*. The electroactive surface area A is directly proportional to the peak current value I_p [226].

3. Results and Discussion

3.1. Structure and Electrochemical Behavior of Cobalt Oxide Coatings

Cobalt oxide coatings have found many applications in catalysis [227,228], energy storage [9,61], and in the purification of organic compounds [229] as it has been pointed out above, i.e., in the literature review section. Taking into account this information, the electrochemical properties of all the prepared coatings were evaluated in terms of the oxygen evolution reaction and the pseudocapacitive behavior. Although coatings can be synthesized in many ways, electrochemical deposition from aqueous solutions is distinguished as a relatively simple, low-cost and environmentally friendly technique enabling to modify the morphology and structure of the coatings by changing the deposition variables. As well as the synthesis method, the electrolyte bath composition and substrate play a crucial role in creating an effective electrochemical system. For this reason, three different precursors (nitrate, chloride and acetate) and a novel substrate with a 3D structure *Bekipor ST 20AL3* were selected to perform the investigations in this work.

Bekipor ST 20AL3 is a stainless steel mesh composed of chaotically oriented thin metal filaments forming a panel. Its small fiber diameter ($d=2-30 \mu\text{m}$), density and thickness enable the increase of the surface area thus ensuring excellent accessibility of internal filaments and the free flow of the electrolyte [230]. However, the traditional synthesis of cobalt (hydro)oxide coatings seems to reduce the surface area of this mesh by clogging the space between fibers; meanwhile, electrodeposition provides uniform coverage of each filament. Increasing the surface area of a coating ensures the larger interface of electrode/electrolyte thus allowing to expect better catalytic and pseudocapacitive performance.

3.1.1. Synthesis of Cobalt (hydro)oxide Coatings by Electrodeposition

The structure of $\alpha\text{-Co(OH)}$ is known to consist of layers of cobalt hydroxide with anion impurities intercalated into interlayer spacing as it has been described in [3-5]. These impurities have a considerable influence on the electrochemical properties of as-deposited coatings. Therefore, electrolytes containing three different

anions – nitrate, chloride and acetate – were selected to conduct the synthesis. Fig. 3.1 shows cyclic voltammograms of *Bekipor ST 20AL3* stainless steel mesh in nitrate, chloride and acetate electrolytic baths. The potential was firstly applied from the initial (at around -0.1 V) to the cathodic side to initiate the formation of cobalt hydroxide. According to the widely accepted mechanism of electrochemical deposition of metal hydroxides, nitrate ions are firstly reduced on the substrate by electrons, and a mass of hydroxyl ions is generated at potential values of -0.5 V (cathodic peak C₁) [231]:



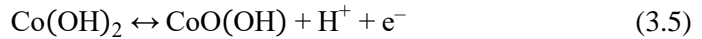
Subsequently, with the help of these electrogenerated bases, Co^{2+} ions and OH^- ions can easily combine into a $\text{Co}(\text{OH})_2$ precipitate displaying the hysteresis loop in the cathodic section [231]:



A sudden increase in the cathodic current at more negative potentials is mainly the consequence of hydrogen evolution, which, depending on the pH value, can occur according to (3.3) or (3.4) equations (cathodic peak C₂):



A significant increase in the current in the anodic part starting at $+0.55$ V is assigned to the oxidation of deposits (anodic peak A₁) and the oxygen evolution reaction (peak A₂) according to (3.6) and (3.7) equations [37]:



What concerns a comparison of the patterns of cyclic voltammograms of all the three precursors, the mechanisms of the redox reactions are similar, yet some differences are noticeable. Although the growth rate and the mass of coating from nitrate solution appears to be the smallest, this precursor generates the highest anodic current at $+1.0$ V.

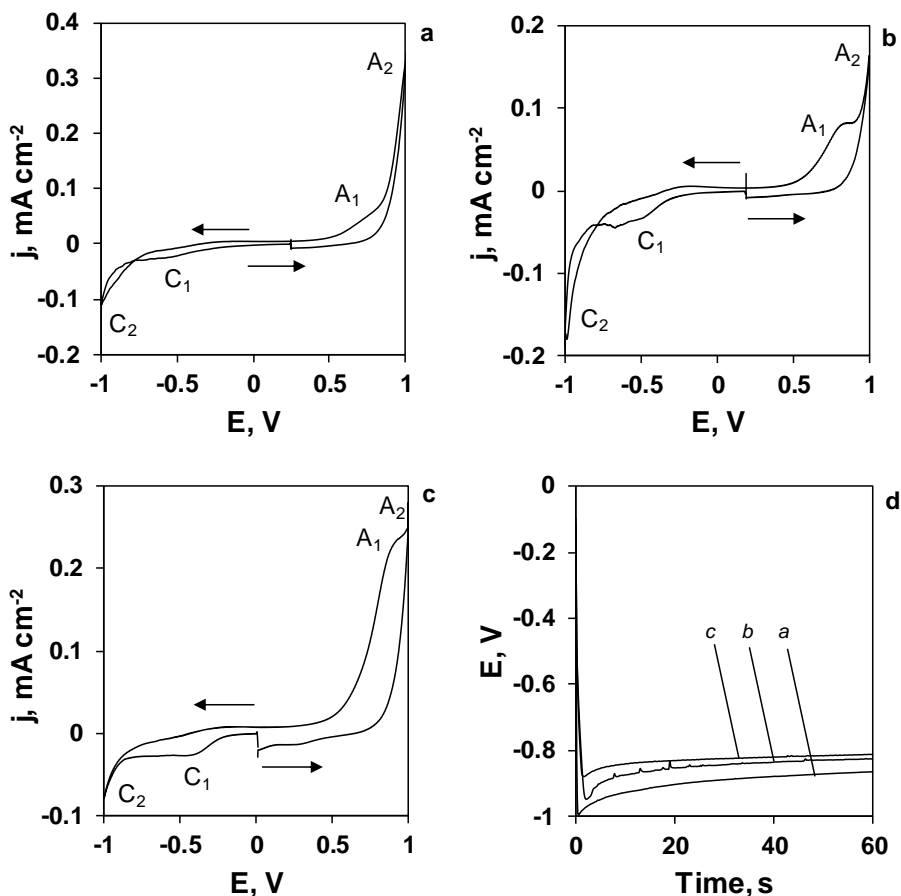


Fig. 3.1. Cyclic voltammograms (*a*, *b*, *c*) and chronopotentiograms (*d*) of *Bekipor ST 20AL3* stainless steel mesh in three different electrolytes: *a* – 0.05 M $\text{Co}(\text{NO}_3)_2$ + 0.1 M KNO_3 ; *b* – 0.05 M CoCl_2 + 0.1 M KNO_3 ; *c* – 0.05 M $\text{Co}(\text{CH}_3\text{COO})_2$ + 0.1 M KNO_3 . Scan rate – 20 mV s^{-1} , current density – 0.5 mA cm^{-2}

3.1.2. Structure Analysis of Cobalt Oxide Coatings

As it was discussed in Chapter 1.1.2, thermogravimetry and differential scanning calorimetry (TG-DSC) revealed that, at 470–535 K, the decomposition of the hydrotalcite-like structure of $\text{Co}(\text{OH})_2$ occurs, which leads to the formation of Co_3O_4 (Chapter 1.1.1). According to the TG-DSC data, the annealing temperature of 673 K for as-deposited cobalt hydroxide coatings to produce Co_3O_4 was selected. X-ray photoelectron spectroscopy confirmed the formation of cobalt hydroxide ($\text{Co}(\text{OH})_2$) in as-deposited coatings and the cobalt oxide Co_3O_4 structure in annealed at 673 K coatings (Chapter 1.1.1). Fourier transform infrared spectroscopy (FTIR) results of as-deposited films confirmed the α -cobalt hydroxide layers with anionic impurities in the interlayer spacing. Meanwhile, annealed coatings demonstrated the spinel Co_3O_4 structure with Co^{3+} ions in the octahedral position and Co^{2+} ions in the tetrahedral position (Chapter 1.1.1).

X-ray powder diffraction (XRD). The coatings were deposited from electrolyte baths containing three different sources of cobalt (II) ions (nitrate, acetate and chloride). The composition and structure of the as-deposited and annealed at 673 K for 1h cobalt (hydro)oxide films were investigated by using X-ray powder diffraction (Fig. 3.2). XRD analysis of as-deposited coatings indicated patterns characteristic mainly to α -cobalt hydroxide $\text{Co}(\text{OH})_2$ (d-spacing 0.274, 0.268, 0.237, etc. nm.; JCPDF 2-925). However, small quantities of impurities and intercalated ions, which are unavoidable during electrosynthesis, were specific to each electrolyte. Cobalt hydroxide deposited from cobalt chloride (Fig. 3.2, *a*, 2) turned out to have the highest amount of impurities indicated as potassium cobalt oxide KCoO_2 , JCPDF 32-769. The peak analysis was made with computer software according to the highest possibility, and the deposition conditions were not estimated. As KCoO_2 is sensitive to humidity [232] and as deposition is carried out in an aqueous solution, the formation of pure KCoO_2 is questionable – as a matter of fact, a crystalline complex of potassium, cobalt and oxygen is more likely to form. However the presence of this side-product is visible as it gives a green shade to blue α - $\text{Co}(\text{OH})_2$. The XRD analysis of cobalt hydroxide deposited from nitrate electrolyte (Fig.3.2, *a*, 1) indicated a compound of nitrate, cobalt and potassium ions which intercalated into the structure (the peak is marked as Y). Cobalt hydroxide deposited from cobalt acetate also contains impurity which was determined to be cobalt acetate (Fig.3.2, *a*, 3).

The corresponding XRD pattern of thermally treated samples (Fig. 3.2, *b*) reveals diffraction peaks which can be readily attributed to the cubic phase of Co_3O_4 (d-spacing 4.6694, 2.8580, 2.4349, etc. nm.; JCPDF 76-1802) without any impurities left after annealing.

To evaluate the influence of precursors to the morphology of the deposits, the crystallite sizes were calculated according to Scherrer's equation (2.1), and the obtained results are given in Table 3.1. It may be noted that cobalt hydroxide deposited from nitrate and acetate electrolytes is distinguished by its almost equally crystallite size, meanwhile, cobalt hydroxide crystals obtained from a chloride precursor are smaller. On the whole, the average values of the Co_3O_4 crystallite size are close for all the three precursors.

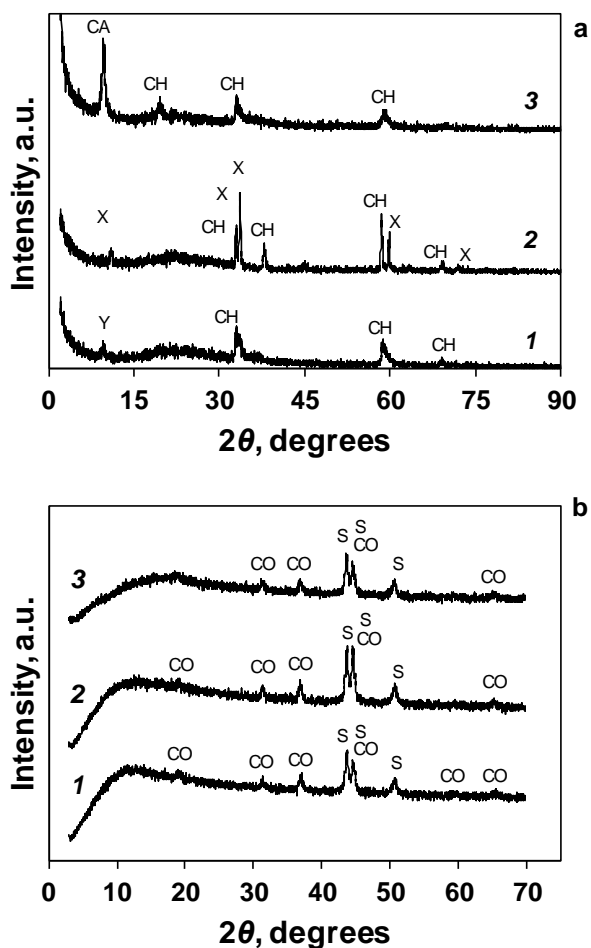
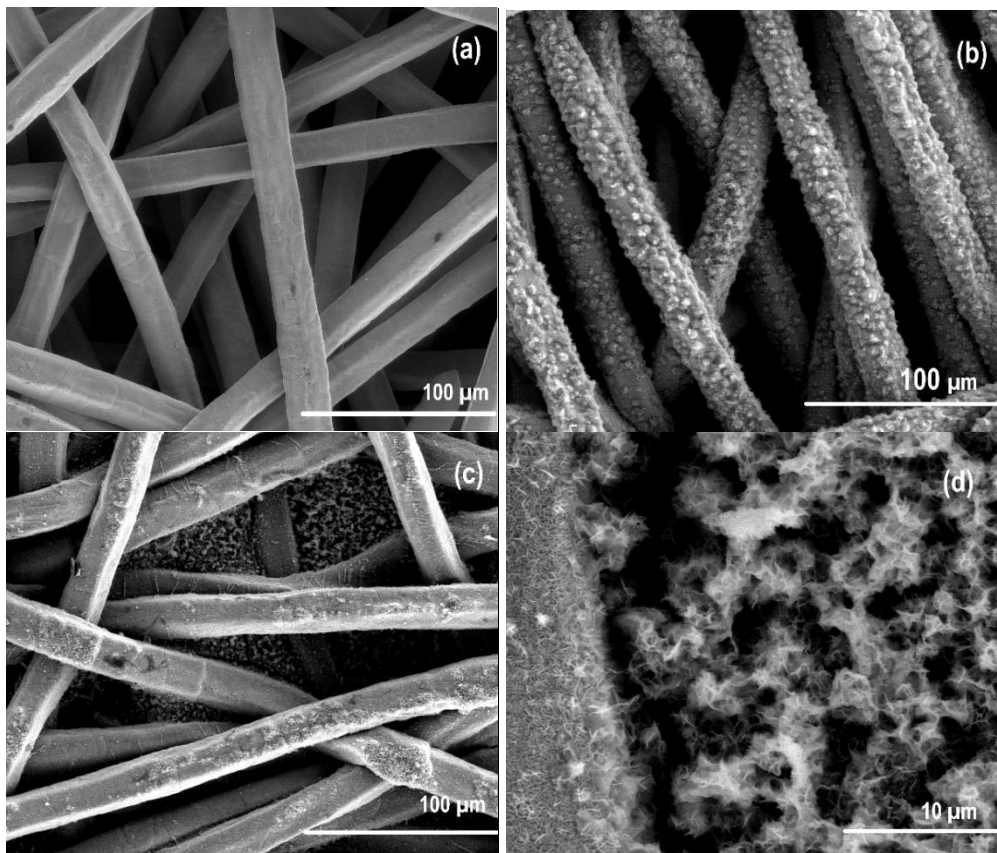


Fig. 3.2. XRD patterns of as-deposited (a) and annealed at 673K (b) cobalt (hydro)oxide films electrodeposited by using different cobalt precursors: 1 – cobalt nitrate; 2 – cobalt chloride; 3 – cobalt acetate. Indexes: CH – cobalt hydroxide, CO – cobalt oxide, CA – cobalt acetate, X – potassium cobalt oxide, Y – a mixed potassium, nitrate and cobalt compound, S – a substrate (stainless steel)

Table 3.1. Average crystallite size of cobalt oxide coatings deposited from different electrolyte baths, calculated according to Scherrer's equation

Sample notation	Average crystallite size, nm
Co(OH) ₂ from acetate	24.0±1
Co(OH) ₂ from nitrate	25.4±1
Co(OH) ₂ from chloride	18.3±1
Co ₃ O ₄ from acetate	20.4±1
Co ₃ O ₄ from nitrate	23.7±1
Co ₃ O ₄ from chloride	26.6±1

Scanning electron microscopy (SEM) images at different magnifications of an uncovered *Bekipor ST 20AL3* mesh (Fig. 3.3, *a*) and a mesh with cobalt hydroxide deposited from a nitrate precursor for 120 s and 300 s are shown (Fig. 3.3, *b–e*). The formation of a 3D structure of the electrocatalyst with covered filaments and free space between them for the electrolyte to flow freely was one of the main purposes of this work. Upon reviewing SEM images, an assumption can be made that with a duration of synthesis which is longer than 300 s, the active surface area gets reduced due to the clogging of the space between fibers (Fig. 3.3, *c, d*). When comparing as-deposited (Fig. 3.3) and annealed (Fig. 3.4) samples, both films showed a very distinct clustering behavior at a lower magnification, whereas, at a higher magnification, a lamellar structure can be seen. The morphology of as-deposited and annealed films from all the three different electrolytes is virtually identical.



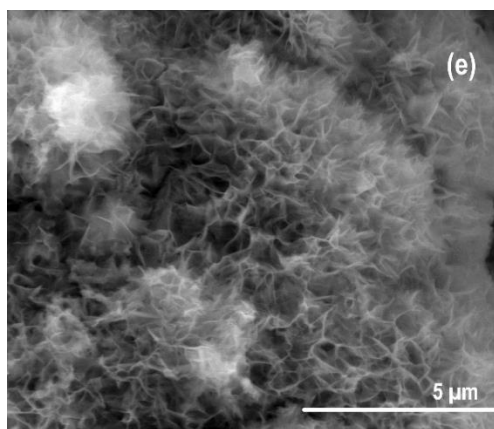


Fig. 3.3. Representative SEM images of clean *Bekipor ST20AL3* stainless steel mesh (a) and as-deposited Co(OH)_2 films (b–e) from nitrate precursor at different deposition times (s): b – 120, c and d – 300. Magnifications: a, b, c – $\times 1000$; d, e – $\times 20000$

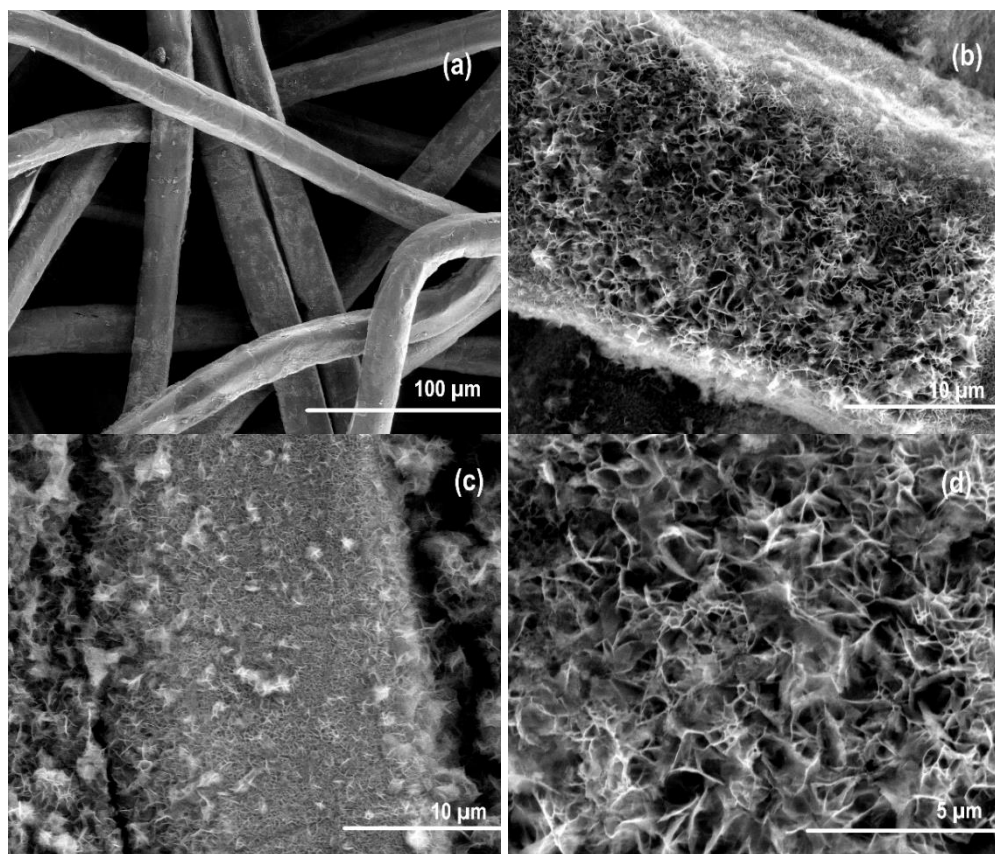


Fig. 3.4. Representative SEM images of Co_3O_4 obtained from nitrate precursor on *Bekipor ST 20AL3* at different deposition times: a – 120 s, b, c, d – 300 s. Magnifications: a – $\times 1000$; b, c – $\times 8000$; d – $\times 20000$

3.1.3. Electrochemical Behavior

Cobalt hydroxide and oxide are known to be effective catalysts in electrochemical and chemical reactions; they are also able to store the charge in the supercapacitor application [2]. The oxygen evolution reaction and pseudocapacitance measurements were chosen as test procedures for the investigation of the electrochemical properties of the prepared coatings. As many electrochemical reactions occur on the interface of the electrode/electrolyte, the surface area plays an important role in improving the activity and efficiency of active materials. For this reason, the attempt to estimate the electroactive surface area was made first.

3.1.3.1. Determination of Electroactive Surface Area

In order to calculate an effective current density, it is important to evaluate the electroactive surface area. This is a challenging scientific task, and various experimental procedures can be applied as it has been already emphasized by Trasatti and Petrii [233]. The manufacturer of SMFF *Bekipor ST 20AL3* does not provide such information, therefore, the electroactive surface area was determined by cyclic voltammetry (Fig. 3.5) using an oxidation-reduction system and containing 2 mM $K_3[Fe(CN)_6]$ and 0.1 M KNO_3 as described in Chapter 2.3.2. Depending on the substrate origin and the different interaction between its surface and the electrolyte, the characteristic anodic peaks were detected at +0.56 V (a) and +0.40 V (b). Our analysis and calculation revealed that the average electroactive surface area of an uncoated *Bekipor ST 20AL3* mesh is $6 \text{ cm}^2/\text{cm}^2$. This number was used for the calculation of the effective current density of galvanostatic deposition.

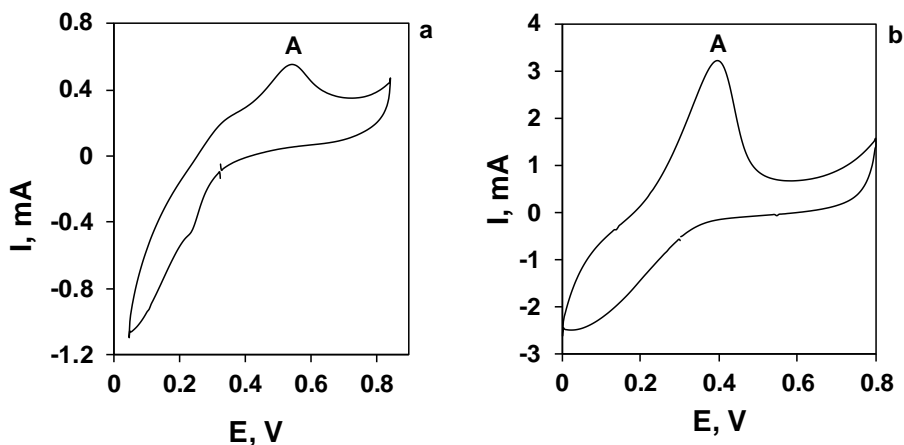


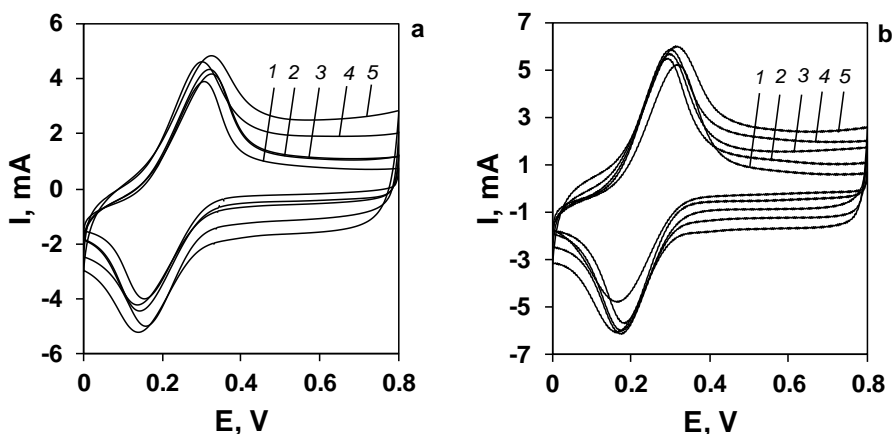
Fig. 3.5. Characteristic cyclic voltammograms of uncoated AISI304 plate (a) and *Bekipor ST 20AL3* (b) mesh in 2 mM $K_3[Fe(CN)_6]$ + 0.1 M KNO_3 electrolyte

SMFF *Bekipor ST 20AL3* is distinguished by its mesh structure having chaotically oriented metal filaments. To achieve the highest surface area of the active material, each filament should be coated separately, and the space between them should not be clogged. Therefore, it is important to explore the growing process of the coating and to determine the most effective duration of synthesis. The electroactive

surface area of as-deposited $\text{Co}(\text{OH})_2$ films at different deposition times was measured by using the same ferro-ferricyanide oxidation-reduction system as with an uncoated mesh. Unfortunately, due to the occurring oxidation of the $\text{Co}(\text{OH})_2$, anodic peak A was inconspicuous; furthermore, as the values of the current density are significantly increased by oxidation processes, the values of the electroactive surface area would be unreliable.

Cobalt oxide Co_3O_4 as a well-known material for its electrocatalytic activity [234-238] in the oxygen evolution reaction was tested under the same conditions in order to investigate the effect of temperature treatment on the electroactive surface area (Fig. 3.6). To evaluate the influence of electrolyte composition during synthesis of cobalt hydroxide to electroactive surface area, and three different sources of cobalt were chosen to complete this task: nitrate, chloride and acetate.

All the calculated values of Co_3O_4 are presented in Table 3.2. As it can be seen, Co_3O_4 obtained after thermal treatment of as-deposited coatings from nitrate and chloride precursors demonstrates very close values of ESA, whereas the acetate precursor seems to increase the active surface. This ESA technique is based on the $\text{Fe}(\text{II})/\text{Fe}(\text{III})$ adsorbed on the surface redox reactions. XRD analysis and calculations (Table 3.1) revealed that Co_3O_4 synthesized from the acetate precursor is composed of the smallest particles among all the three precursors (the average crystallite size is 20.4 nm). Therefore, an assumption that smaller particles are able to adsorb more ions on the surface and so are able to increase the redox current can be made. When comparing the initiation of the coatings' growth, the chloride precursor turned out to speed up the formation of films in the first minute as it generates the highest values of ESA after 60 s. This can be related to the difference in mobility of anions in water as the chloride anion has an advantage over nitrate and acetate. Later, the ESA of coatings from chloride increased slower because cobalt oxide particles tend to aggregate during thermal treatment (Table 3.1).



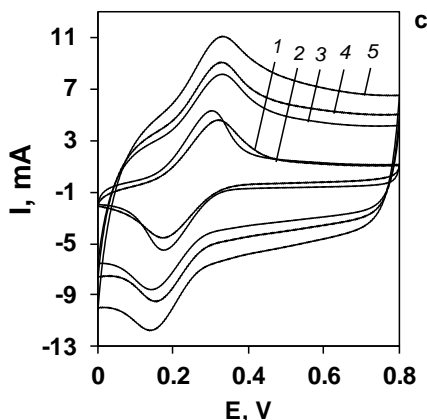


Fig. 3.6. Characteristic cyclic voltammograms of Co_3O_4 films in 2 mM $\text{K}_3[\text{Fe}(\text{CN})_6]$ + 0.1 M KNO_3 electrolyte at different deposition times: 1 – 60 s, 2 – 120 s, 3 – 180 s, 4 – 240 s, 5 – 300 s. The source of cobalt: a – nitrate; b – chloride; c – acetate

Table 3.2. Values of the electroactive surface area of cobalt oxide films on *Bekipor ST 20AL3* from different precursors

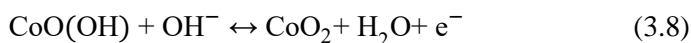
Source of cobalt	Electroactive surface area of Co_3O_4 , cm^2/cm^2				
	Deposition time, s				
	60	120	180	240	300
Cobalt nitrate	7.2	7.7	7.9	8.5	8.9
Cobalt chloride	9.5	10.0	10.4	10.7	11.0
Cobalt acetate	8.3	9.7	14.7	16.5	20.2

3.1.3.2. Electrocatalytic Activity of Cobalt (hydro)oxide in OER

Linear sweep voltammetry was performed for the evaluation and comparison of the electrocatalytic behavior in the OER of the films deposited from different electrolytes on *Bekipor ST 20AL3*. The geometric surface area of the mesh was used during the calculations of the current density and the potential window 0 ÷ +1.1 V. These experimental runs were carried out by using films prepared after different electrodeposition times (60–300 s). Fig. 3.7, a represents the first and the fifth scans of a common linear sweep voltammogram of $\text{Co}(\text{OH})_2$ on *Bekipor ST 20AL3*. As it can be seen, there is a considerable oxidation peak at around +0.3 ÷ +0.35 V in the first scan which decreases significantly in the fifth scan; this peak can be related to the primary oxidation of the film itself [30,239]:



By sweeping the potential to the anodic direction, oxygen evolution starts at +0.6 V along with the further oxidation of the film:



The films deposited from cobalt nitrate show the highest electrocatalytic activity. The activity of the coatings synthesized from cobalt chloride and acetate are rather similar as their generated current density does not exceed $8 \text{ mA}\cdot\text{cm}^{-2}$. These differences can be related to the different amount of impurities during electrodeposition, which was confirmed by XRD analysis (Fig. 3.2). As it was mentioned above, cobalt hydroxide deposited from chloride electrolyte contains a considerable quantity of side-product of potassium, cobalt and oxygen, which negatively affects the activity of the active material in both capacitive and electrocatalytic applications and yields a green shade to blue $\alpha\text{-Co(OH)}_2$. Meanwhile, as-deposited coatings from nitrate and acetate solutions are much less impure and retain their blue color. When comparing the current densities of coatings from different precursors (Fig. 3.7, *b*), cobalt hydroxide deposited from cobalt nitrate is distinguished due to its slower growth of the coating (Table 3.2). Its activity increases with a longer deposition time; meanwhile, coatings synthesized from a chloride and acetate bath are the most active when deposited for 60 s. Longer synthesis reduces or does not affect their catalytic ability in OER. These regularities are related to the structure of the *Bekipor ST 20AL3* mesh as it is composed of chaotically situated filaments. Therefore, it is important to control the growth of the coating so that every filament would be covered separately, and that the interlayer spacing would not be clogged. The electroactive surface area calculated in Chapter 3.1.3.1 gives only the relative total active area and does not provide information about the direction of the film formation. Hence, it is probable that when synthesizing films from acetate and chloride electrolytes, mesh filaments are coated during the first minute, while further growth occurs uncontrollably.

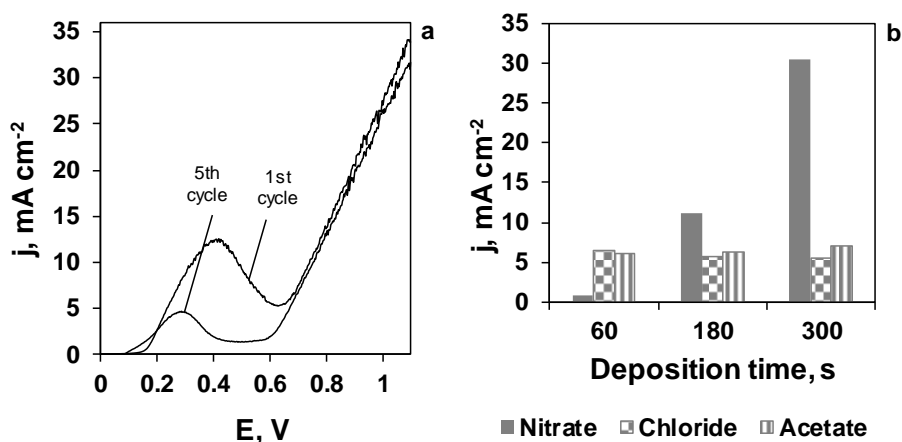
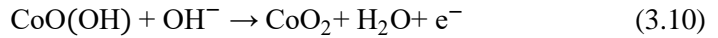


Fig. 3.7. (a) Representative linear sweep voltammograms of Co(OH)_2 on *Bekipor ST 20AL3* in 0.1 M NaOH at a scan rate of 20 mV s^{-1} . (b) Values of current density at +0.7 V generated by Co(OH)_2 deposited 120-240 s from different precursors

The plots of linear sweep voltammetry of annealed films consisting of Co_3O_4 are shown in Fig. 3.8. The main figures are submitted with the current densities calculated according to the geometric surface area, meanwhile, the electroactive surface area is introduced in insets. In all the linear sweep voltammograms, the redox

peaks at around $+0.58 \div +0.65$ V are observed, which corresponds to the change between different cobalt oxidation states according to the following reactions [228,240,241]:



The films deposited from cobalt nitrate electrolyte are distinguished as the most electrochemically active in the oxygen evolution reaction whereas cobalt oxide obtained from cobalt acetate and cobalt chloride shows lower activity. This drop of current density for coatings from acetate and chloride precursors can also be related to a significantly higher amount of impurities compared with the nitrate precursor. As it can be seen from Fig. 3.8, the considerable peaks at $+0.5 \div +0.7$ V prove the occurring oxidation of the film deposited from chloride (Fig. 3.8, *b*) and acetate (Fig. 3.8, *c*) electrolytes, while the nitrate precursor allows obtaining superior purity of cobalt oxide (Fig. 3.8, *a*).

Due to the complexity of the OER occurring on the surface of metal oxides, the exact interpretation of the observed variations in the electrocatalytic activity of the prepared samples is almost impossible. As it has been pointed out by Doyle and Lyons [242], metal oxides are an extremely complex experimental system, and their electrocatalytic activity is highly dependent on a multitude of parameters, such as the electronic structure at the surface and in the bulk, morphology, material preparation history, etc. Special attention should be paid to the electroconductivity of the films if the OER is to proceed at a practical rate. The electroconductive properties are highly influenced by the presence of dopants and impurities as well as by the film thickness and other factors. In our case, the variations in electrocatalytic activity of cobalt (hydro)oxides can be partly related to the different amount of impurities incorporated during electrodeposition. As it was confirmed by XRD analysis (Fig. 3.2), cobalt hydroxide deposited from the chloride electrolyte contains a considerable quantity of side-product involving potassium which can negatively affect the activity of the active material in both capacitive and electrocatalytic applications. On the other hand, the heat treatment improved the electrocatalytic activity of the films which thus tend to become more compact and pure.

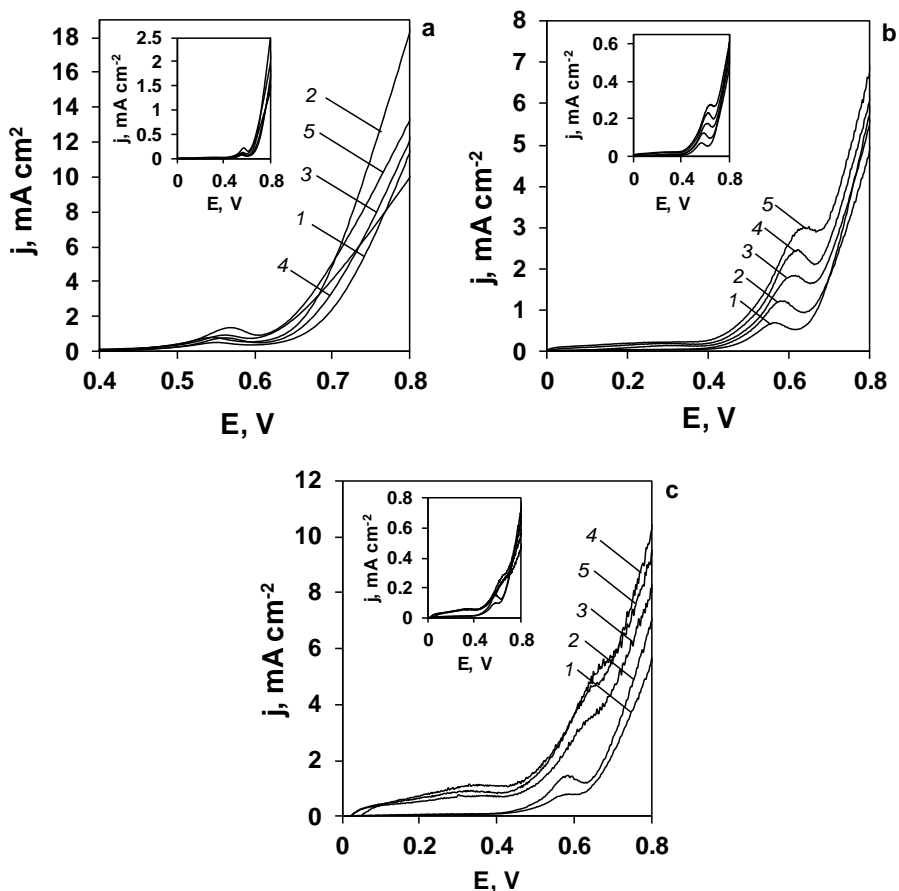


Fig. 3.8. Linear sweep voltammograms of Co_3O_4 films on *Bekipor ST 20AL3* deposited from nitrate (a), chloride (b) and acetate (c) baths. Deposition times: 1 – 60 s, 2 – 120 s, 3 – 180 s, 4 – 240 s, 5 – 300 s. Supporting electrolyte – 0.1 M NaOH. Insets – linear sweep voltammograms of Co_3O_4 , current density calculated according to the electroactive surface area (Table 3.2)

In order to investigate the electrochemical behavior of $\text{Co}(\text{OH})_2$ and Co_3O_4 films in the oxygen evolution reaction, controlled potential electrolysis was conducted in a 0.1 M NaOH solution at various applied potentials (Fig. 3.9 and Fig. 3.10). The electrolyte solution was continuously stirred, and, after each measurement, the electrode was allowed to reach its steady-state potential. All the values of the current density were calculated according to the geometric surface area. When comparing the results of as-deposited coatings (Fig. 3.9), the highest current density was generated by cobalt hydroxide deposited from cobalt nitrate; furthermore, $\text{Co}(\text{OH})_2$ films from acetate and chloride precursors were distinguished with a considerably high amount of undesirable noises when applying potentials over +0.66 V. These results can be related to the oxidation of side-products in the film structure, decreasing their catalytic activity and complicating the contact between the electroactive substance and the

electrolyte. Meanwhile, as-deposited $\text{Co}(\text{OH})_2$ synthesized from a nitrate precursor showed reasonably good current density and stability in the higher potential region due to its purer structure verified by XRD results (Fig. 3.2).

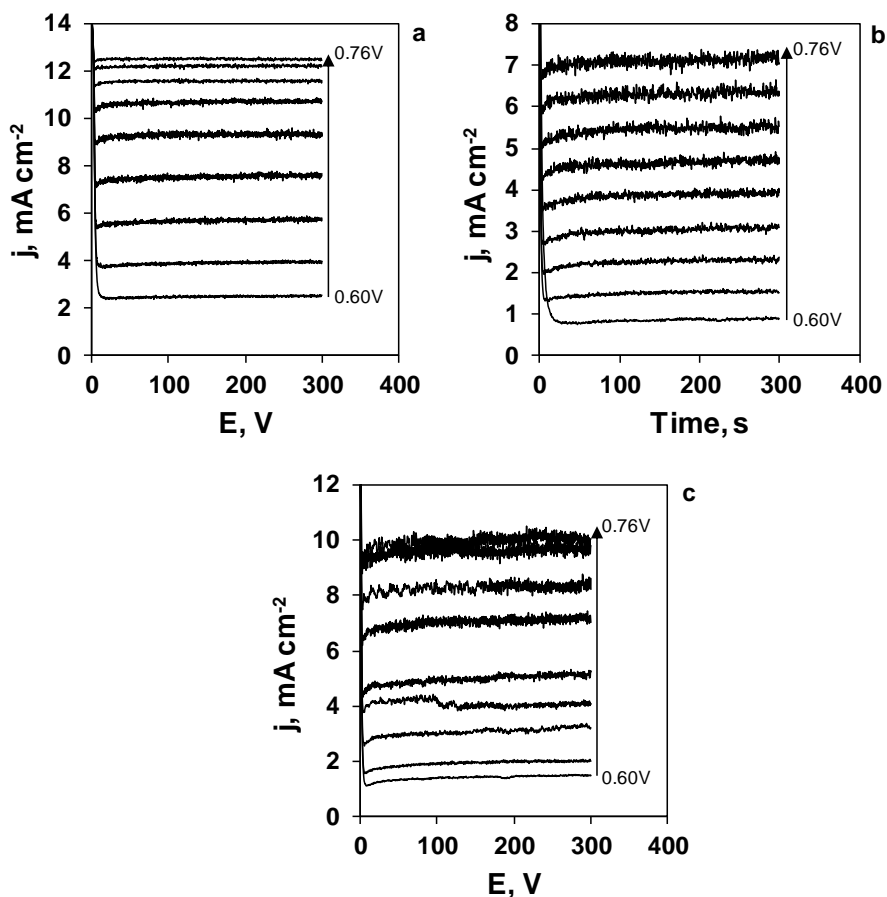


Fig. 3.9. Characteristic chronoamperograms of cobalt hydroxide films on *Bekipor ST 20AL3* deposited from different electrolytes: *a* – cobalt nitrate; *b* – cobalt chloride; *c* – cobalt acetate. Supporting electrolyte – 0.1 M NaOH

Controlled potential electrolysis under the same conditions was performed for cobalt oxide coatings annealed at 673 K for 1h, and the results are given in Fig. 3.10. When comparing the influence of different precursors, the highest current density is generated by the coating deposited from the nitrate precursor (Fig. 3.10, *a*), meanwhile, cobalt oxides from chloride (Fig. 3.10, *b*) and acetate (Fig. 3.10, *c*) generate lower values of current density; also, significant noises in these curves are noticed, particularly for the films from the acetate precursor. These results suggest the assumption that Co_3O_4 deposited from chloride and acetate retains more impurities after heat treatment.

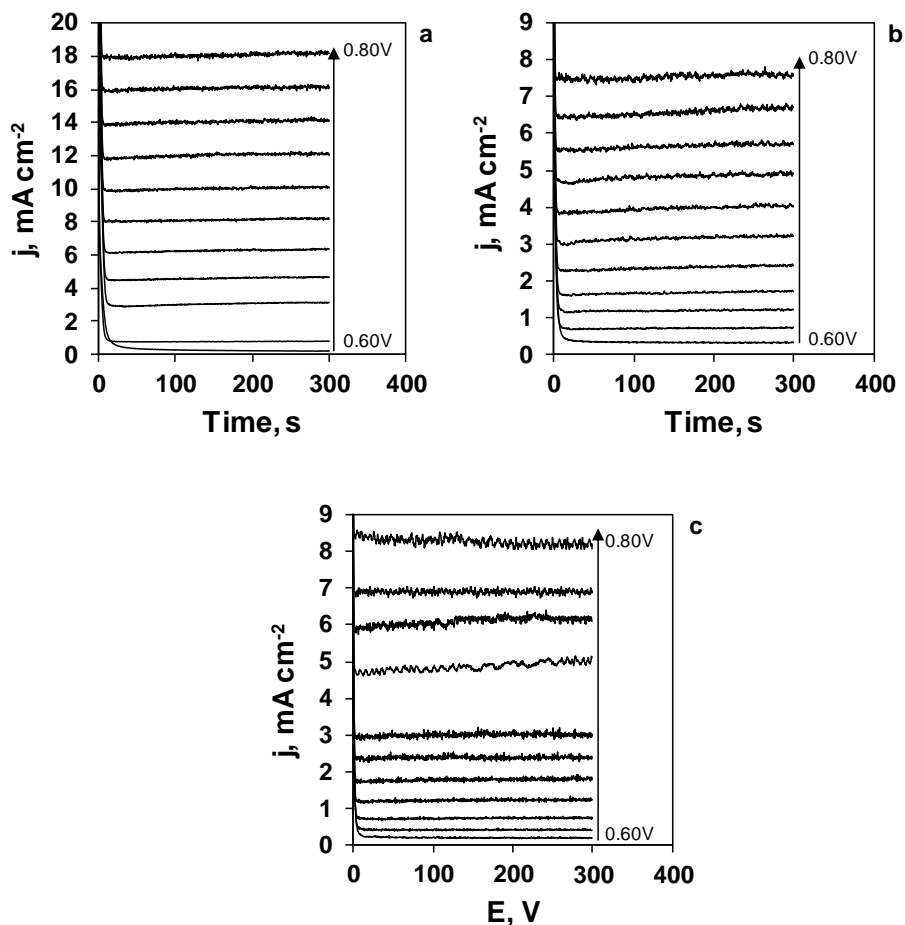


Fig. 3.10. Characteristic chronoamperograms of cobalt oxide films on *Bekipor ST 20AL3* deposited from different electrolytes: *a* – cobalt nitrate; *b* – cobalt chloride; *c* – cobalt acetate. Supporting electrolyte – 0.1 M NaOH

The collected electrolysis data was used to construct the Tafel plot presented in Fig. 3.11. It is well known that the Tafel equation possesses fundamental importance in electrochemical kinetics, and slope b is an indicative parameter of the electrode reaction mechanism [243]. Overpotential η was calculated according to the following equation:

$$\eta = E_{appl} - 0.26; \quad (3.11)$$

Here, E_{appl} is the applied potential (V) measured against $\text{Ag, AgCl} | \text{KCl}_{(sat)}$ reference electrode, 0.26 is the value of the equilibrium potential against $\text{Ag, AgCl} | \text{KCl}_{(sat)}$ reference electrode for water oxidation at pH 13. Fig. 3.11 presents the dependence of the overpotential as a function of logarithm of the current density for $\text{Co}(\text{OH})_2$ and Co_3O_4 electrodes. As an abrupt change of the Tafel slope is observed for all the films at the overpotential values higher than $+0.42 \div +0.46$ V, it can be

considered as an indication of the change of the reaction mechanism, for example, the rate-determining step under the changed reaction conditions. A smaller Tafel slope suggests that the rate-determining step is at the ending part of the multiple electron transfer reaction [243]. Both cobalt hydroxide and oxide on *Bekipor ST 20AL3* can be assessed as a highly effective and stable active material for OER, as their activity is very similar to that of nanocomposites [238,244] or metal-doped structures [245-251] synthesized by other authors.

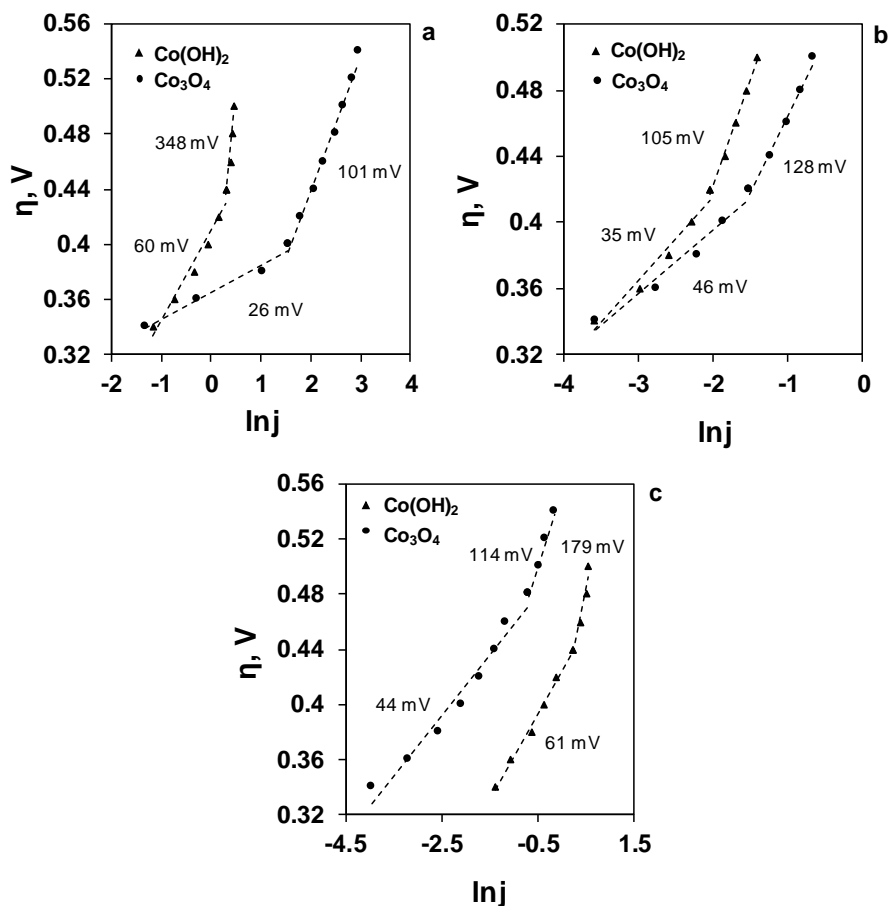


Fig. 3.11. Tafel plots of cobalt hydroxide and cobalt oxide on *Bekipor ST 20AL3* deposited from different electrolytes: *a* – cobalt nitrate, *b* – cobalt chloride, *c* – cobalt acetate

For a comparison of the electrocatalytic behavior of cobalt oxide coatings on *Bekipor ST 20AL3* in water oxidation, IrO₂ was taken into account as the benchmark from [252] (Fig. 3.12). When analyzing the results, a lower value of the onset potential is seen for IrO₂ (+0.5 V (+1.47 V vs. RHE)), whereas Co₃O₄ deposited on either AISI304 or *Bekipor ST 20AL3* exhibits exactly the same onset potential at +0.63 V (+1.6 V vs. RHE). The overpotential values of +0.48 V at a current density of 10 mA·cm⁻² are the same for IrO₂ and Co₃O₄ on *Bekipor ST 20AL3*; meanwhile, the overpotential of Co₃O₄ on AISI304 is only +0.82 V at 10 mA·cm⁻². When applying

the potential at higher values than +0.63 V, cobalt oxide on *Bekipor ST 20AL3* mesh exhibits significant values of the current density which are the result of its 3D structure with a high surface area.

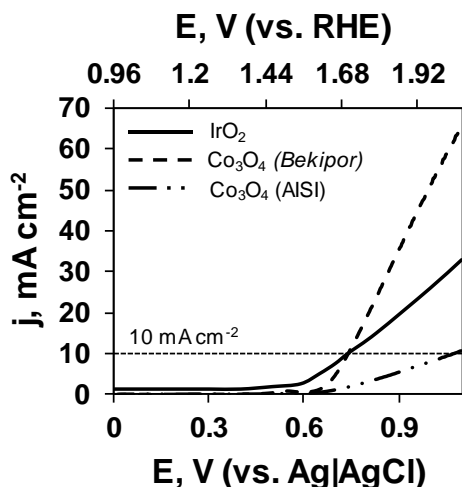


Fig. 3.12. Comparison of IrO_2 [252] and Co_3O_4 electrochemical activity in OER. The current density is calculated according to the geometric surface area. Supporting electrolyte – 0.1 M NaOH

3.1.3.3. Capacitive Properties of Cobalt (hydro)oxide Coatings on *Bekipor ST 20AL3*

Cobalt oxide compounds having a layered structure with large interlayer spacing proved to be an efficient catalyst for OER. Nevertheless, recently these compounds attract more and more attention as suitable active materials for supercapacitor applications. Pseudocapacitors (or supercapacitors) store energy by charge transfer between the electrode and the electrolyte because of the Faradaic reactions occurring on the surface of the active material; capacitance is determined by the electric charge transfer whose rate depends on the quantity of the active substance and the surface area of the transfer [221,223,253,254]. Supercapacitors provide a much longer lifecycle ($\sim 10^6$ cycles) and a shorter period of charge accumulation (~ 0.6 s) compared with electrochemical batteries or fuel cells. One of the major quantitative characteristic of supercapacitors is specific capacitance which strongly depends on the surface area of the active material and the pore size [254] as well as on the amount of the active material. In this chapter, for the evaluation of the capacitive characteristics of cobalt hydroxide deposited from different electrolytes, cyclic voltammetry tests were employed. The experiments were conducted in a 0.1 M NaOH supporting electrolyte at a potential window of $-0.2 \text{ V} \div +0.4 \text{ V}$ at a scan rate of $20 \text{ mV} \cdot \text{s}^{-1}$. The electric charge was estimated after calculating the integrals of the anodic or the cathodic part in time. The potential window was defined according to the anodic and cathodic electric charge values as both of them have to be equal.

Fig. 3.13 illustrates the first ten cyclic voltammograms of cobalt hydroxide coatings synthesized from three different precursors. The shapes of the curves in all of the cases are not rectangular and can be related to pseudocapacitance rather than to the double-layer capacitance [255]. The charge storing process takes place according to the following equations:



The values of the current density of coatings synthesized from nitrate, chloride and acetate precursors are similar. In all the cases, the first cycle generates the highest value of the current density due to the intensive oxidation of cobalt hydroxide. After the three initial cycles, the stability and repeatability of the voltammograms are reached, therefore, in order to ensure reliable values of specific capacitance, only the parameters of the tenth cycle were used.

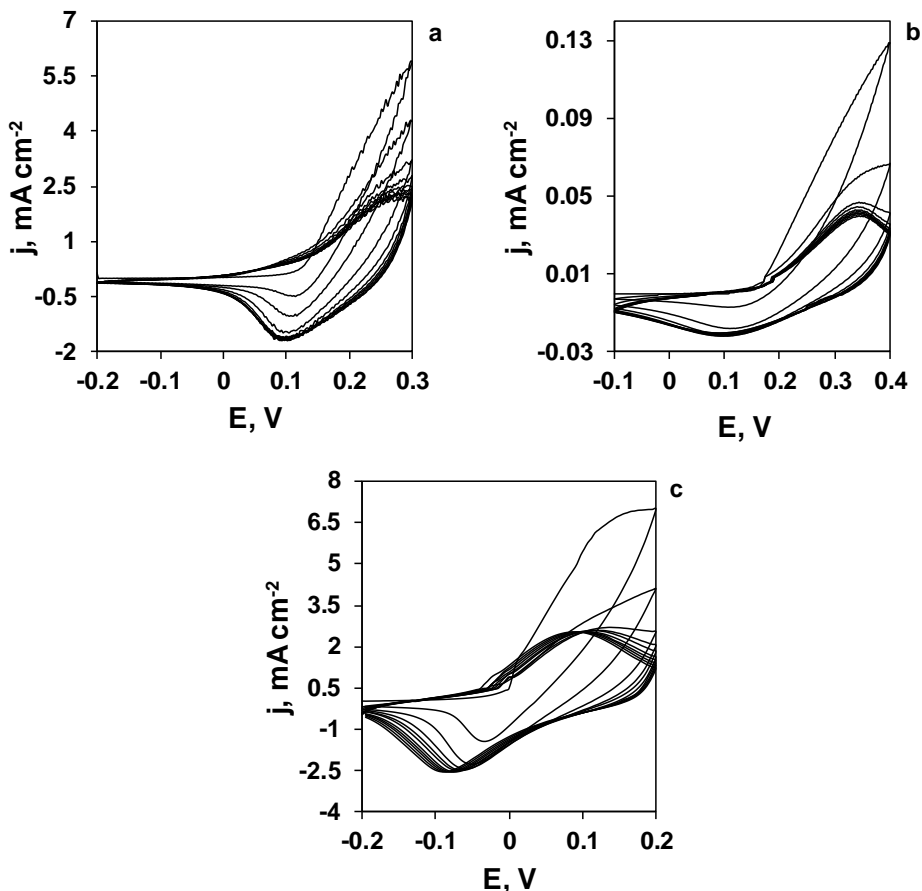


Fig. 3.13. Cyclic voltammograms of cobalt hydroxide films on *Bekipor ST 20AL3* deposited from different electrolytes: *a* – cobalt nitrate; *b* – cobalt chloride; *c* – cobalt acetate. Supporting electrolyte – 0.1 M NaOH, scan rate – 20 mV·s⁻¹

The specific capacitance was calculated by using the following equation [223]:

$$SC = \frac{Q}{\Delta E \cdot m}; \quad (3.14)$$

Here, Q is electric charge in coulombs, ΔE is the potential range in volts, and m is the active substance mass in grams. Table 3.3 illustrates the dependence between the specific capacitance and the mass of cobalt hydroxide. As it can be concluded from the results, the formation of coatings from the three sources of cobalt occur at different growth rates, which affects the capacitive behavior as well. The highest specific capacitance ($1324 \text{ F} \cdot \text{g}^{-1}$) was reached when using an electrolyte bath containing cobalt nitrate. The influence of the deposition time to a specific capacitance is clearly observed from the obtained results: synthesis which takes longer than 300 s has a negative effect on specific capacitance. The variation in the observed values of specific capacitance can be explained in terms of differences regarding the electroactive surface area, pore structure, presence of adsorbed ions and impurities [172]. For example, structure analysis revealed that cobalt hydroxide deposited from a chloride bath contains the highest amount of side-product consisting of potassium, cobalt and oxygen, which decreases the capacitive activity of the coating. Furthermore, deposition from the cobalt chloride electrolyte allows reaching the highest amount of electroactive materials. This can be related to the diffusional effects as the mobility of anions in water decreases in the order chloride > nitrate > acetate [256].

The highest value of specific capacitance for cobalt hydroxide deposited on AISI304 stainless steel was $490 \text{ F} \cdot \text{g}^{-1}$ [31]. The significant difference between the SC values of $\text{Co}(\text{OH})_2$ on the two substrates is observed and subsequently related to the a higher surface area of the stainless steel mesh.

Table 3.3. Capacitive characteristics of $\text{Co}(\text{OH})_2$ films on metal fiber filter *Bekipor ST 20AL3*. m is mass of cobalt hydroxide, c is a specific capacitance. Mass deviation $\pm 0.05 \text{ mg}$

Deposition time t, s	Electrolyte bath					
	0.05 M $\text{Co}(\text{CH}_3\text{COO})_2$		0.05 M $\text{Co}(\text{NO}_3)_2$		0.05 M CoCl_2	
	m, mg	c, $\text{F} \cdot \text{g}^{-1}$	m, mg	c, $\text{F} \cdot \text{g}^{-1}$	m, mg	c, $\text{F} \cdot \text{g}^{-1}$
60	0.2	237	0.05	822	0.3	202
120	0.3	812	0.1	1324	0.6	239
180	0.4	842	0.5	459	0.8	449
240	0.5	965	0.9	306	1.1	315
300	0.7	689	1.1	171	1.2	302
360	0.8	154	1.2	156	1.3	273

Cobalt oxide Co_3O_4 , which is well-known for its ability to store electric charge, was examined under the same conditions as $\text{Co}(\text{OH})_2$ to determine its capacitive properties. The ten obtained cyclic voltammograms were recorded in a potential window of $-0.1 \div +0.4 \text{ V}$ in 0.1 M NaOH supporting electrolyte, and the results are displayed in Fig. 3.14. When analyzing the obtained results, significantly better cycle stability is observed for oxide coatings synthesized from all the three precursors:

nitrate (a), chloride (b) and acetate (c). The drop of the current density between the first and the second cycles is 12–20%, while in the case of cobalt hydroxide this value reaches 61–66%. The capacitive behavior of Co_3O_4 outcomes from the succeeding reactions is as follows [255,257]:



Due to the narrow potential window, only the first stage of oxidation/reduction is likely to happen. Despite the good stability and cyclability, the values of the generated current density of Co_3O_4 differ up to 10 times from the ones of $\text{Co}(\text{OH})_2$. After conducting the calculations of the specific capacitance according to equation (3.14) within the range of $2\text{--}30 \text{ F}\cdot\text{g}^{-1}$, cobalt oxide seemed to be a less effective supercapacitor than cobalt hydroxide.

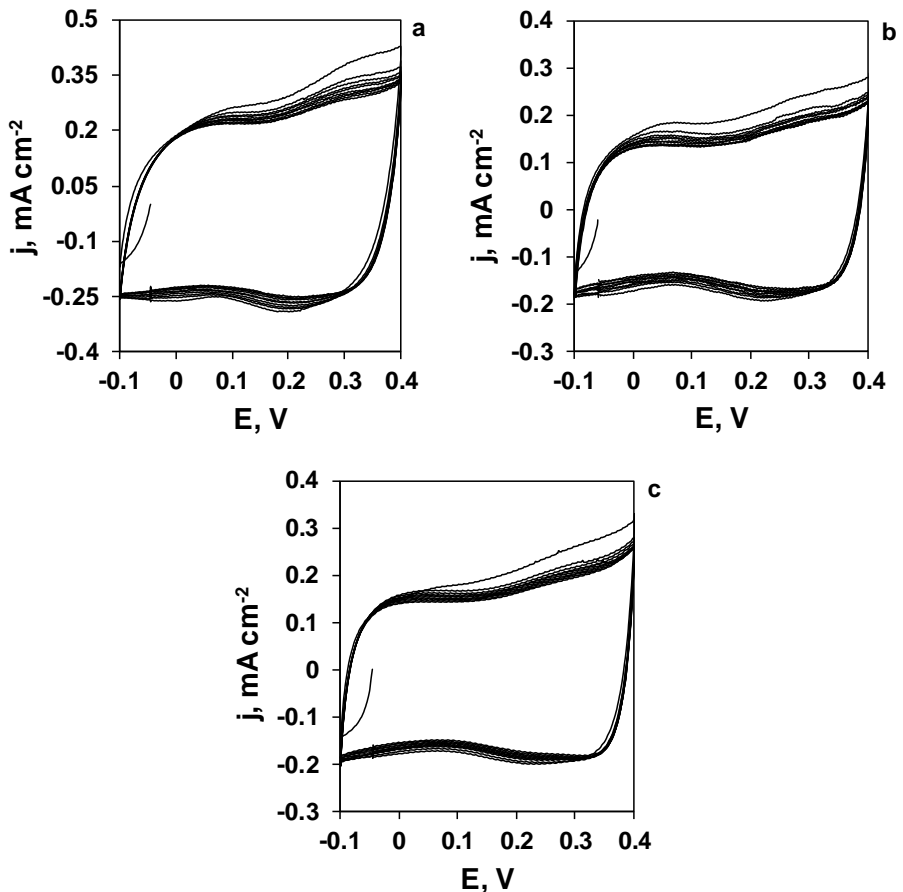


Fig. 3.14. Cyclic voltammograms of cobalt oxide films on *Bekipor ST 20AL3* deposited from different electrolytes: *a* – cobalt nitrate; *b* – cobalt chloride; *c* – cobalt acetate. Supporting electrolyte – 0.1 M NaOH, scan rate – $20 \text{ mV}\cdot\text{s}^{-1}$

Having conducted investigations of the electrochemical properties of cobalt oxide coatings, some conclusions can be drawn:

- Cobalt oxide coatings were synthesized by galvanostatic deposition on stainless steel mesh *Bekipor ST 20AL3* from three different precursors: nitrate, chloride and acetate. Our structure analysis revealed that as-deposited coatings are made of lamellar α -Co(OH)₂ layers containing anion impurities depending on the electrolyte used: nitrate, chloride and acetate. Spinel Co₃O₄ was obtained by annealing as-deposited coatings at 673 K for 1h. The nitrate precursor is distinguished with the least amount of impurities for both Co(OH)₂ and Co₃O₄ coatings.
- The kinetics of film growth and the approximate electroactive surface area were determined, which revealed that coatings from chloride and acetate precursors feature a superior growth rate to that of nitrate. It was established that during synthesis taking longer than 300 s, the space between fibers is clogged, and the surface area decreases.
- Co(OH)₂ and Co₃O₄ deposited from a nitrate bath displayed the best electrocatalytic activity in OER.
- The values of specific capacitance were evaluated from cyclic voltammograms. The highest SC value of 1324 F·g⁻¹ was determined for Co(OH)₂ deposited from a nitrate solution. Meanwhile, the high amount of impurities in coatings from chloride and acetate precursors has a negative effect on their capacitive activity. It should be noted that this value of SC should be treated with precaution as it is known that the pseudocapacity measurements by cyclic voltammetry can lead to rather significant deviations as compared to the values recorded by other methods.

The presented results in this chapter expand the knowledge in the field of cobalt (hydro)oxide electrochemistry. However, in order to obtain coatings with a higher electrocatalytic activity and pseudocapacitance, it is reasonable to synthesize mixed metal oxides. Taking into account the results of scholarly literature analysis, the next stage of this work was the electrodeposition of nickel-cobalt (hydro)oxide coatings.

3.2. Structure and Electrochemical Properties of Cobalt-Nickel Oxide Coatings

As both cobalt and nickel belong to the same group of transition metals and are similar not only in terms of chemical properties but also in terms of their electric conductivity and electronic structure, the composites of these elements are widely used and investigated worldwide. Transition metal oxides (TMO) are denoted by low costs and great elemental abundance; they have also demonstrated excellent electrochemical activities [258]. Particularly, TMOs based on Fe, Ni and Co are highly active for the oxygen evolution reaction in alkaline conditions due to being a great alternative to the most active, but unstable or denoted by low elemental abundance RuO₂ and IrO₂ [258]. When examining the capacitive properties of TMOs, they not only store energy like electrostatic carbon materials, but also exhibit electrochemical Faradaic reactions between electrode materials and ions within the

appropriate potential windows [174]. In this chapter, the structure and electrochemical properties of electrodeposited layered nickel-cobalt oxide coatings are investigated.

3.2.1. Electrochemical Synthesis of Layered Nickel-Cobalt (hydro)oxide

Previous experiments (Chapter 3.1) proved electrochemical deposition to be a reliable method for cobalt hydroxide synthesis. Therefore, it was decided to employ this method to compose layered mixed nickel-cobalt oxide coatings. Three different substrates were chosen: AISI304 stainless steel plates, FTO glass and *Bekipor ST 20AL3* stainless steel mesh.

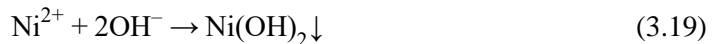
3.2.1.1. Electrodeposition of Nickel-Cobalt Hydroxides on AISI304 Plates

In previous experiments, the electrochemical synthesis of thin cobalt hydroxide films on stainless steel substrates was conducted by using the galvanostatic deposition method while employing three different sources of cobalt ions: acetate, nitrate and chloride electrolytes. The best catalytic and capacitive activity was demonstrated by the coatings deposited from a cobalt nitrate solution (Chapter 3.1), therefore, cobalt nitrate and nickel nitrate solutions were selected for use in the formation of mixed coatings.

Fig.3.15 shows the AISI304 stainless steel cyclic voltammogram in 0.05 M $\text{Co}(\text{NO}_3)_2$ + 0.05 M $\text{Ni}(\text{NO}_3)_2$ + 0.1 M KNO_3 solution; the inset presents the cyclic voltammogram of AISI304 plate in the solution consisting only of 0.05 M $\text{Co}(\text{NO}_3)_2$ + 0.1 M KNO_3 . The potential was firstly applied from the initial (at around -0.1 V) to the cathodic side so that to initiate the formation of nickel-cobalt hydroxide. The small cathodic peak C_1 is related to the electrogeneration of hydroxyl ions from nitrate on the surface of a stainless steel plate [62,259]:



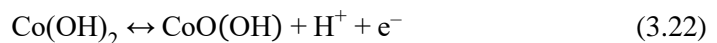
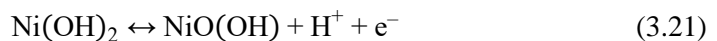
Due to the presence of hydroxyl ions, close to the electrode surface, the pH increases and enables the precipitation of nickel and cobalt hydroxides [259]:



The hysteresis loop in the cathodic area confirms the formation of insoluble compounds on the surface of AISI304 stainless steel plates. When sweeping the potential to the more negative than -1.0 V region, hydrogen evolution starts according to the following equation (peak C_2):



Further oxidation highlights an increase in the current density at $+0.7 \div +0.85$ V (anodic peak A_1) which is mainly assigned to the oxidation of deposits [33,37,259,260]:



Meanwhile, anodic peak A₂ at + 1V is associated to the further oxidation of the coating and the oxygen evolution reaction [243]:



The presence of nickel hydroxide changes the position and shape of anodic peaks: the peak which was at around +0.8 V in the cobalt curve changes its position in the nickel-cobalt curve and occurs at around +0.9 V. If comparing cobalt voltammogram (inset) with the one of nickel-cobalt, a significant decrease in the current density is observed which can be a consequence of the possible competition between cobalt and nickel ions. For this reason, the potentiostatic deposition was chosen instead of galvanostatic deposition. To determine the optimal potential values of the formation of nickel and cobalt layers, the chronopotentiograms of AISI304 plates were recorded in two separate electrolytes – cobalt nitrate and nickel nitrate (Fig.3.16). When analyzing the stainless steel plate behavior in a cobalt nitrate solution (Fig.3.16, 1), the stable potential value of –0.85 V was reached during galvanostatic deposition. Meanwhile, the optimal deposition potential value for the nickel hydroxide (Fig.3.16, 2) formation is more negative, and it reaches –1.15 V. Therefore, the potentiostatic deposition of layered nickel-cobalt hydroxide was performed by using the potential values of –0.85 V for cobalt and –1.15 V for nickel layer formation.

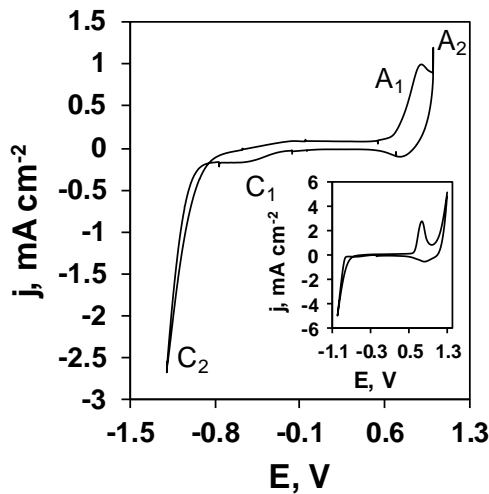


Fig. 3.15. Cyclic voltammogram of AISI304 stainless steel plate in 0.05 M $\text{Co}(\text{NO}_3)_2$ + 0.05 M $\text{Ni}(\text{NO}_3)_2$ + 0.1 KNO_3 electrolyte. Scan rate – 20 mV s^{-1} . Inset – cyclic voltammogram of AISI304 plate in 0.05 M $\text{Co}(\text{NO}_3)_2$ + 0.1 M KNO_3

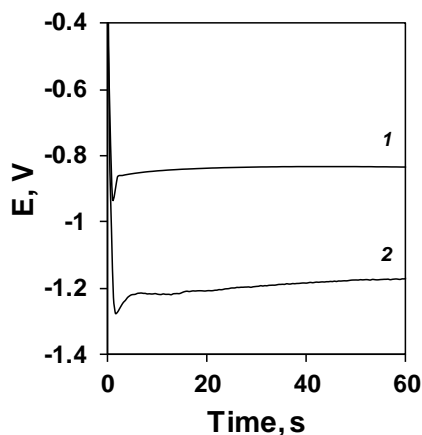


Fig. 3.16. Chronopotentiograms of AISI304 stainless steel plates in two different electrolytes: 1 – 0.05 M $\text{Co}(\text{NO}_3)_2 + 0.1 \text{ M KNO}_3$; 2 – 0.05 M $\text{Ni}(\text{NO}_3)_2 + 0.1 \text{ M KNO}_3$. Current density – 0.5 mA cm^{-2}

In order to determine the most stable coatings which could demonstrate advantageous catalytic and capacitive activity, different conditions of electrochemical deposition were applied. Firstly, it was necessary to identify the optimal duration of synthesis; for this purpose, various deposition times were adjusted: 60, 90, 120, 300 and 600 s. It was noticed that the smooth surface of coatings subjected to a longer than 120 s synthesis time while they are wet results in the coating starting to crack during the drying process, and, finally, it peels off from the surface. No such behavior was observed when working with the coatings consisting of only cobalt oxides, so the cracking might be a consequence of the presence of nickel layers. In order to ensure good adhesion between the coatings and the surface, no deposition was carried out longer than 120 s in the following experiments. The second step was to test various ratios of nickel and cobalt layers to form the preferable spinel structure NiCo_2O_4 after heat treatment; therefore, four different ways of deposition were selected providing coatings with different titles: Ni-Co-OH, Ni-2Co-OH, Ni-3Co-OH and Ni-Co-OH(-1V) (Table 3.4). Fig.3.17 demonstrates the chronoamperograms of potentiostatic deposition of layered nickel-cobalt hydroxide by applying two potential values (-0.85 V and -1.15 V) when undergoing changes in time. In all the layered nickel-cobalt oxide coatings, synthesis began from the formation of a cobalt layer to improve the adhesion with AISI304 plates. The average mass of the deposited coatings on AISI304 was $0.55 \text{ mg}\cdot\text{cm}^{-2}$ for Ni-Co-OH and $0.40 \text{ mg}\cdot\text{cm}^{-2}$ for Ni-2Co-OH.

Table 3.4. Detailed information of deposition parameters of mixed nickel-cobalt oxide coatings on AISI304.

Coating	Ni-Co-OH		Ni-2Co-OH		Ni-3Co-OH		Ni-Co-OH (-1V)				
Deposition process	100 seconds	Time, s	E, V	90 seconds	Time, s	E, V	80 seconds	Time, s	E, V		
		10	-0.85		20	-0.85		30	-0.85	90	-1
		10	-1.15		10	-1.15		10	-1.15		
		10	-0.85		20	-0.85		30	-0.85		
		10	-1.15		10	-1.15		10	-1.15		
		10	-0.85		20	-0.85					
		10	-1.15		10	-1.15					
		10	-0.85								
		10	-1.15								
		10	-0.85								
		10	-1.15								
		10	-0.85								
		10	-1.15								

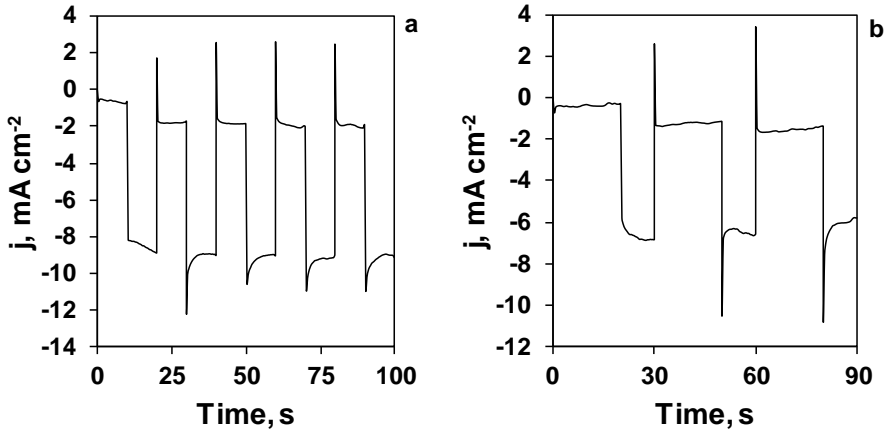


Fig. 3.17. Chronoamperograms of AISI304 in 0.05 M $\text{Co}(\text{NO}_3)_2$ + 0.05 M $\text{Ni}(\text{NO}_3)_2$ + 0.1 M KNO_3 forming mixed and layered Ni-Co-OH (a) and Ni-2Co-OH (b) coatings

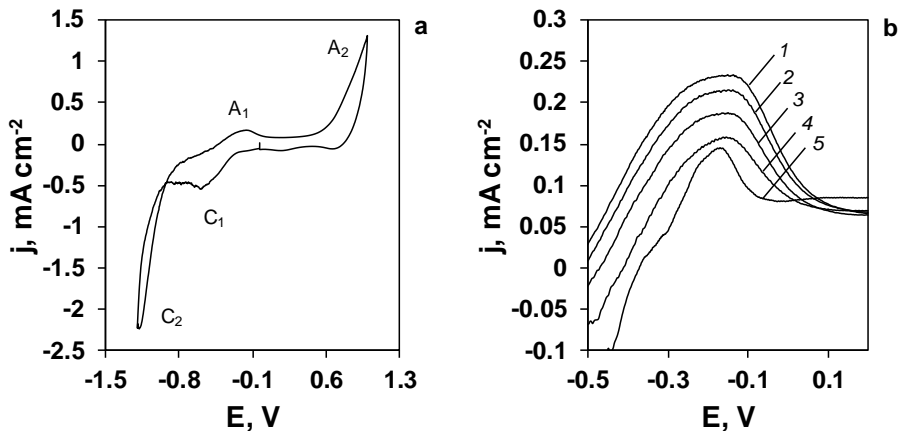
3.2.1.2. Electrodeposition of Layered Nickel-Cobalt Hydroxides on *Bekipor ST 20AL3* Mesh

The surface area is one of the main substrate characteristics affecting the morphology and properties of the deposited active substance. As reported in previous works [31,115], *Bekipor ST 20AL3* stainless steel mesh allows increasing the specific surface area as well as increasing the activity in electrocatalytic and pseudocapacitive applications. Nevertheless, even surface coverage must be ensured which must cover each filament of the 3D mesh separately without clogging the internal area. For this task, electrochemical deposition is one of the most suitable methods.

The main goal of this work was to form layered cobalt-nickel oxide structures featuring a spinel structure; therefore, only Ni-Co-OH and Ni-2Co-OH coatings were selected to be deposited on the substrates. The synthesis of layered nickel-cobalt

hydroxides on *Bekipor ST 20AL3* was performed under the same conditions as with AISI304 stainless steel by using potentiostatic deposition while applying two different potential values: -0.85 V for cobalt hydroxide layer deposition and -1.15 V for nickel hydroxide (Fig. 3.18, *c*). The experiments were performed in a 0.05 M $\text{Co}(\text{NO}_3)_2$ + 0.05 M $\text{Ni}(\text{NO}_3)_2$ + 0.1 M KNO_3 solution in ambient temperature. The detailed synthesis information is given in Chapter 3.2.1.1.

Fig. 3.18*a*, showing the cyclic voltammogram of the researched *Bekipor ST 20AL3* mesh in the deposition solution, highlights four peaks: two cathodic peaks and two anodic peaks. As with AISI304, C_1 peak is related with the nitrate ions reduction to NO_2^- except that it is much more intensive, which can be the result of the greater surface area. Peak C_2 is assigned to the deposition of cobalt and nickel insoluble hydroxides, which is confirmed by the hysteresis loop and the hydrogen evolution reaction. What concerns the investigation of the oxidation curve, anodic peak A_1 , which is mainly caused by nitrite ions oxidation to NO_3^- , constantly decreases with every scan but still remains after five scans (Fig. 3.18, *b*). This result reveals a different rate of the surface coverage for different stainless steel substrates: the AISI304 plate was covered after one cycle, meanwhile, due to the much larger surface area, the *Bekipor ST 20AL3* mesh still has uncovered zones after five cycles. The average mass of the deposited coatings on *Bekipor ST 20AL3* was 0.31 $\text{mg}\cdot\text{cm}^{-2}$ for Ni-Co-OH and 0.20 $\text{mg}\cdot\text{cm}^{-2}$ for Ni-2Co-OH coatings.



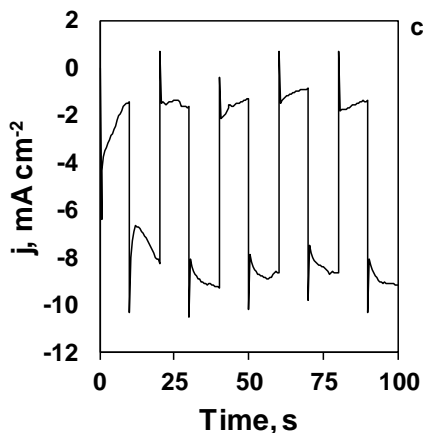


Fig. 3.18. The first (a) and the initial five (b) cyclic voltammograms and the chronoamperogram (c) of *Bekipor ST 20AL3* mesh in 0.05 M $\text{Co}(\text{NO}_3)_2$ + 0.05 M $\text{Ni}(\text{NO}_3)_2$ + 0.1 KNO_3 electrolyte. Scan rate – 20 mV s^{-1}

3.2.1.3. Electrodeposition of Layered Nickel-Cobalt Hydroxides on FTO Glass

There are many factors which affect the formation, morphology and characteristics of the deposited coatings. The origin of the substrate is one of the most important and influential parameters for electrochemical deposition forming mechanically stable coatings with the uniform surface. Fluorine-doped tin oxide (FTO), as the coating layer of a glass tray, is a material which is relatively stable under atmospheric conditions, chemically inert, high-temperature resistant and mechanically hard material. In addition, it is able to perform in a wider potential window without changing its properties. Because of these advantages, FTO glass was selected as a substrate to carry out further analysis of electrochemically deposited nickel-cobalt (hydro)oxides.

Fig. 3.19 demonstrates a cyclic voltammogram of FTO glass in a 0.05 M $\text{Co}(\text{NO}_3)_2$ + 0.05 M $\text{Ni}(\text{NO}_3)_2$ + 0.1 M KNO_3 solution. Basically, the shape and the nature of the curve are similar to the one of AISI304 and *Bekipor ST 20AL3*, but there are some differences which should be emphasized. Firstly, the current density of the voltammogram of FTO is noticeably lower comparing to the one of stainless steel. Two cathodic peaks can be attributed to nitrate ions reduction to nitrite ions (C_1) and to the deposition of nickel and cobalt hydroxides followed by hydrogen evolution (C_2). Meanwhile, anodic peak A_1 related to nitrite ions oxidation to nitrate ions is much more prominently expressed in the first cycle than in the AISI304 case, but it decreases and finally vanishes during further scans (Fig. 3.19, inset). This behavior can be explained with slower deposition and surface coverage on FTO glass, so, nitrate/nitrate ions from the solution can be found on the surface. As mentioned in Chapter 3.2.1.1, anodic peak A_2 is assigned to the oxidation of the deposits and oxygen evolution according to (3.21) – (3.23).

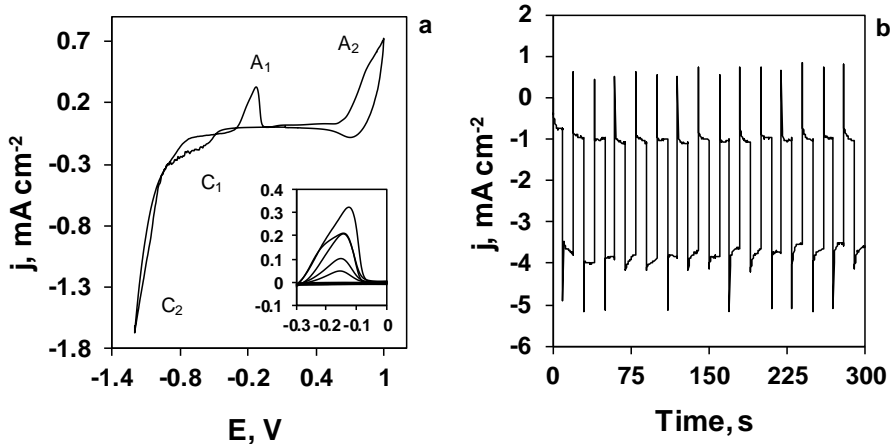


Fig.3.19. Cyclic voltammogram (a) and chronoamperogram (b) of FTO glass in a 0.05 M $\text{Co}(\text{NO}_3)_2$ + 0.05 M $\text{Ni}(\text{NO}_3)_2$ + 0.1 KNO_3 electrolyte. Scan rate 20 mV s^{-1}

While the cyclic voltammogram showed the slower deposition and surface coverage of FTO glass, the longer layered nickel-cobalt hydroxides synthesis was performed. The total duration of deposition was 5 minutes, and application to different potentials as with AISI304 stainless steel was implemented: -0.85 V for the cobalt hydroxide layer and -1.15 V for nickel hydroxide (Fig. 3.19, b). The average mass of the formed coatings on FTO glass was $0.42 \text{ mg}\cdot\text{cm}^{-2}$ for Ni-Co-OH and $0.33 \text{ mg}\cdot\text{cm}^{-2}$ for Ni-2Co-OH.

3.2.2. Structure Analysis of Nickel-Cobalt Oxide Coatings

The varying deposition conditions and ways affect the morphology, structure and stability of the deposited coatings. During the synthesis, it was observed that the mixed nickel-cobalt hydroxide coatings deposited by applying the constant potential of -1V were less mechanically stable, the surface had visible signs of cracking, and the coverage was uneven. For this reason, this coating was not used in further experiments, but it remained as an object whose structure is still necessary to investigate. The structure of all the as-deposited and annealed coatings was investigated with XRD, TG-DSC, AAS, Raman spectroscopy, SEM, EDS and XPS techniques. The obtained results are outlined in the following chapters.

3.2.2.1. X-ray diffraction analysis. Ni-Co-O, Ni-2Co-O, Ni-3Co-O and Ni-Co-O(-1V) films for XRD analysis were deposited on AISI304 plates and physically removed. Then, the obtained powders were annealed at 673 K for 1h. The XRD patterns of all the coatings (Fig. 3.20) demonstrate a number of reflections with various crystallographic intensities thus conforming the presence of spinel type NiCo_2O_4 (JCPDS data card No. 20-0781). Some small intensities of excess Co_3O_4 can be seen in Ni-2Co-O and Ni-3Co-O. It is inferred that Ni-Co-O and Ni-3Co-O are slightly less crystalline than Ni-2Co-O and Ni-Co-O(-1V) coatings. The average crystallite sizes calculated according to Debye-Scherrer's relation are given in Table 3.5.

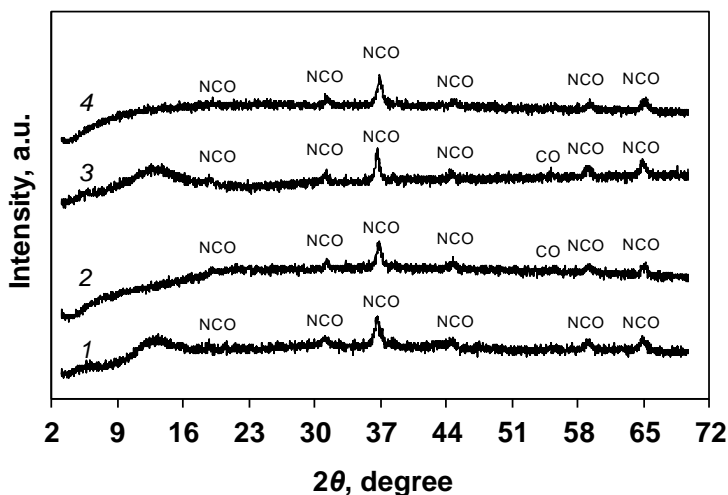


Fig. 3.20. XRD pattern of annealed at 673 K various nickel-cobalt oxide powders: 1 – Ni-Co-O; 2 – Ni-2Co-O; 3 – Ni-3Co-O and 4 – Ni-Co-O(-1V). Indexes: NCO – nickel-cobalt oxide NiCo_2O_4 , CO – cobalt oxide Co_3O_4

Table 3.5. Average crystallite size of mixed nickel-cobalt oxide coatings calculated according to Scherrer’s equation

Sample notation	$2\theta, ^\circ$	Average crystallite size, nm
Ni-Co-O	36.57	13.3±1
Ni-2Co-O	36.77	16.3±1
Ni-3Co-O	36.61	16.9±1
Ni-Co-O(-1V)	36.94	15.6±1

As the duration and kinetics of the formation of layered nickel-cobalt oxide coatings on FTO glass were distinguished from the ones on stainless steels, the XRD analysis of these products was performed (Fig. 3.21). The coatings on FTO glass differ in terms of small thickness; therefore, the peaks of the conductive layer of the substrate (tin oxide) are the most intensive. In as-deposited spectra for both Ni-Co-OH and Ni-2Co-OH (Fig.3.21, 1), only the peaks of cobalt hydroxide were identified, while the peaks of amorphous $\text{Ni}(\text{OH})_2$ [261] were not detected. Nevertheless, the presence of NiCo_2O_4 was determined in the annealed coatings (Fig.3.21, 2–4).

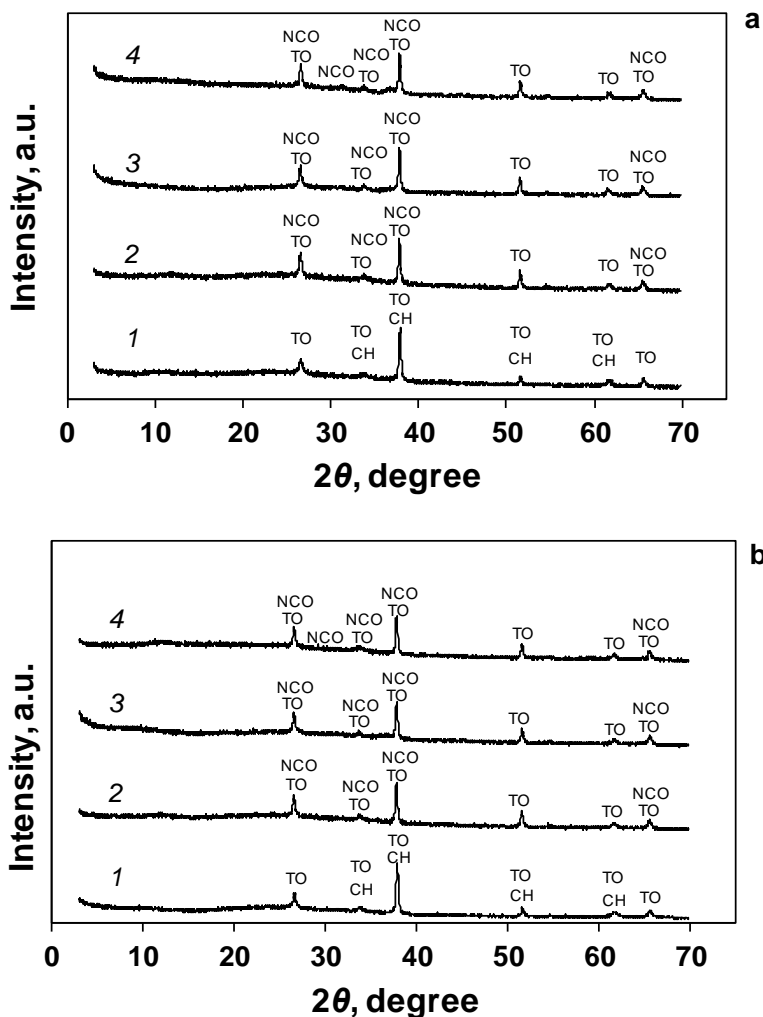


Fig. 3.21. XRD pattern of as-deposited (1) and annealed (2–4) nickel-cobalt oxide coatings on FTO glass. Annealing temperature: 2 – 473 K, 3 – 573 K, 4 – 673 K. Indexes: *NCO* – nickel-cobalt oxide NiCo_2O_4 , *CH* – cobalt hydroxide, *TO* – tin oxide (substrate)

3.2.2.2. TG-DSC analysis. The annealing effect to the coatings was evaluated from TG-DSC curves. Fig. 3.22 shows thermogravimetric (TG) and differential scanning calorimetry (DSC) analysis results of as-prepared Ni-Co-O and Ni-2Co-O samples electrochemically deposited on AISI304 and removed as powders. In both cases, the DSC curves reveal three endothermic effects in the temperature range of 326–1057 K. They are accompanied by the weight loss of about 36% (Ni-Co-O) and 33% (Ni-2Co-O). The first endothermic effects at 328–422 K (Ni-Co-O) and 326–402 K (Ni-2Co-O) are due to the evaporation of physically adsorbed and interlayer water molecules. The endothermic effects at 488–532 K (Ni-Co-O) and 491–535 K (Ni-2Co-O) can be associated with the decomposition of cobalt and nickel hydroxides

and the formation of spinel-type NiCo_2O_4 . The third endothermic peaks observed at 966–1057 K (Ni-Co-O) and 958–1056 K (Ni-2Co-O) can be related to the decomposition of spinel-type NiCo_2O_4 to two separate crystalline structures – Co_3O_4 and NiO [262].

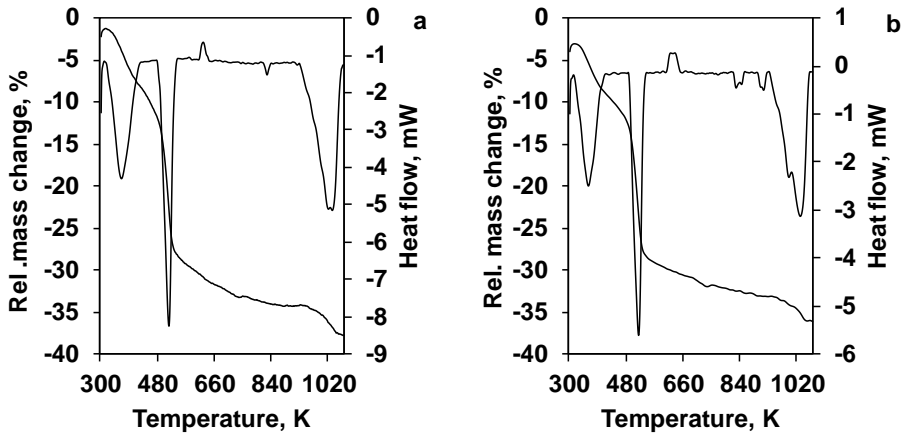


Fig.3.22. TG-DSC patterns of as-deposited Ni-Co-O (a) and Ni-2Co-O (b) samples

3.2.2.3. *Atomic absorption spectroscopy (AAS)* was carried out to determine the varying ratio of Ni:Co in as-prepared Ni-Co-OH coatings with different deposition times. It was determined that the average Ni:Co ratio is around 1:2.5, which allows to expect the spinel structure of NiCo_2O_4 in the annealed films.

Table 3.6. Ratio of Ni:Co in the Ni-Co-OH coatings measured by AAS

Sample notation	Atomic ratio Ni:Co in the Ni-Co-OH coatings
Ni-Co-OH	1 : 2.25
Ni-2Co-OH	1 : 2.50
Ni-3Co-OH	1 : 2.86
Ni-Co-OH, deposited at -1V	1 : 2.57

3.2.2.4. *Raman spectroscopy* was used to determine the structure properties of as-prepared (Fig. 3.23) and annealed at three different temperatures nickel-cobalt oxide coatings (Fig. 3.24). All the tested coatings were formed on AISI304 steel plates. Stainless steel consists mainly of Fe, Cr and Ni and tends to oxidize when immersed into aqueous solutions thus forming a thin oxide layer. Therefore, the Raman spectrum of uncoated AISI304 plates (Fig. 3.23, 1) was recorded to assess the impact of the substrate on the results. Two characteristic peaks were identified in this curve (408 cm^{-1} and 670 cm^{-1}) which were associated with the vibrations of the common hematite structure of iron and chrome oxides referred to as $(\text{Fe,Cr})_2\text{O}_3$ [263].

Fig. 3.23 showing the spectra of as-deposited Ni-Co-O (2) and Ni-2Co-O (3) coatings contains characteristic peaks at 456 cm^{-1} and 522 cm^{-1} associated with the vibrations of $\text{Co}(\text{OH})_2$ [37,264] and Ni-OH [42]. The small peak in Ni-2Co-O at 645 cm^{-1} can be related to the vibrations of $\text{CoO}(\text{OH})$ [37,260]. Furthermore, both spectra

of the as-deposited coatings show a small peak at 1045 cm^{-1} which can be assigned to the vibrations of $\alpha\text{-Ni(OH)}_2$ [42].

Meanwhile, the Raman spectra of all the annealed nickel-cobalt oxide coatings (Fig.3.24, 2–4) demonstrate overlaying signals of Co-O and Ni-O vibrations in the band of $470\text{--}640\text{ cm}^{-1}$ from which some more intensive signals can be marked: 465, 525, and 640 cm^{-1} . All of these peaks are associated to the vibrations of $\text{Ni}^{3+}\text{-O}$, $\text{Co}^{2+}\text{-O}$ and $\text{Co}^{3+}\text{-O}$ [265-271].

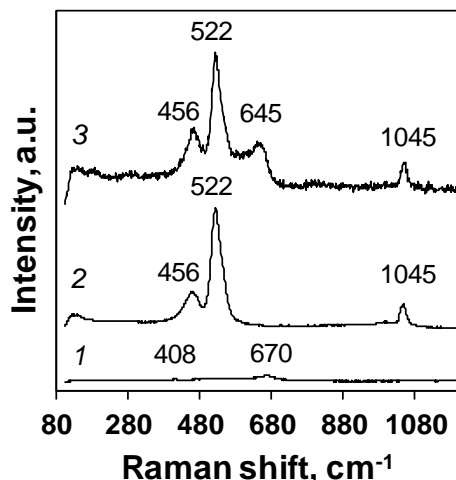


Fig. 3.23. Raman spectra of uncoated AISI304 steel plates (1) and as-deposited coatings of Ni-Co-O (2) and Ni-2Co-O (3)

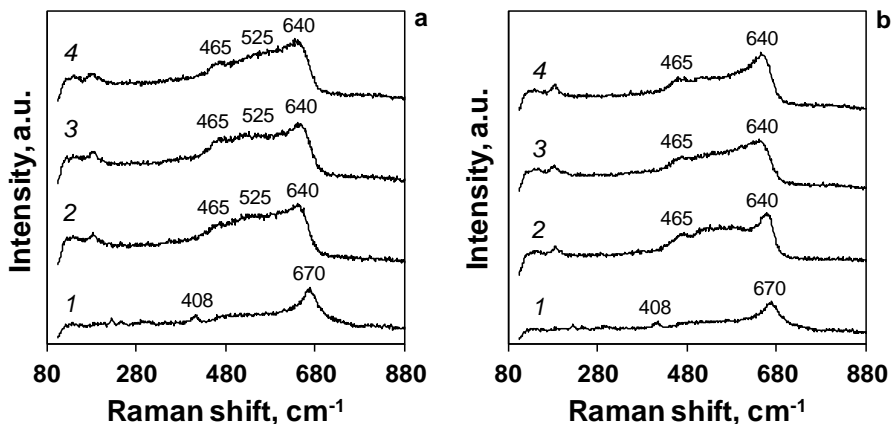


Fig. 3.24. Raman spectra of uncoated AISI304 steel (1) and coatings of Ni-Co-O (a) and Ni-2Co-O (b) annealed at different temperatures: 2 – 473 K; 3 – 573 K; 4 – 673 K

3.2.2.5. The representative *scanning electron microscopy (SEM)* images and element map generated by *energy-dispersive X-ray spectroscopy (EDS)* are displayed in Fig.3.25. The powdered form of the deposited on AISI304 steel annealed at 673 K

and mechanically removed layered nickel-cobalt oxide was used to avoid the signals of the substrate. As it can be seen in SEM images (Fig.3.25, *a*, *b*), the distinct clustering behavior at a lower magnification is detected, while, at a higher magnification, the lamellar structure can be observed. The element map (Fig.3.25, *c*, *d*) demonstrates the distribution between cobalt and nickel to be very close to the spinel-type oxide with stoichiometry NiCo_2O_4 . The EDS elemental analysis is given in Fig. 3.26 and Table 3.7, which mainly confirms the results of XRD and Raman analysis and identifies Co, Ni and O as the main elements of the annealed coatings with traces of side elements such as carbon, chlorine and sulphur.

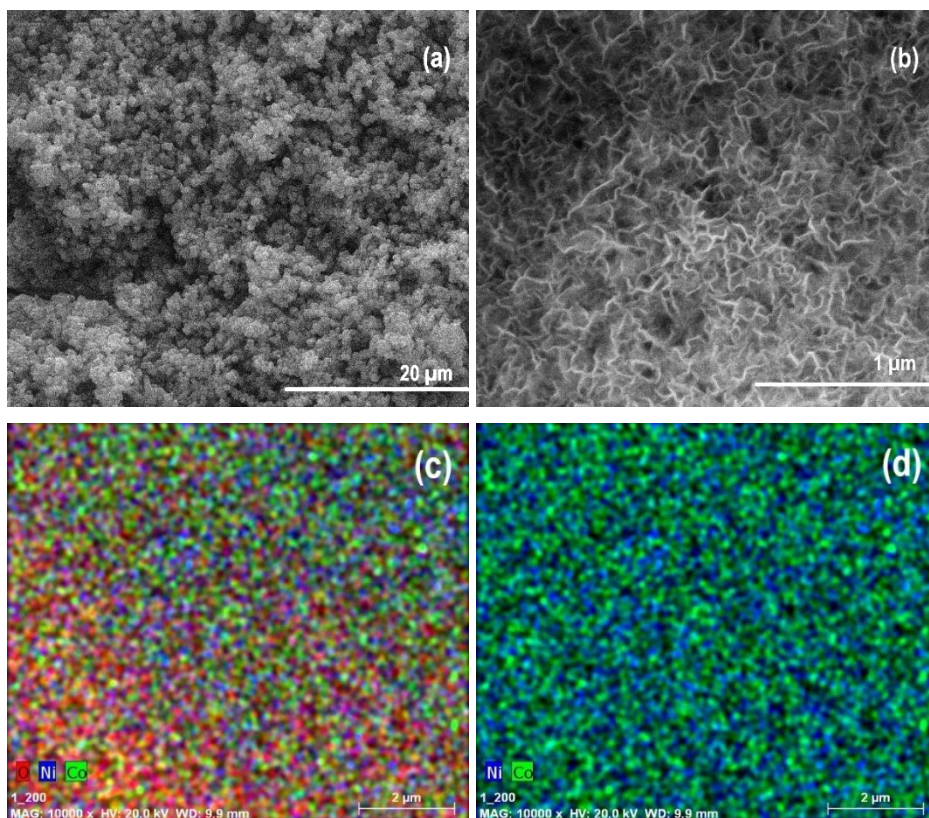


Fig. 3.25. SEM images at $\times 20000$ (*a*) and $\times 100000$ (*b*) magnification and EDS map (*c*, *d*) of Ni-Co-O powders

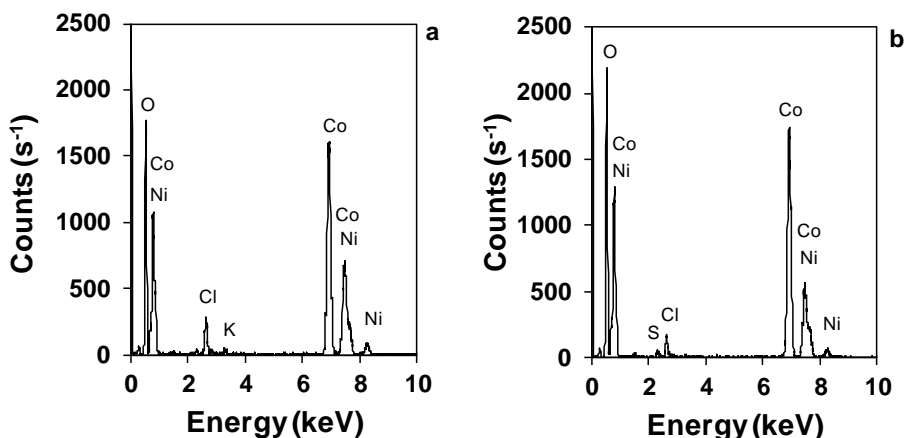


Fig. 3.26. EDS spectra of annealed at 673 K Ni-Co-O (a) and Ni-2Co-O (b) powder deposited on AISI304 plates

Table 3.7. Results of quantitative EDS analysis of Ni-Co-O and Ni-2Co-O powders deposited on AISI304

Element	Ni-Co-O	Ni-2Co-O
	Concentration (at. %)	Concentration (at. %)
Co	32.2	31.7
Ni	12.1	16.0
O	51.7	47.5
C	2.6	1.8
Cl	1.0	2.3
S	0.4	0.7

3.2.3. Electrochemical Characterization

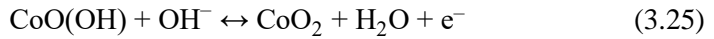
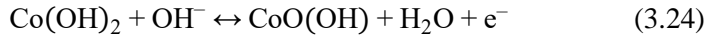
3.2.3.1. Electrocatalytic Activity in Oxygen Evolution Reaction

3.2.3.1.1 Cobalt-nickel oxide coatings on AISI304 stainless steel

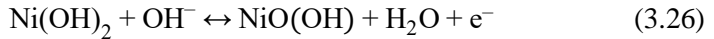
In the previous works [30,31], AISI304 stainless steel plates proved to be suitable support for cobalt oxide coatings deposition and primary investigations. It is an easily handled, cheap and relatively stable base in aqueous solutions. Due to these characteristics, AISI304 plates were chosen for the initial investigations of cobalt-nickel oxide coatings.

To assess the electrocatalytic activity of cobalt-nickel hydroxide coatings on AISI304 plates, linear sweep voltammograms in 0.1 M NaOH were recorded by applying the potential window from 0 V to +1.1 V (vs. Ag/AgCl) at the scan rate of 20 mV s⁻¹ (Fig.3.27). In order to ensure the even distribution of the electrolyte on the film's surface, the solution was constantly stirred. In all the linear sweep voltammograms, which includes cobalt hydroxide in their composition, the redox

peaks at around +0.25 ÷ +0.4 V are observed due to the oxidation of cobalt hydroxide [30,239]:



Along with cobalt hydroxide oxidation, nickel hydroxide conversion to oxyhydroxide occurs as well at around +0.5 V for pure Ni(OH)₂ coating, whereas, for layered Ni-Co-OH coatings, this peak can be shifted to the more negative side at +0.4 V [259,272]:



As it is seen from the results, as-deposited cobalt-nickel oxide coatings are distinguished by the best catalytic activity in OER reactions comparing to separate cobalt and nickel hydroxides. The advantage of Ni-Co-OH over Ni-2Co-OH might be related to the more favorable ratio between nickel and cobalt to the spinel structure in the annealed coatings. Besides, a significant difference between the activities of nickel and cobalt hydroxides can be spotted in Fig. 3.27. During the potentiostatic electrodeposition of these coatings, when the same duration of synthesis was applied, the mass of the deposited nickel hydroxide was three-time higher compared to the cobalt hydroxide mass. Usually, the current density in LSV is calculated by estimating the surface area instead of the mass. Therefore, the more intensive oxidation of Ni(OH)₂ occurring in the thicker hydroxide layer according to equation (3.26) enhances the total current density.

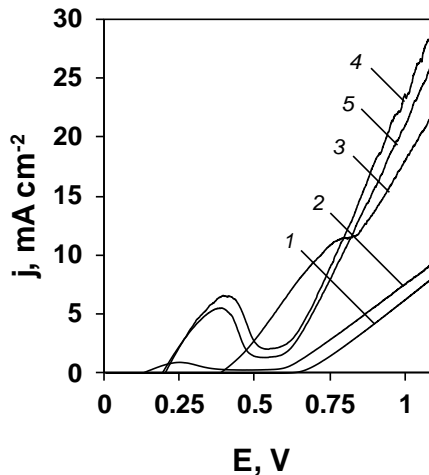


Fig. 3.27. Linear sweep voltammograms of as-deposited coatings on AISI304 plates in 0.1M NaOH: 1 – uncoated AISI304 plate, 2 – Co(OH)₂, 3 – Ni(OH)₂, 4 – Ni-Co-OH, 5 – Ni-2Co-OH. Scan rate – 20 mV·s⁻¹

It was reported that nickel-cobalt spinel oxides intrinsically catalyze oxygen evolution reactions, are stable in an alkaline environment, and that Ni and Co are more abundant and less expensive than the noble metals [273]. The formation of nickel-

cobalt spinel oxides depends on the calcination temperature [273,274]; therefore, five different temperatures were selected for annealing according to the TG-DSC effects (Fig. 3.22): 473, 573, 673, 773 and 1073 K. In order to determine the impact of annealing on the activity in OER, linear sweep voltammograms of temperature treated Ni-Co-O and Ni-2Co-O coatings were recorded (Fig. 3.28).

Fig. 3.28 revealed that spinel-type nickel-cobalt oxide coatings annealed at 573 K and 673 K along with as-deposited nickel-cobalt hydroxide coatings demonstrate the best electrocatalytic activity for both Ni-Co-O and Ni-2Co-O ratios. However, the observed current of as-deposited nickel-cobalt hydroxide in OER can be partly related to the continuous oxidation reaction of both cobalt and nickel hydroxides to oxyhydroxides [223,227,275]. A peak around +0.4V for the as-deposited nickel-cobalt coating is related to cobalt hydroxide oxidation and is characteristic to the one in the as-deposited cobalt hydroxide LSV curve (Chapter 3.1.3.2); meanwhile, from around +0.75V, nickel hydroxide oxidation to NiO(OH) occurs. Due to these reactions, the real electrochemical activity of hydroxide coatings in OER cannot be evaluated from LSV. Nickel-cobalt oxide coatings annealed at 473K also show a small oxidation peak at +0.4V which can be associated with the same oxidation processes as there is some part of hydroxide remaining in their structure after calcination. As it can be seen in Fig.3.28, there is a reasonable drop of the current density in the LSV curves of Ni-Co-O and 2Ni-Co-O annealed at 773 K and 1073 K. This decrease is related to the decomposition of spinel-type NiCo₂O₄ and the formation of two separate oxides: NiO and Co₃O₄.

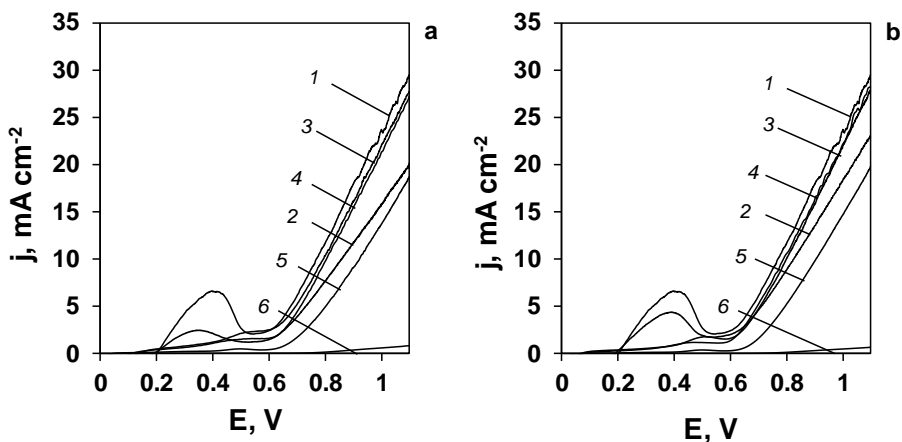


Fig. 3.28. Linear sweep voltammograms of annealed Ni-Co-O (a) and Ni-2Co-O (b) coatings on AISI304 plates in 0.1M NaOH with different annealing temperature: 1 – without treatment (as-deposited), 2 – 473 K, 3 – 573 K, 4 – 673 K, 5 – 773 K, 6 – 1073 K. Scan rate – 20 mV·s⁻¹

When concluding the LSV results, IrO₂ was taken as a benchmark from [252] to evaluate the electrocatalytic properties of annealed at 673 K nickel-cobalt oxide coatings on AISI304 plates. Separate cobalt oxide and nickel oxides polarization curves were also taken into consideration so that to understand the relation between the structure and the electrocatalytic properties. All the linear sweep voltammograms

are shown in Fig. 3.29. According to the obtained results, the onset potential of iridium oxide (+0.5 V (+1.47 V vs. RHE)) is lower than the ones of cobalt and nickel coatings on AISI304, all of which exhibit the same onset potential of +0.63 V (+1.6 V vs. RHE). However, the activity of Ni-Co-O and Ni-2Co-O is close to the benchmark IrO₂ as their overpotential value is 530 mV, while the discussed substances are considerably cheaper and deposited on a low-cost and easy-handling substrate – stainless steel plates. Meanwhile, separate Co₃O₄ and NiO are much less effective, which proves that the common structure of cobalt and nickel, especially spinel NiCo₂O₄, is distinguished with significantly higher electrochemical activity and is an effective catalyst in water oxidation processes.

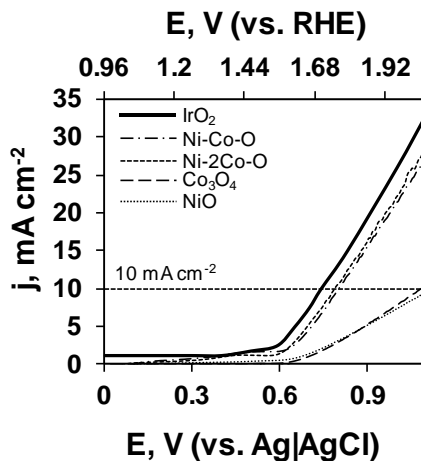


Fig. 3.29. Linear sweep voltammograms of annealed at 673 K Ni-Co-O, Ni-2Co-O, Co₃O₄ and NiO coatings on AISI304 plates. Benchmark – IrO₂ electrodes [252]. Supporting electrolyte – 0.1M NaOH. Scan rate – 20 mV·s⁻¹

In order to evaluate the electrocatalytic behavior of nickel-cobalt oxide coatings in the oxygen evolution reaction, controlled potential electrolysis was conducted in a 0.1 M NaOH solution at various applied potentials (Fig. 3.30). According to the linear sweep voltammetry results (Fig. 3.28), Ni-Co-O and Ni-2Co-O annealed at 573 K were chosen for this test. The electrolyte solution was being continuously stirred, and, after each measurement, the electrode was allowed to reach its steady-state potential. The collected current-potential data was used to construct its Tafel plot (Fig. 3.31). It is well known that the Tafel equation possesses fundamental importance in electrochemical kinetics, and that slope b is an indicative parameter of the electrode reaction mechanism [243]. Overpotential η was calculated according to equation (3.11).

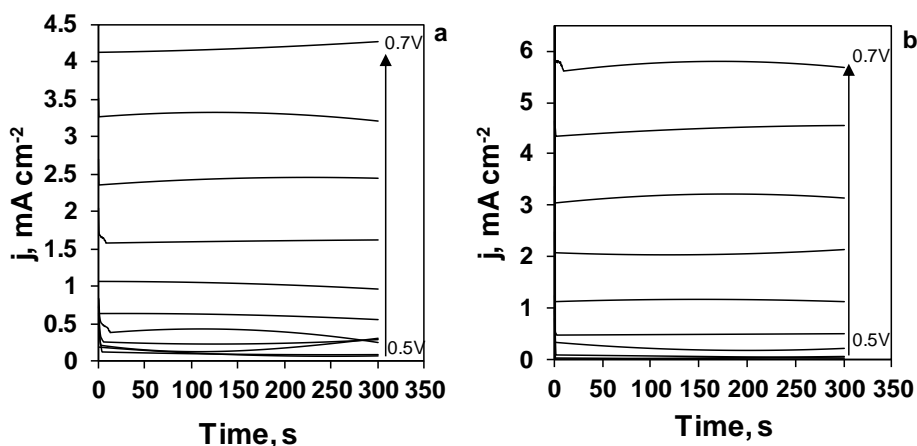


Fig. 3.30. Characteristic voltammograms of Ni-Co-O (a) and Ni-2Co-O (b) deposited on AISI304 stainless steel, annealed at 573 K for 1h. Supporting electrolyte – 0.1 M NaOH

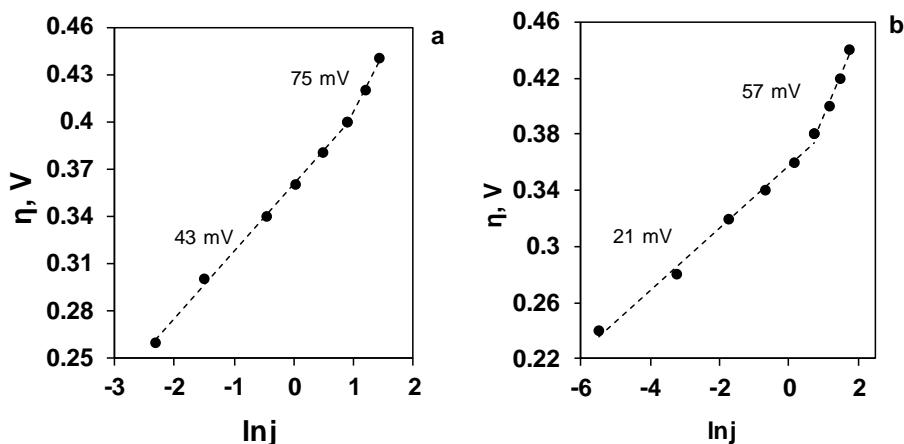


Fig. 3.31. Tafel plots of Ni-Co-O (a) and Ni-2Co-O (b), deposited on AISI304 stainless steel and annealed at 573 K for 1h

Fig. 3.31 presents the dependence of the overpotential as a function of the logarithm of the current density for nickel-cobalt oxide electrodes. Both coatings, Ni-Co-O and Ni-2Co-O, show an abrupt change of the Tafel slope at overpotential values higher than +0.40 V and +0.38 V, respectively: from 43 to 75 mV for the Ni-Co-O coating and from 21 to 57 mV for Ni-2Co-O coating. The switch of the Tafel slope can be considered as an indication of the change of the reaction mechanism, for example, the rate-determining step under changed reaction conditions. A smaller Tafel slope suggests that the rate-determining step is at the ending part of the multiple-electron transfer reaction, which is commonly a sign of a good electrocatalyst [243]. The obtained results show that mixed nickel-cobalt oxide coatings on AISI304 stainless steel can be assessed as a highly effective and stable electrode for OER, with

the activity being very similar to the results obtained by other authors using mixed cobalt-nickel oxide catalysts [276-280].

3.2.3.1.2 Cobalt-nickel oxide coatings on *Bekipor ST 20AL3* stainless steel mesh

During previous experiments, stainless steel mesh *Bekipor ST 20AL3* proved to be a highly effective and mechanically as well as chemically stable substrate for catalytic and capacitive purposes [31,230]. Although it served well when depositing cobalt oxide coatings and even though all of its qualities allowed improving the properties of coatings (Chapter 3.1), the synthesis of layered cobalt-nickel oxide films is a more complicated and complex target. The usage of a stainless steel mesh may allow increasing the surface area, but the layered structure may fail to be achieved. A complete description of the deposition of nickel-cobalt oxide coatings on *Bekipor ST 20AL3* mesh is given in Chapter 3.2.1.2.

In order to compare the electrocatalytic properties of different active materials deposited on a stainless steel mesh, the polarization curves were obtained. Linear sweep voltammograms (Fig. 3.32) were recorded in a potential window from 0 to +1.1 V while using 0.1 M NaOH as the supporting electrolyte. The values of the current density were calculated by using only the geometric surface area of the mesh instead of the active surface area due to the complexity of evaluation. Our review of the obtained results indicates that the best electrocatalytic activity in oxygen evolution is reached when using the Ni-2Co-O coating as an active material. The activity of Ni-Co-O and Co(OH)_2 is virtually equal when applying a potential higher than +0.6 V, but their behavior in the lower potential region is different. Cobalt hydroxide shows only a small peak at +0.2 V, which is related to the oxidation of hydroxide to oxyhydroxide, but the presence of Ni in the layered Ni-Co coatings increases their oxidation current significantly thus changing the position (+0.3 ÷ +0.4 V) and the shape of the peaks.

Stainless steel itself proved to be a reasonably active catalyst in the water splitting process promoting oxygen evolution; therefore, it is not a surprise that uncoated *Bekipor ST 20AL3* mesh (Fig. 3.32, 1) generates reasonably high values of the current density during the polarization. However, a mesh coated with Ni(OH)_2 seemed to exhibit the lowest activity, which may be related to the rapid growth of the coating and to the clogging of the space between the mesh filaments. The results are the decreased surface area and the loss of the 3D structure.

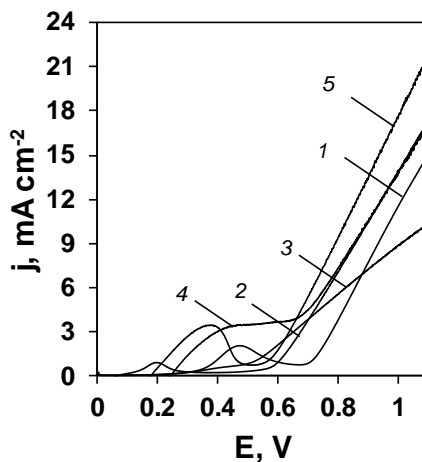


Fig. 3.32. Linear sweep voltammograms of as-deposited coatings on *Bekipor ST20AL3* mesh in 0.1M NaOH: 1 – uncoated *ST20AL3* mesh, 2 – $\text{Co}(\text{OH})_2$, 3 – $\text{Ni}(\text{OH})_2$, 4 – Ni-Co-OH , 5 – Ni-2Co-OH . Scan rate – $20 \text{ mV} \cdot \text{s}^{-1}$

As it was investigated in the previous chapter (3.2.3.1.1), temperature treatment maintains considerable influence on the activity of the films catalyzing oxygen evolution, therefore, layered nickel-cobalt hydroxide coatings on *Bekipor ST 20AL3* were annealed by applying five different temperatures: 473, 573, 673, 773 and 1073 K according to the TG-DSC curves (Fig.3.22). As with the films deposited on AISI304, all the annealed coatings on the stainless steel mesh are distinguished with different electrocatalytic activity as they were polarized in 0.1 M NaOH in a potential window of $0 \div +1.1 \text{ V}$. The obtained results (Fig.3.33) revealed that, unlike the AISI304 case, the temperature treatment at 673K not only increases the chemical stability of active materials but also significantly increases the activity in OER. Temperatures lower and higher than 673 K have a negative effect on the electrocatalytic activity; meanwhile, in the case of AISI304, the best values were reached with the coatings annealed at 473 or 573 K. Although the regularities of Ni-Co-O and Ni-2Co-O activity slightly differ, it might be related to the different distribution of cobalt oxide and nickel oxide on the surface of the mesh while it is not necessarily a layered structure.

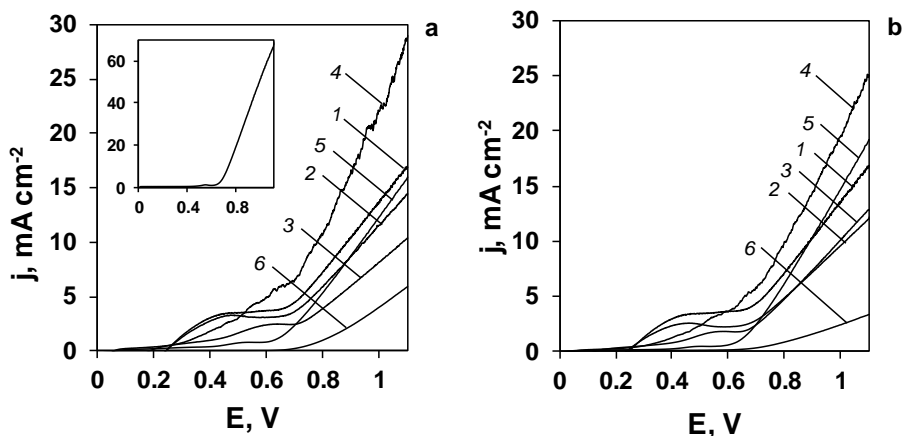


Fig. 3.33. Linear sweep voltammograms of annealed Ni-Co-O (a) and Ni-2Co-O (b) coatings on *Bekipor ST 20AL3* stainless steel mesh in 0.1M NaOH with different annealing temperature: 1 – without treatment (as-deposited), 2 – 473 K, 3 – 573 K, 4 – 673 K, 5 – 773 K, 6 – 1073 K. Scan rate – $20 \text{ mV} \cdot \text{s}^{-1}$. Inset in part a – linear sweep voltammogram of Co_3O_4 on *Bekipor ST 20AL3* annealed at 673 K

Nickel-cobalt oxide obtained after thermal treatment at 673 K showed the best electrocatalytic activity for both Ni-Co-O (a) and Ni-2Co-O (b); therefore, these films were selected to compose Tafel plots (Fig. 3.34). In order to collect the required data, controlled potential electrolysis was conducted in 0.1 M NaOH electrolyte at various potentials (Fig. 3.34) under the same conditions as with coatings deposited on AISI304 stainless steel plates (Chapter 3.2.3.1.1). Electrolysis results illustrate a small difference between the activities of Ni-Co-O (Fig. 3.34, a) and Ni-2Co-O (Fig. 3.34, b) as a higher amount of cobalt in the film's composition produces a slightly greater current density.

Tafel plots (Fig. 3.35) revealed that the curves change their slope at the potentials of +0.38 V as it was observed during the experiments with AISI304. The values of Tafel parameter b are slightly smaller for Ni-Co-O coating thus distinguishing it from the AISI304 values where Ni-2Co-O demonstrated the results that are more advantageous. This inequality arises mainly from the uneven distribution between cobalt and nickel oxide layers on *Bekipor ST 20AL3*.

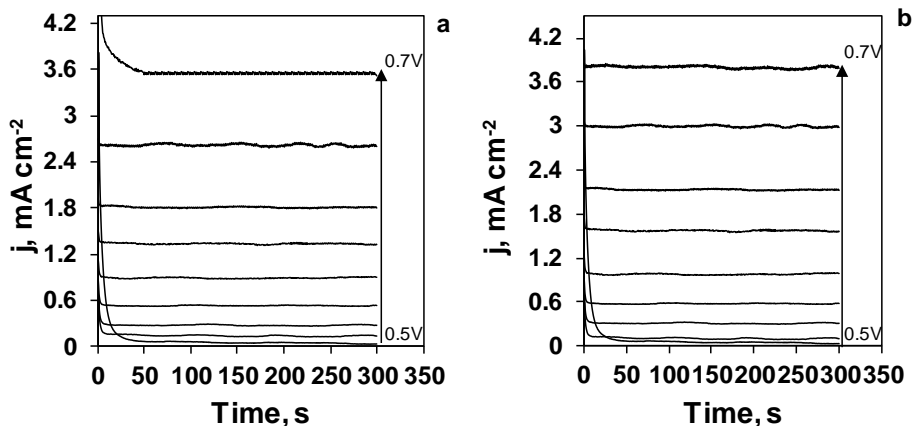


Fig. 3.34. Characteristic voltammograms of Ni-Co-O (a) and Ni-2Co-O (b) deposited on *Bekipor ST 20AL3* stainless steel mesh annealed at 673 K for 1h. Supporting electrolyte – 0.1 M NaOH

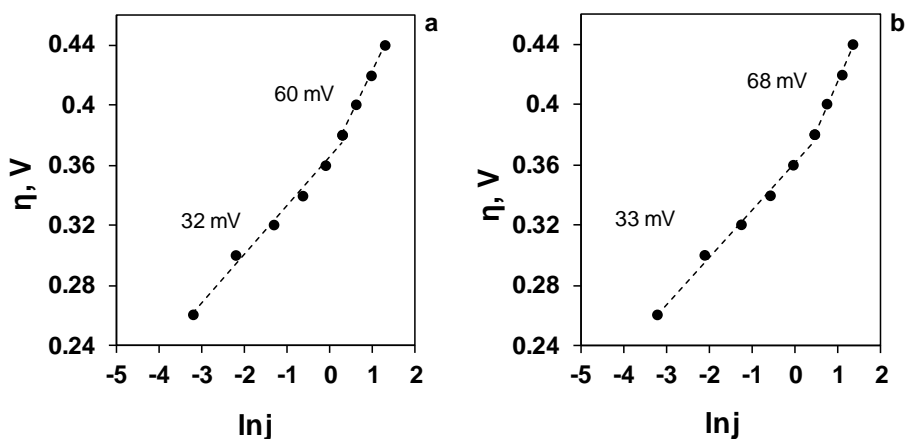


Fig. 3.35. Tafel plots of Ni-Co-O (a) and Ni-2Co-O (b) deposited on *Bekipor ST 20AL3* stainless steel mesh and annealed at 673 K for 1h

3.2.3.1.3 Cobalt-nickel oxide coatings on FTO glass

There is a perceptible relation between the substrate properties and the formation and morphology of the electrochemically deposited coatings. Many factors can affect the peculiarities of the deposited coating: adhesion properties, conductivity, and the origin of the substrate. It was observed that nickel from stainless steel substrates catalyzes the production of hydroxide ions [281], which leads to the more rapid growth of the coating during the same period. For these reasons, a completely different from stainless steel substrate was chosen to evaluate the influence of the tray to the properties of the coatings. A proper description of the layered cobalt-nickel hydroxide coatings electrodeposition on FTO glass procedure is given in Chapter 3.2.1.3.

In order to estimate the electrocatalytic activity of as-deposited cobalt-nickel hydroxide coatings on FTO glass, linear sweep voltammetry was conducted in 0.1 M NaOH (Fig. 3.36) by applying the potential window from 0 V to +1.1 V. The electrolyte solution was intensively stirred to avoid the surface coverage with oxygen bubbles. The synthesis of coatings on FTO was quite difficult due to the weak adhesion between the substrate surface and the film layers, as well as due to the small growth rate. It took 300 s instead of 90–100 s to reach the same mass values for 1 cm² as in SS substrate cases. Although other synthesis parameters were the same, the morphology of the coatings on FTO and SS substrates was discovered to differ. The coatings deposited on AISI304 stainless steel and *Bekipor ST 20AL3* show better catalytic ability in OER than those deposited on FTO glass even with the elimination of the current density of uncoated substrates. Unlike AISI304 and *Bekipor ST 20AL3* substrates, the Co(OH)₂ coating demonstrates the highest activity in OER, whereas the presence of nickel seems to decrease the generated current density of the coatings. The layered structure did not provide the expected increase in the current density as the values of the current density of Ni-Co-O, Ni-2Co-O and Ni(OH)₂ are very close. This regularity could be related to the sluggish and complicated growth of the nickel hydroxide layer.

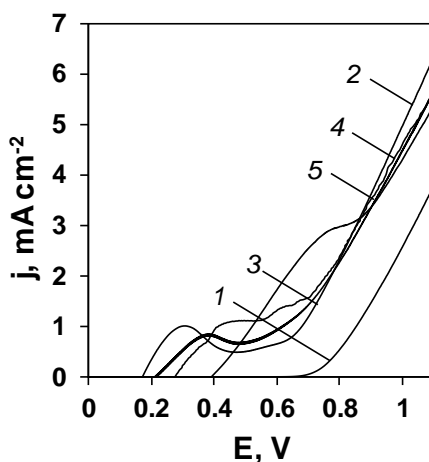


Fig. 3.36. Linear sweep voltammograms of as-deposited coatings on FTO glass in 0.1M NaOH: 1 – uncoated FTO glass, 2 – Co(OH)₂, 3 – Ni(OH)₂, 4 – Ni-Co-OH, 5 – Ni-2Co-OH. Scan rate – 20 mV·s⁻¹

Previous experiments (Chapters 3.2.3.1.1 and 3.2.3.1.2) revealed that temperature treatment increases the stability of nickel-cobalt oxide coatings without negative effects on their electrocatalytic performance in OER. For this reason, the same LSV investigations were established with the coatings deposited on FTO glass and annealed at various temperatures. From the results shown in Fig. 3.37, some assumptions can be made. Initially, in both Ni-Co-O and Ni-2Co-O coatings, annealing at 573 K increases the generated current density the most. Secondly, the activity of Ni-Co-O is slightly higher than the one of Ni-2Co-O. The possible excess of cobalt oxide after the thermal treatment seems to have a negative effect on the

common NiCo_2O_4 electrocatalytic behavior. Thirdly, all the curves on FTO glass retain the same shape as on AISI304 and *Bekipor ST 20AL3* while having small peaks from +0.38 V to +0.6 V (as explained in Chapters 3.2.3.1.1 and 3.2.3.1.2). In addition, it is obvious that annealing at higher temperatures than 573 K has a negative effect on the electrocatalytic properties. Moreover, it was observed that 1073 K temperature is too high for FTO glass, and that some signs of melting occurred although AISI304 stainless steel sustained this temperature without any damage.

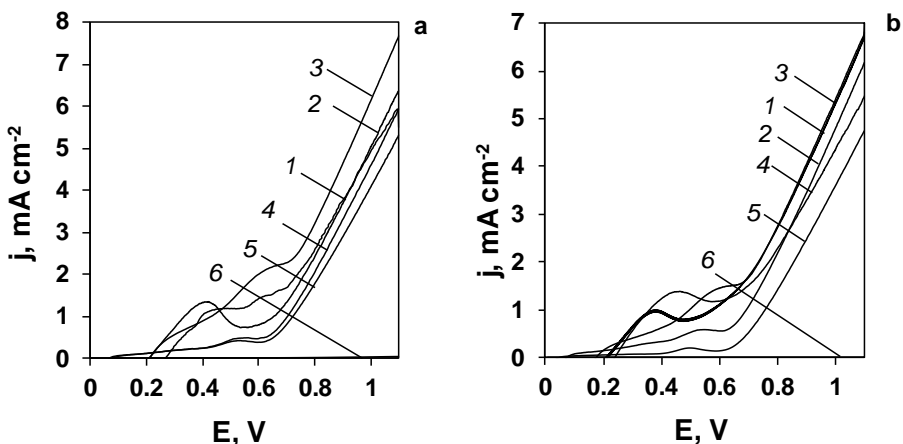


Fig. 3.37. Linear sweep voltammograms of annealed Ni-Co-O (a) and Ni-2Co-O (b) coatings on FTO glass in 0.1M NaOH with different annealing temperature: 1 – as-deposited, 2 – 473 K, 3 – 573 K, 4 – 673 K, 5 – 773 K, 6 – 1073 K. Scan rate – $20 \text{ mV} \cdot \text{s}^{-1}$

In order to assess the electrocatalytic behavior of nickel-cobalt oxide coatings on FTO glass in the OER reaction, Tafel plots (Fig. 3.39) were constructed for both Ni-Co-O (a) and Ni-2Co-O (b) films. To collect the required data, controlled potential electrolysis was conducted in a 0.1 M NaOH electrolyte at various potentials (Fig.3.38) under the same conditions as with the coatings deposited on stainless steel substrates (Chapters 3.2.3.1.1 and 3.2.3.1.2).

As we can see from the electrolysis results, the Ni-Co-O coating produces slightly higher values of the current densities comparing with the Ni-2Co-O coating. The quantitative evaluation of the electrocatalytic behavior of the coatings was determined by the calculation of the Tafel slopes (Fig. 3.39). Ni-2Co-O shows a greater activity while having relatively lower parameter b values (34 and 73 mV), whereas the ones of Ni-Co-O are slightly higher (41 and 88 mV). Anyway, all these values demonstrate the effectiveness of both coatings as the catalysts in the oxygen evolution reaction.

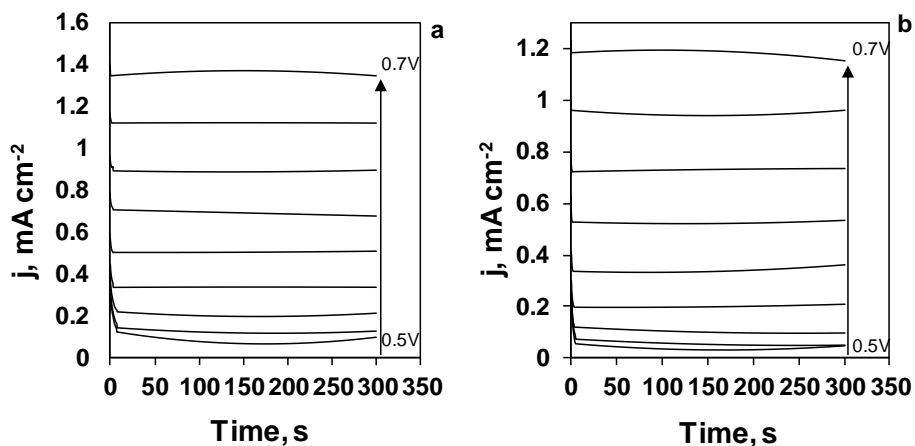


Fig. 3.38. Characteristic voltammograms of Ni-Co-O (a) and Ni-2Co-O (b) deposited on FTO glass plates annealed at 573 K for 1h. Supporting electrolyte – 0.1 M NaOH

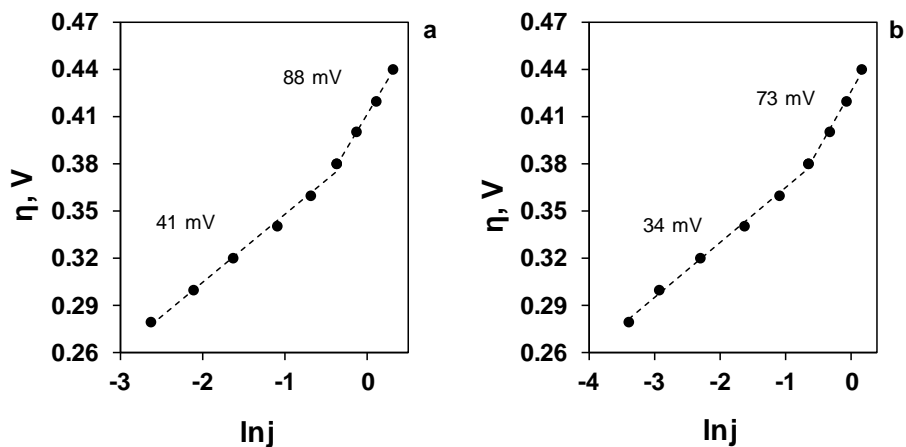
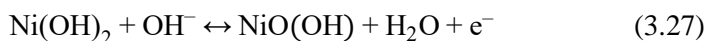


Fig. 3.39. Tafel plots of Ni-Co-O (a) and Ni-2Co-O (b) deposited on FTO glass plates and annealed at 573 K for 1h

3.2.3.2. Pseudocapacitive Properties of Layered Nickel-Cobalt Oxide Coatings

In the previous works, cobalt hydroxide and oxide proved to be promising active materials for capacitive applications. Nickel, as a close element to cobalt by nature and properties, oxide compounds are a good alternative to RuO_2 due to their easy synthesis, relatively high specific capacitance (a theoretically estimated value of $3750 \text{ F}\cdot\text{g}^{-1}$), environment friendliness and low cost [173,174]. The redox reaction of nickel hydroxide and oxide in a KOH electrolyte can be expressed as follows [174,272]:



However, the capacitive activity of nickel oxide strongly depends on its crystallinity [174]. Ni porous structure is unsatisfactory because it can limit the transportation of the electrolyte ions, which leads to slow electrochemical processes in charge storage and delivery [174]. The study of the relation between the annealing temperature and the specific capacitance of NiO was carried out by Cheng *et al.* [188] who determined that the best specific capacitance of nickel oxide is achieved when the calcination temperature range is 473–573 K. There are some other challenges in using nickel oxide compounds for capacitive applications, one of which is the poor cycle stability of nickel hydroxide. Meanwhile, nickel oxide demonstrates a better cycle performance with smaller losses of specific capacitance. However, the electrical conductivity of nickel oxide is rather low, however, the introduction of cobalt ions into the nickel oxide matrix may help to improve the conductivity [174].

In order to evaluate the capacitive properties of layered nickel-cobalt (hydro)oxide coatings on different substrates, galvanostatic charge/discharge (GCPL) measurements were performed.

To synthesize nickel-cobalt oxide, as-deposited coatings were annealed at different temperatures: 473, 573, 673, 773 and 1073 K. The average mass of the annealed active material is given in Table 3.8.

Table 3.8. The average mass of deposited and annealed nickel-cobalt oxide on different substrates

Substrate	Sample	Deposition time, s	Average mass of active material, mg·cm ⁻²					
			as-deposited	473 K	573 K	673 K	773 K	1073 K
AISI304	Ni-Co-O	100	0.55	0.48	0.40	0.37	0.36	0.34
	Ni-2Co-O	90	0.40	0.36	0.29	0.27	0.26	0.25
Bekipor ST 20AL3	Ni-Co-O	100	0.31	0.27	0.22	0.21	0.20	0.19
	Ni-2Co-O	90	0.20	0.18	0.15	0.13	0.13	0.12
FTO	Ni-Co-O	300	0.42	0.37	0.30	0.29	0.28	–
	Ni-2Co-O	300	0.33	0.30	0.24	0.22	0.22	–

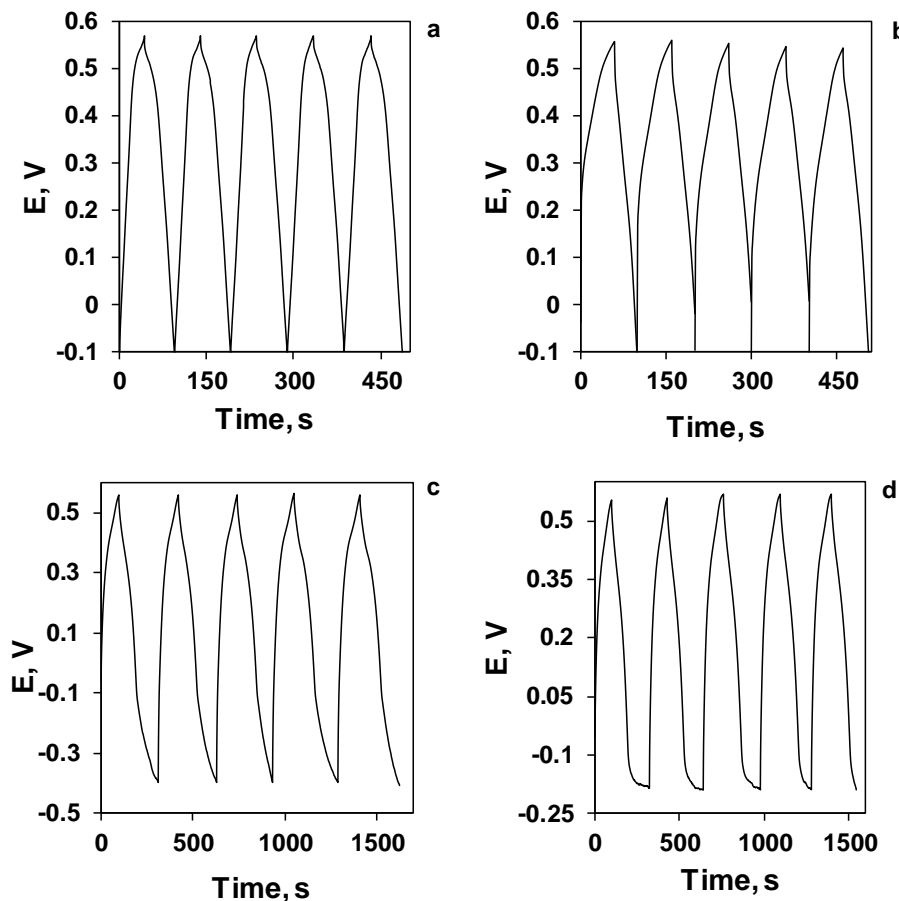
3.2.3.2.1 Pseudocapacitive behavior of layered nickel-cobalt oxide coatings on AISI304

In the previous chapters, the pseudocapacitive characteristics of cobalt hydroxide and oxide were investigated by using the data collected from cyclic voltammograms. Although it is a recognized and relatively accurate method, galvanostatic charge/discharge is a more common and informative technique to evaluate the capacitive parameters of the active substance. Therefore, this method was used in the determination of the capacitive properties of all the layered nickel-cobalt hydro(oxide) coatings deposited on all the three different substrates: AISI304 stainless steel plates, Bekipor ST 20AL3 stainless steel mesh and FTO glass.

To start with, AISI304 stainless steel plates were selected for the basic determination of the layered nickel-cobalt (hydro)oxide specific capacitance as they proved to be a stable, highly conductive support, on which, the stable coatings with uniform distribution are formed. One of the main tasks of this work was to investigate

the layered nickel-cobalt oxide structures featuring the spinel structure. Therefore, only the coatings annealed at different temperatures were selected for further investigation. Galvanostatic cycling with potential limitation (GCPL) analysis was performed in a potential range of $-0.3 \div +0.6$ V in a 0.1 M NaOH solution at $1 \text{ A} \cdot \text{g}^{-1}$.

During the evaluation of the electrocatalytic activity in OER, nickel-cobalt oxides were determined to be a much more active catalyst than separate Co_3O_4 and NiO. The charge/discharge experiments and the calculations of the capacitive parameters revealed the advantageous behavior of nickel-cobalt oxides as well (Fig.3.40 and Table 3.9).



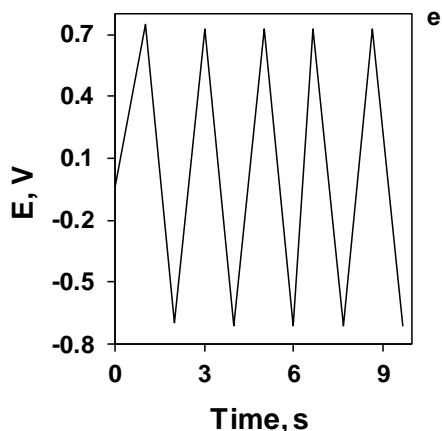


Fig. 3.40. Galvanostatic charge/discharge of annealed at 673 K for 1 h AISI304 plate in 0.1 M NaOH solution covered with different coatings: *a* – Co_3O_4 , *b* – NiO, *c* – Ni-Co-O, *d* – Ni-2Co-O, *e* – uncoated plate. Current density – $1 \text{ A}\cdot\text{g}^{-1}$

The main quantitative parameters of the supercapacitors – specific capacitance SC ($\text{F}\cdot\text{g}^{-1}$), specific energy SE ($\text{Wh}\cdot\text{kg}^{-1}$) and specific power SP ($\text{W}\cdot\text{kg}^{-1}$) – are given in Table 3.9. The values were evaluated according to the (1.32), (1.33) and (1.34) equations, respectively. The calculation of the specific capacitance confirmed the advantage of layered nickel-cobalt oxide coatings comparing to the values of separate oxides tested under the same conditions. When comparing Ni-Co-O and Ni-2Co-O, the higher amount of cobalt in Ni-2Co-O increases the SC but lowers the specific energy and the specific power, which indicates the rate of the generation of electric impulse. However, when reviewing the current supercapacitors which typically produce $5\text{--}10 \text{ Wh}\cdot\text{kg}^{-1}$ [282], the obtained values of nickel-cobalt oxides seem to demonstrate a promising result.

Table 3.9. Quantitative capacitive parameters of as-deposited cobalt and nickel hydroxide coatings and uncoated AISI304 plate

Coating	ΔV , V	t_D , s	Δm , mg	I , A	SC , $\text{F}\cdot\text{g}^{-1}$	SE , $\text{Wh}\cdot\text{kg}^{-1}$	SP , $\text{W}\cdot\text{kg}^{-1}$
Co_3O_4	0.65	52	1.6	0.0016	80	4.7	325
NiO	0.65	48	2.1	0.0021	74	4.3	325
Ni-Co-O	0.96	195	2.32	0.00232	203	26	480
Ni-2Co-O	0.82	219	1.9	0.0019	267	25	410
AISI304	1.4	1	1.8	0.0005	0.0002	$5.4\cdot 10^{-5}$	0.2

During the previous measurements of the electrocatalytic activity of annealed nickel-cobalt oxide coatings, the relation between the calcination temperature and the activity of the coatings was proven. It was related to the different morphology and structure of the films which can be confirmed from the effects in the TG-DSC curves (Fig. 3.22). The capacitive properties strongly depend on the crystallinity of the active substance [174]; therefore, the endothermic/exothermic peaks in the TG-DSC curves

allowed selecting five temperature values for further experiments: 473, 573, 673, 773 and 1073 K. The results of the galvanostatic charge/discharge analysis of the annealed coatings are given in Fig. 3.41. The best capacitive activity is demonstrated by the Ni-Co-O and Ni-2Co-O coatings annealed at 473–573 K where the formation of the spinel structure is the most likely. Ni-2Co-O has the advantage over Ni-Co-O due to the greater amount of cobalt oxide, which enhances the total electric conductivity. Further thermal treatment reaching temperatures higher than 473 K has a detrimental effect on the specific capacitance, as it can be seen in Table 3.10.

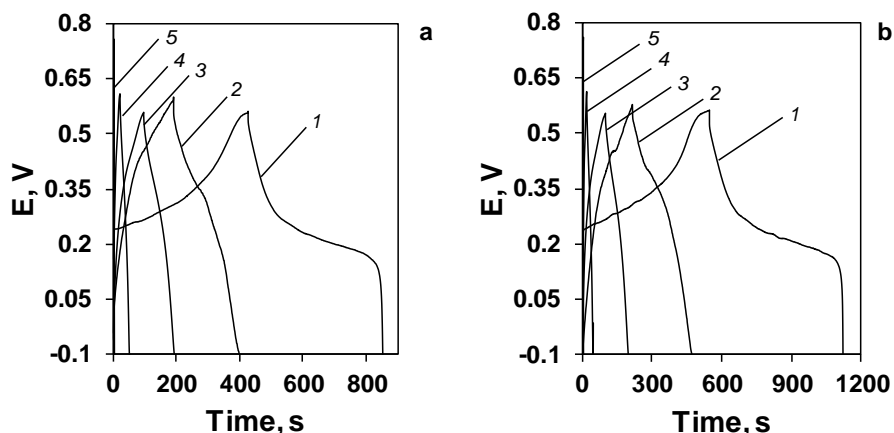


Fig. 3.41. Galvanostatic charge/discharge curves of Ni-Co-O (a) and Ni-2Co-O (b) films on AISI304 annealed for 1h at different temperatures: 1 – 473 K, 2 – 573 K, 3 – 673 K, 4 – 773 K, 5 – 1073 K. Current density $1 \text{ A} \cdot \text{g}^{-1}$

Table 3.10. Capacitance parameters of nickel-cobalt oxide coatings on AISI304 annealed at different temperatures

Coating	Annealing temperature, K	Specific capacitance SC , $\text{F} \cdot \text{g}^{-1}$	Specific energy SE , $\text{Wh} \cdot \text{kg}^{-1}$	Specific power SP , $\text{W} \cdot \text{kg}^{-1}$
Ni-Co-O	as-deposited	3.3	1.1	760
	473	400	125	750
	573	406	52	480
	673	203	26	480
	773	40	2.9	128
	1073	1.8	0.6	312
Ni-2Co-O	as-deposited	6.8	2.1	740
	473	402	126	750
	573	396	53	490
	673	267	25	410
	773	15	1.12	130
	1073	0.64	0.22	312

The good cyclability is one of the most important parameters of pseudocapacitors showing their shelf life. Ni-Co-O on the AISI304 plate annealed at

673 K for 1h was chosen to investigate the long-term cycle stability (Fig. 3.42). The experiment was run at a current density of $1 \text{ A} \cdot \text{g}^{-1}$ for 50 cycles. The results confirmed reasonably good cycle stability of this coating as its specific capacitance maintains 96.6% of its initial value.

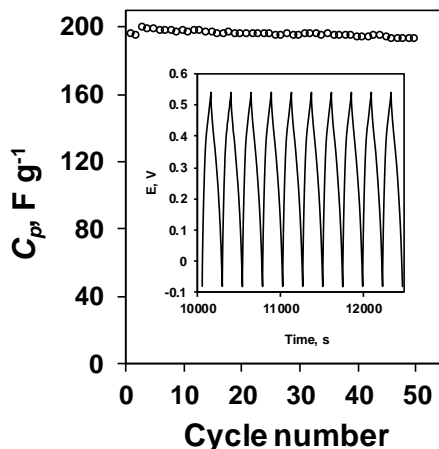


Fig. 3.42. Long term cycling performance of Ni-Co-O film on AISI304 annealed at 673 K. Inset: galvanostatic charge/discharge curves of the last 10 cycles of the Ni-Co-O film on AISI304 annealed at 673 K at the current density of $1 \text{ A} \cdot \text{g}^{-1}$

3.2.3.2.2 Pseudocapacitive behavior of layered nickel-cobalt oxide coatings on *Bekipor ST 20AL3* mesh

Pseudocapacitance is determined by the electric charge transfer whose rate depends on the quantity of the active substance and the surface area of the transfer [223,253,254]. During the investigations of the cobalt oxide pseudocapacitive properties, *Bekipor ST 20AL3* enabled to achieve three-to-four times higher values of the specific capacitance due to its great surface area. Although the even contribution of cobalt and nickel oxides on the stainless steel mesh might not be guaranteed, a 3D structure with a high surface area and permeability of the electrolyte possesses some potential of showing promising results. Therefore, *Bekipor ST 20AL3* was chosen for conducting further investigations. As it was determined in Chapter 3.1.3.1, the electroactive surface area of the SS mesh is $6 \text{ cm}^2/\text{cm}^2$.

The galvanostatic charge/discharge curves of nickel-cobalt oxide coatings on *Bekipor ST 20AL3* annealed at various temperatures are presented in Fig. 3.43, and the calculations of capacitive parameters are given in Table 3.11. Once again, the excess of cobalt oxide increases the discharge time as well as the specific capacitance. All the SC values are higher for Ni-2Co-O comparing with Ni-Co-O, and the highest value is $769 \text{ F} \cdot \text{g}^{-1}$ for the Ni-2Co-O film annealed at 473 K. When comparing other energetic parameters, such as the specific energy and the specific power, the results are more complex as the highest specific power is provided by the same Ni-2Co-O coating (annealed at 473 K), but generally Ni-Co-O coatings have higher SP values than Ni-2Co-O. The behavior regularities of layered nickel-cobalt (hydro)oxide

coatings on *Bekipor ST 20AL3* are similar to the coatings deposited on AISI304, although, due to the increased surface area, the stainless steel mesh is more advantageous.

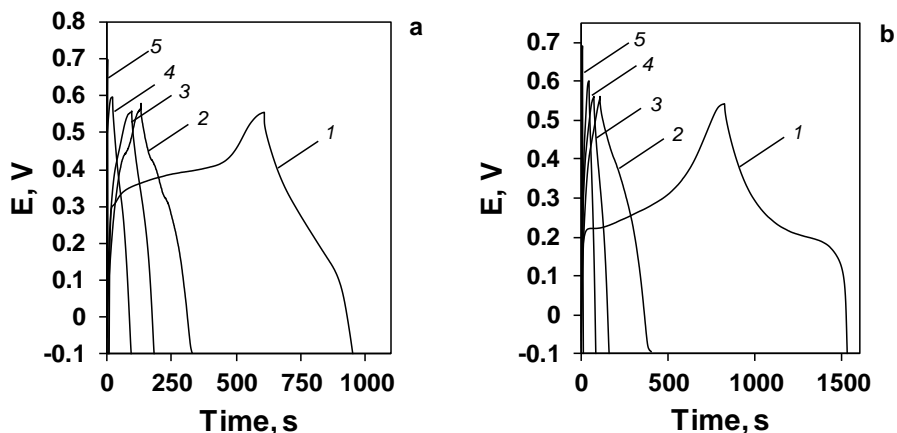


Fig. 3.43. Galvanostatic charge/discharge curves of Ni-Co-O (a) and Ni-2Co-OH (b) films on *Bekipor ST 20AL3* annealed for 1h at different temperatures: 1 – 473 K, 2 – 573 K, 3 – 673 K, 4 – 773 K, 5 – 1073 K. Current density – $1 \text{ A}\cdot\text{g}^{-1}$

Table 3.11. Capacitive parameters of nickel-cobalt oxide coatings on *Bekipor ST 20AL3* mesh

Coating	Annealing temperature, K	Specific capacitance SC, $\text{F}\cdot\text{g}^{-1}$	Specific energy SE, $\text{Wh}\cdot\text{kg}^{-1}$	Specific power SP, $\text{W}\cdot\text{kg}^{-1}$
Ni-Co-O	as-deposited	4.5	0.625	500
	473	539	168	750
	573	349	37	437
	673	140	9.5	350
	773	138	31	635
	1073	5	1	575
Ni-2Co-O	as-deposited	7.8	0.9	450
	473	769	312	855
	573	450	27	330
	673	135	8.7	340
	773	122	24	600
	1073	8	1.2	520

When reviewing the obtained results of the nickel-cobalt oxide coatings on *Bekipor ST 20AL3*, the highest value of specific capacitance is $769 \text{ F}\cdot\text{g}^{-1}$, which was demonstrated by the Ni-2Co-O coating annealed at 473 K. This value is almost twice higher than the best SC values of $402\text{--}406 \text{ F}\cdot\text{g}^{-1}$ achieved by nickel-cobalt oxides on AISI304. This significant difference proves that, generally, the stainless steel mesh is a more effective substrate for capacitive applications. Thermal treatment at temperatures higher than 473 K leads to a diminishing effect on the capacitive

behavior as in it was observed in the case of AISI304 stainless steel. Although the coatings on *Bekipor ST 20AL3* showed higher values at 473 K, other results fluctuate considerably if comparing with the coatings on AISI304. The main explanation of this phenomenon is the uneven distribution between the nickel and cobalt oxide layers unable to form a common structure.

3.2.3.2.3 Pseudocapacitive behavior of layered nickel-cobalt oxide coatings on FTO glass

During the electrocatalytic measurements of the coatings deposited on stainless steel and glass substrates, the significant influence of the substrate was observed. In order to eliminate the substrate impact and obtain more accuracy of the parameters, layered nickel-cobalt hydro(oxides) were deposited on FTO glass according to the procedures explained in Chapter 3.2.1.3.

Firstly, galvanostatic charge/discharge measurements were applied to uncoated FTO glass (Fig. 3.44), from which, it became clear that FTO glass does not have significant capacity by itself and therefore is a great substrate for further experiments.

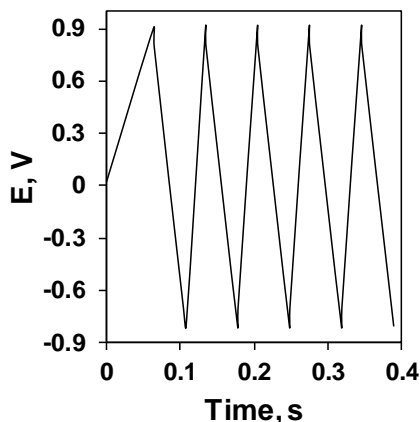


Fig. 3.44. Galvanostatic charge/discharge of FTO glass in 0.1 M NaOH solution at current density $1 \text{ A} \cdot \text{g}^{-1}$

The deposition process on FTO glass is distinguished from the one on stainless steel substrates due to the much slower formation of the film; therefore, a layered coating with thinner nickel and cobalt layers can be achieved. As-deposited nickel-cobalt coatings were synthesized under the same conditions as in Chapter 3.2.1.3. As capacitance measurements with annealed coatings on AISI304 and *Bekipor ST 20AL3* showed that thermal treatment at temperatures higher than 773 K has a detrimental effect on the substrate's mechanical stability and conductivity, only four temperatures for nickel-cobalt oxide coatings annealing were selected: 473, 573, 673 and 773 K.

As layered nickel-cobalt oxide coatings formed on FTO glass are significantly different from the coatings deposited on stainless steels, more detailed results are presented. Starting with Ni-Co-O(H), Fig. 3.45 illustrates the charge/discharge curves of as-deposited Ni-Co-OH (*a*) and annealed at different temperatures Ni-Co-O coatings (*b-d*). When reviewing the results, the difference in shape is observed: in as-

deposited and annealed at 473 K nickel-cobalt coatings curves, a fracture at +0.3 V is seen; it is possibly related to Co(OH)_2 and Ni(OH)_2 oxidation to CoO(OH) and NiO(OH) , respectively. Further treatment removes this effect due to the elimination of hydroxyl ions. Generally, all the curves show a behavior type which is more specific to batteries than capacitors when the charge time is much shorter than the discharge time.

The capacitive parameters of Ni-Co-O coatings are given in Table 3.12. The best specific capacitance is calculated for the annealed Ni-Co-O coating at 573 K, although the coating after a thermal treatment at 473 K is distinguished with higher values of specific energy and specific power. In general, layered coatings on FTO are much better capacitors with great charge storing abilities.

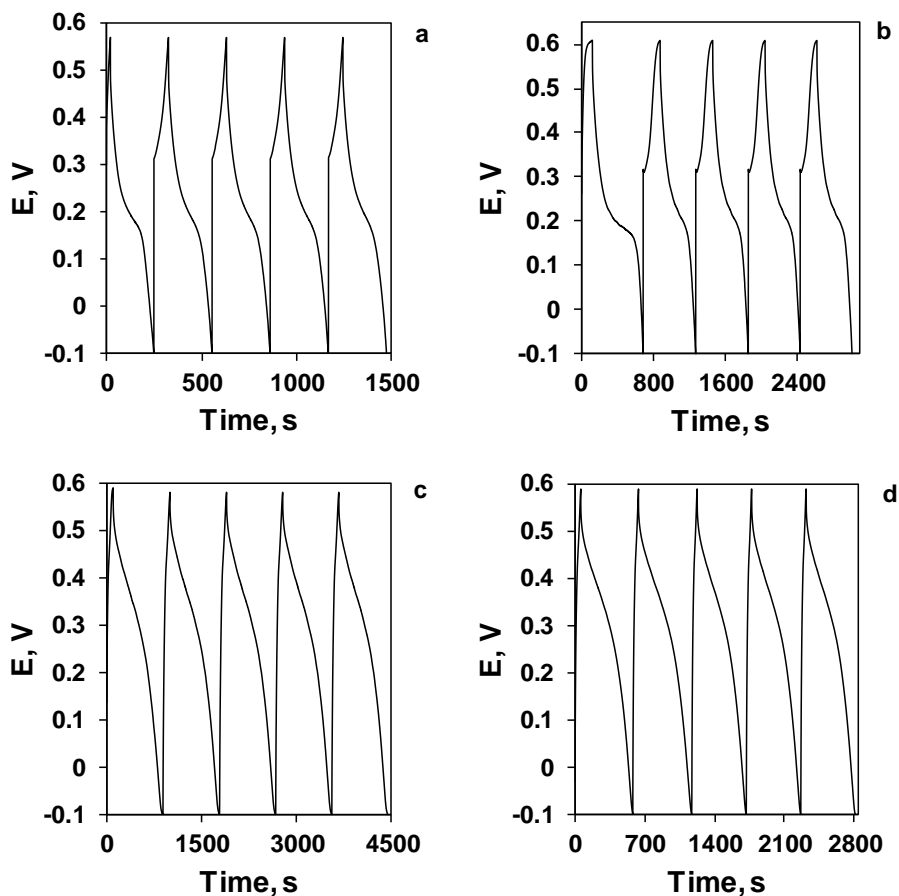


Fig. 3.45. Galvanostatic charge/discharge curves of as-deposited (a) and annealed at different temperatures Ni-Co-O films on FTO glass. Temperatures: *b* – 473 K, *c* – 573 K, *d* – 673 K. Current density $1 \text{ A}\cdot\text{g}^{-1}$

Capacitive measurements were performed with as-deposited and annealed at different temperatures Ni-2Co-O coatings on FTO under the same conditions. The results are presented in Fig. 3.46 and Table 3.12. The charge/discharge curves of

as-deposited Ni-2Co-O (a) are similar to Ni-Co-O by shape, charge/discharge time and the potential window; a visible fracture is observed at +0.3 V which is related to Ni²⁺ and Co²⁺ oxidation to Ni³⁺ and Co³⁺. However, the behavior of coating annealed at 273 K (b) is more characteristic to oxide than oxyhydroxide as it has its potential window shifted to the more positive area and towards relatively symmetric peaks, which shows that the presence of excess cobalt is advantageous. The charge storing mechanism of Ni-2Co-O (c,d), annealed at 573 and 673 K is essentially the same as with Ni-Co-O coatings (Fig. 3.46, c,d). When reviewing the quantitative results of Ni-2Co-O, the benefit in specific capacitance against Ni-Co-O is observed because it reaches as high a value as 1332 F·g⁻¹; however, the specific energy and the specific power values are much lower than those of Ni-Co-O. This means that Ni-2Co-O is able to store more charge, but Ni-Co-O provides a stronger impulse and offers quicker charge accumulation.

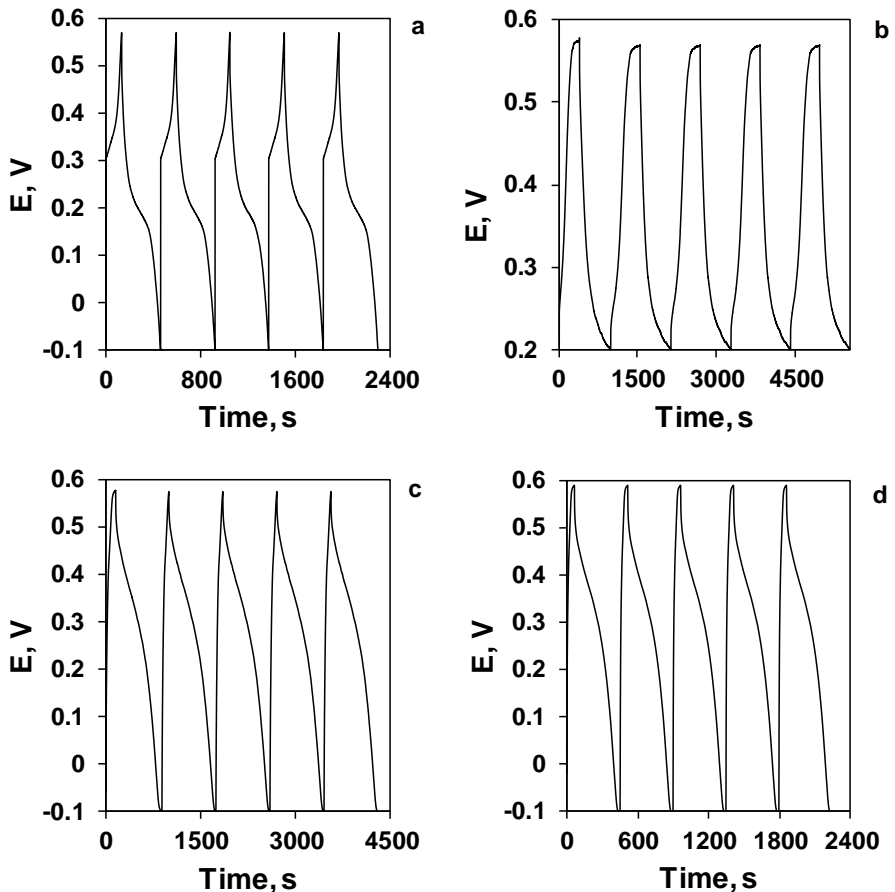


Fig. 3.46. Galvanostatic charge/discharge curves of as-deposited (a) and annealed at different temperatures Ni-2Co-O films on FTO glass. Temperatures: *b* – 473 K, *c* – 573 K, *d* – 673 K. Current density 1 A·g⁻¹

Table 3.12. Capacitance parameters of nickel-cobalt oxide coatings on FTO glass

Coating	Annealing temperature, K	Specific capacitance C_p , $F \cdot g^{-1}$	Specific energy E , $Wh \cdot kg^{-1}$	Specific power P , $W \cdot kg^{-1}$
Ni-Co-O	as-deposited	343	21	335
	473	613	162	690
	573	1142	75.5	345
	673	787	50.5	340
	773	73	14	1017
Ni-2Co-O	as-deposited	488	30	335
	473	1332	25	147
	573	1115	71	337
	673	758	50	493
	773	86	17	1017

Overall, all the layered nickel-cobalt (hydro)oxide coatings on FTO glass appeared to be beneficial comparing with coatings on stainless steel at least regarding a few points. Firstly, FTO glass is a great substrate for the investigation of the capacitive properties of films because it has no capacity itself. The formation mechanism and the slow growth rate of coatings on FTO glass allows achieving a more layered structure without increasing the mass of the substance. Comparing to stainless steel substrates, the capacitive parameters of the coatings deposited on FTO glass are more advantageous.

Although nickel–cobalt oxides on the FTO substrate proved to be a great alternative to oxides of expensive rare metals, some additional research should still be performed. The long cycling life is an important requirement for pseudocapacitive applications. Therefore, long-term stability tests should be carried out by applying 2,000–10,000 cycles of charge/discharge. This is needed in order to eliminate specific capacitive fluctuations due to pulverization and the loss of the electrical contact between the active material and the current as well as wettability issues [283]. After the stability has been checked and proven, the construction of a symmetric or asymmetric hybrid capacitor may begin. The latest research revealed that hybrid devices involving hybridization of a faradaically rechargeable pseudocapacitor or a battery-type electrode with a non-faradaically rechargeable electric double-layer capacitor electrode system (e.g., carbon-based materials) are more advantageous over the common systems [284]. In these systems, energy can be stored through both mechanisms. The total charge stored in the hybrid electrode is due to both components widening the working potential window as well.

To sum up, the electrocatalytic performance of cobalt and nickel–cobalt oxide coatings formed during this work, some noteworthy remarks can be highlighted. The significant activity in OER demonstrated by cobalt oxide coatings on *Bekipor ST 20AL3* suggests further development of the electrocatalytic system involving this electrode. However, a few additional experiments should complete the characterization, such as long-term stability tests when applying a high current

density, and quantitative measurements of the generated O₂. When reviewing the overall results of the activity of nickel–cobalt oxides in oxygen evolution, the advantage of coatings deposited on AISI304 over other substrates is evident. The obtained results (Fig. 3.29) confirmed the formation of a spinel structure NiCo₂O₄ directly on the substrate as well as the significant system performance. Although spinel structures are distinguished with excellent stability, alkaline oxygen evolution creates harsh conditions which might lead to the film's destruction. Therefore, long-term stability tests under such conditions are vital before composing a commercial electrolyzer. Furthermore, online gas chromatography could be introduced in the system's characterization techniques for the quantitative measurements of the generated O₂.

Conclusions

1. Cobalt (hydro)oxide coatings on *Bekipor ST 20AL3* stainless steel mesh were formed by galvanostatic electrodeposition while using three different cobalt(II) precursors (nitrate, chloride and acetate). The structural analysis revealed that the as-deposited coatings are mainly composed of lamellar α -Co(OH)₂ layers with intercalated impurities depending on the electrolyte in use. It was discovered that the most uniform coating formation in 3D structure is achieved when the deposition time is approximately 240 s, and the current density is 0.5 mA·cm⁻².
2. The highest electrolytic activity in water anodic oxidation and specific capacitance were obtained for cobalt (hydro)oxide coatings electrodeposited when using a cobalt(II) nitrate bath. The formation of the spinel-type Co₃O₄ after the annealing at 673 K leads to superior electrocatalytic performance but it has a detrimental effect on the pseudocapacitive properties.
3. Layered nickel-cobalt oxide coatings were potentiostatically electrodeposited on AISI304 plates, *Bekipor ST 20AL3* mesh and FTO glass. Structural analysis revealed that as-deposited coatings consist predominantly of α -Co(OH)₂ and α -Ni(OH)₂ phases which form a spinel-type NiCo₂O₄ structure after annealing at 473–673 K. Under similar electrodeposition conditions, the growth rate of nickel-cobalt hydroxide depends on the substrate in use, and it decreases in the following order: AISI304 > *Bekipor ST 20AL3* > FTO.
4. It was established that the presence of a spinel-type NiCo₂O₄ phase results in the high activity of coatings in the oxygen evolution reaction: the anodic current density of 10 mA·cm⁻² in 0.1 M NaOH is achieved at 0.45 V overpotential. The electrocatalytic activity of nickel-cobalt oxides is higher than the one of separate Co₃O₄ and NiO phases. The overall electrocatalytic efficiency depends on the substrate and the annealing temperature: the highest values of the anodic current were obtained for coatings annealed at 573–673 K on AISI304 stainless steel plates.
5. The galvanostatic charge-discharge measurements revealed that the best pseudocapacitive performance is characteristic of nickel-cobalt oxide coatings on FTO glass: the maximum specific capacitance of 1332 F·g⁻¹ was obtained for coatings annealed at 473 K.

Acknowledgments

Writing this dissertation was one of the most challenging tasks in my professional life. This work would never have been completed without the support and encouragement of my beloved husband Irmantas Barauskas and son Faustas Barauskas.

I would like to express my sincere gratitude to my supervisor, prof. Eugenijus Valatka, for his wisdom, endless optimism, and belief in my strength and abilities.

I also thank to my colleagues for their contribution: Tadas Dambrauskas for XRD spectra, Žaneta Rukuižienė for SEM and EDS analysis, Andrius Gineika for TG–DSC analysis, Andrius Jaskūnas for AAS analysis and Aušra Tamulevičienė for RAMAN spectra.

Finally, I would like to thank my parents, Artūras Kelpša and Halina Kelpšienė, my sister, Agnė Kelpšaitė-Budinavičienė, and my grandmother, Felicija Tumienė, for their support.

REFERENCES

1. **Donaldson, J.D., Beyersmann, D.** *Cobalt and Cobalt Compounds*. Weinheim: Wiley and Sons VCH Verlag GmbH & Co. KGaA, 2005.
2. **Garcia, T., Dejoz, A.M., Puertolas, B., Solsona, B.E.** *Cobalt Oxide, Co_3O_4 , as a Catalyst for Environmental Applications*. USA: Nova Science Publishers, 2011.
3. **Brownson, J.R.S., Levy-Clement, C.** Electrodeposition of alpha- and beta-Cobalt Hydroxide Thin Films via Dilute Nitrate Solution Reduction. In: *Physica Status Solidi B*, 2008, **245**(9), 1785–1791.
4. **Ismail, J., Ahmed, M.F., Kamath, P.V., Subbanna, G.N., Uma, S., Gopalakrishnan, J.** Organic Additive-Mediated Synthesis of Novel Cobalt(II) Hydroxides. In: *Journal of Solid State Chemistry*, 1995, **114**(2), 550–555.
5. **Liu, Z., Ma, R., Osada, M., Takada, K., Sasaki, T.** Selective and Controlled Synthesis of Alpha and Beta Cobalt Hydroxides in Highly Developed Hexagonal Platelets. In: *Journal of American Chemical Society*, 2005, **127**(40), 13869–13874.
6. **Jayashree, R.S., Kamath, P.V.** Electrochemical Synthesis of α -Cobalt Hydroxide. In: *Journal of Materials Chemistry*, 1999, **9**(4), 961–963.
7. **Xu, Z.P., Zeng, H.C.** Thermal Evolution of Cobalt Hydroxides: A Comparative Study of Their Various Structural Phases. In: *Journal of Materials Chemistry*, 1998, **8**(11), 2499–2506.
8. **Evans, D.G., Slade, R.C.T.** *Double Layered Hydroxides*. Heidelberg: Springer-Verlag, 2006.
9. **Hu, Z.G., Mo, L.P., Feng, X.J., Shi, J., Wang, Y.X., Me, Y.L.** Synthesis and Electrochemical Capacitance of Sheet-Like Cobalt Hydroxide. In: *Materials Chemistry and Physics*, 2009, **114**(1), 53–57.
10. **Masikhwa, T.M., Madito, M.J., Momodu, D., Bello, A., Dangbegnon, J.K., Manyala, N.** High Electrochemical Performance of Hybrid Cobalt Oxyhydroxide/Nickel Foam Graphene. In: *Journal of Colloid and Interface Science*, 2016, **484**, 77–85.
11. **Forticaux, A., Dang, L.N., Liang, H.F., Jin, S.** Controlled Synthesis of Layered Double Hydroxide Nanoplates Driven by Screw Dislocations. In: *Nano Letters*, 2015, **15**(5), 3403–3409.
12. **Hu, S., Melton, C., Mukherjee, D.** A Facile Route for the Synthesis of Nanostructured Oxides and Hydroxides of Cobalt Using Laser Ablation Synthesis in Solution (LASIS). In: *Physical Chemistry Chemical Physics*, 2014, **16**(43), 24034–24044.
13. **Scavetta, E., Ballarin, B., Gazzano, M., Tonelli, D.** Electrochemical Behaviour of Thin Films of Co/Al Layered Double Hydroxide Prepared by Electrodeposition. In: *Electrochimica Acta*, 2009, **54**(3), 1027–1033.
14. **Zheng, H., Tang, F., Lim, M., Rufford, T., Mukerji, A., Wang, L., Gaoqing, L.** Electrochemical Behaviour of Carbon-Nanotube/Cobalt Oxyhydroxide Nanoflake Multilayer Films. In: *Journal of Power Sources*, 2009, **193**(2), 930–934.
15. **Garrido Pedrosa, A.M., Souza, M.J.B., Melo, D.M.A., Araujo, A.S., Zinner, L.B., Fernandes, J.D.G., Martinelli, A.E.** Systems Involving Cobalt and Cerium

Oxides: Characterization and Catalytic Behavior in the C₆-C₇ n-Alkanes Combustion. In: *Solid State Sciences*, 2003, **5**(5), 725–728.

16. **Moro-Oka, Y., Morikawa, Y., Ozaki, A.** Regularity in the Catalytic Properties of Metal Oxides in Hydrocarbon Oxidation. In: *Journal of Catalysis*, 1967, **7**(1), 23–32.

17. **Sokolovskii, V.D.** Principles of Oxidative Catalysis on Solid Oxides. In: *Catalysis Reviews – Science and Engineering*, 1990, **32**(1–2), 1–49.

18. **Bond, G.C.** *Heterogeneous Catalysis: Principles and Applications*. Oxford: Oxford University Press, 1987.

19. **McCormick, P.G., Tsuzuki, T., Robinson, J.S., Ding, J.** Nanopowders Synthesized by Mechanochemical Processing. In: *Advanced Materials*, 2001, **13**(12–13), 1008–1010.

20. **Zhang, R., Villanueva, A., Alamdari, H., Kaliaguine, S.** Catalytic Reduction of NO by Propene over LaCo_{1-x}Cu_xO₃ Perovskites Synthesized by Reactive Grinding. In: *Applied Catalysis B: Environmental*, 2006, **64**(3–4), 220–233.

21. **Yang, H., Hu, Y., Zhang, X., Qiu, G.** Mechanochemical Synthesis of Cobalt Oxide Nanoparticles. In: *Materials Letters*, 2004, **58**(3–4), 387–389.

22. **Hu, L., Peng, Q., Li, Y.** Selective Synthesis of Co₃O₄ Nanocrystal with Different Shape and Crystal Plane Effect on Catalytic Property for Methane Combustion. In: *Journal of American Chemical Society*, 2008, **130**(48), 16136–16137.

23. **Llorca, J., De La Piscina, P.R., Dalmon, J.A., Homs, N.** Transformation of Co₃O₄ during Ethanol Steam Reforming. Activation Process for Hydrogen Production. In: *Chemistry of Materials*, 2004, **16**(18), 3573–3578.

24. **Amri, A., Jiang, Z.T., Yin, C.Y., Fadli, A., Rahman, M.M., Bahri, S., Widjaja, H., Mondinos, N., Herawan, T., Munir, M.M., Priyotomo, G.** Structural, Optical and Mechanical Properties of Cobalt Copper Oxide Synthesized from Low Concentrations of Sol-Gel Process. In: *Physica Status Solidi A – Applications and Materials Science*, 2016, **213**(12), 3205–3213.

25. **Schoeberl, C., Manolova, M., Freudenberger, R.** Sol-Gel-Deposited Cobalt and Nickel Oxide as an Oxygen Evolution Catalyst in Alkaline Media. 2014, **40** (35), 11773–11778.

26. **El-Hout, S.I., Chen, C.L., Liang, T., Yang, L.F., Zhang, J.** Cetyltrimethylammonium Bromide Assisted Hydrothermal Synthesis of Cobalt Oxide Nanowires Anchored on Graphene as an Efficient Electrode Material for Supercapacitor Applications. In: *Materials Chemistry and Physics*, 2017, **198**, 99–106.

27. **Alayoglu, S., Rosenberg, D.J., Ahmed, M.** Hydrothermal Synthesis and Characterization under Dynamic Conditions of Cobalt Oxide Nanoparticles Supported over Magnesium Oxide Nano-Plates. In: *Dalton Transactions*, 2016, **45**(24), 9932–9941.

28. **Noorbakhsh, A., Mirkalaei, M.M., Yousefi, M.H., Manochehri, S.** Electrodeposition of Cobalt Oxide Nanostructure on the Glassy Carbon Electrode for Electrocatalytic Determination of Para-Nitrophenol. *Electroanalysis*, 2014, **26**(12), 2716–2726.

29. **Li, S.J., Du, J.M., Chen, J., Mao, N.N., Zhang, M.J., Pang, H.** Electrodeposition of Cobalt Oxide Nanoparticles on Reduced Graphene Oxide: A Two-Dimensional Hybrid for Enzyme-Free Glucose Sensing. In: *Journal of Solid State Electrochemistry*, 2014, **18**(4), 1049–1056.
30. **Kelpsaite, I., Baltrusaitis, J., Valatka, E.** Electrochemical Deposition of Porous Cobalt Oxide Films on AISI 304 Type Steel. In: *Materials Science-Medziagotyra*, 2011, **17**(3), 236–243.
31. **Barauskiene, I., Valatka, E.** Synthesis, Structure and Capacitive Properties of Cobalt Hydroxide Films on Stainless Steel Substrates. (2014). In: *Central European Journal of Chemistry*, 2014, **12**(11), 1206–1211.
32. **Rajamathi, M., Kamath, P.V., Seshadri, R.** Chemical Synthesis of α -Cobalt Hydroxide. In: *Materials Research Bulletin*, 2000, **35**(2), 271–278.
33. **Zhu, Y., Li, H., Gedanken, A.** Preparation of Nanosized Cobalt Hydroxides and Oxyhydroxides Assisted by Sonication. In: *Journal of Materials Chemistry*, 2002, **12**, 729–733.
34. **Oku, M., Sato, Y.** *In-Situ* X-ray Photoelectron Spectroscopic Study of the Reversible Phase Transition between CoO and Co₃O₄ in Oxygen of 10⁻³ Pa. In: *Applied Surface Science*, 1992, **55**(1), 37–41.
35. **Patil, D., Patil, P., Subramanian, V., Joy, P.A., Potdar, H.S.** Highly Sensitive and Fast Responding CO Sensor Based on Co₃O₄ Nanorods. In: *Talanta*, 2010, **81**(1–2), 37–43.
36. **Nefedov, V.I., Firsov, M.N., Shaplygin, I.S.** Electronic Structures of MRhO₂, MRh₂O₄, RhMO₄ and Rh₂MO₆ on the Basis of X-Ray Spectroscopy and ESCA Data. In: *Journal of Electron Spectroscopy and Related Phenomena*, 1982, **26**(1), 65–78.
37. **Yang, J., Liu, H., Martens, W.N., Frost, R.L.** Synthesis and Characterization of Cobalt Hydroxide, Cobalt Oxyhydroxide, and Cobalt Oxide Nanodiscs. In: *Journal of Physical Chemistry C*, 2010, **114**, 111–119.
38. **Vaz, C.A.F., Wang, H.Q., Ahn, C.H., Henrich, V.E., Baykara, M.Z., Schwendemann, T.C., Pilet, N., Albers, B.J., Schwarz, U.D., Zhang, L.H., Zhu, Y., Wang, J., Altman, E.I.** Interface and Electronic Characterization of Thin Epitaxial Co₃O₄ Films. In: *Surface Science*, 2009, **603**(2), 291–297.
39. **Christoskova, S.G., Stoyanova, M., Georgieva, M., Mehandjiev, D.** Preparation and Characterization of a Higher Cobalt Oxide. In: *Materials Chemistry and Physics*, 1999, **60**(1), 39–43.
40. **Kerfoot, D.G.E.** *Nickel*. Weinheim: Wiley and Sons VCH Verlag GmbH & Co. KGaA, 2005.
41. **Guillet, N., Millet, P.** *Alkaline Water Electrolysis*. Weinheim, Germany: Wiley-VCH Verlag GmbH & Co. KGaA, 2015.
42. **Hall, D.S., Lockwood, D.J., Bock, C., MacDougall, B.R.** Nickel Hydroxides and Related Materials: A Review of Their Structures, Synthesis and Properties. In: *Proceedings of the Royal Society A*, 2014, **471**, Article No. 20140792.
43. **McEwen, R.S.** Crystallographic Studies on Nickel Hydroxide and the Higher Nickel Oxides. In: *Journal of Physical Chemistry*, 1971, **75**(12), 1782–1789.

44. **Bode, H., Dehmelt, K., Witte, J.** Zur kenntnis der nickelhydroxidelektrode - I. Uber das nickel (III)-hydroxidhydrat. In: *Electrochimica Acta*, 1966, **11**(8), 1079–1087.
45. **Tang, J.J., Liu, Y., Tian, L., Zhang, L.L., Wang, D.X., Zhang, T.A.** Influence of Crystal Growth Direction Selectivity on Morphology and Electrochemical Activity of Spherical Nickel Hydroxide. In: *Chinese Journal of Inorganic Chemistry*, 2017, **32**(2), 354–360.
46. **Wang, Y.B., Shang, B., Lin, F., Chen, Y., Ma, R.G., Peng, B., Deng, Z.W.** Controllable Synthesis of Hierarchical Nickel Hydroxide Nanotubes for High Performance Supercapacitors. In: *Chemical Communications*, 2018, **54**(5), 559–562.
47. **Kong, X.K., Zhang, C.L., Hwang, S.Y., Chen, Q.W., Peng, Z.M.** Free-Standing Holey Ni(OH)₂ Nanosheets with Enhanced Activity for Water Oxidation. In: *Small*, 2017, **13**(26), UNSP 1700334.
48. **Patel, R., Park, J.T., Patel, M., Dash, J.K., Gowd, E.B., Karpoomath, R., Mishra, A., Kwak, J., Kim, J.H.** Transition-Metal-Based Layered Double Hydroxides Tailored for Energy Conversion and Storage. In: *Journal of Materials Chemistry A*, 2018, **6**(1), 12–29.
49. **Wang, D.W., Guan, B., Li, Y., Li, D.D., Xu, Z.Y., Hu, Y.F., Wang, Y.Q., Zhang, H.H.** Morphology-Controlled Synthesis of Hierarchical Mesoporous alpha-Ni(OH)₂ Microspheres for High-Performance Asymmetric Supercapacitors. In: *Journal of Alloys and Compounds*, 2018, **737**, 238–247.
50. **Li, J., Wei, M., Chu, W., Wang, N.** High-Stable Alpha-Phase NiCo Double Hydroxide Microspheres via Microwave Synthesis for Supercapacitor Electrode Materials. In: *Chemical Engineering Journal*, 2017, **316**, 277–287.
51. **Osinska, M., Stefanowicz, T., Paukszta, D.** Nickel Hydroxide Ageing Time Influence on its Solubility in Water Acidified with Sulphuric Acid. In: *Journal of Hazardous Materials*, 2004, **112**(3), 177–182.
52. **Yuan, S.X., Lu, C.X., Li, Y., Wang, X.M.** Two-Step Deposition/Reduction Synthesis of Porous Lamellar beta-Ni(OH)₂/Reduced Graphene Oxide Composites with Large Capacitance for Supercapacitors. In: *Chemelectrochem*, 2017, **4**(11), 2826–2834.
53. **Mansournia, M., Moradinia, E.** beta-Ni(OH)₂ and NiO Nanostructures: Novel Template-Free Synthesis and Their Photocatalytic Activity. In: *Journal of Materials Science – Materials in Electronics*, 2016, **27**(1), 82–89.
54. **Din, M.I., Rami, A.** Recent Advances in the Synthesis and Stabilization of Nickel and Nickel Oxide Nanoparticles: A Green Adeptness. In: *International Journal of Analytical Chemistry*, 2016, Article No. 3512145.
55. **Jia, F., Zhang, L., Shang, X., Yang, Y.** Non-Aqueous Sol-Gel Approach towards the Controllable Synthesis of Nickel Nanospheres, Nanowires and Nanoflowers. In: *Advanced Materials*, 2008, **20**(5), 1050–1054.
56. **Tong, W., Huang, Y.D., Cai, Y.J., Guo, Y., Wang, X.C., Jia, D.Z., Sun, Z.P., Pang, W.K., Guo, Z.P., Zong, J.** Synthesis of Hierarchical Mesoporous Lithium Nickel Cobalt Manganese Oxide Spheres with High Rate Capability for Lithium-Ion Batteries. In: *Applied Surface Science*, 2018, **428**, 1036–1045.

57. **Chen, D.H., Wu, S.H.** Synthesis of Nickel Nanoparticles in Water-In-Oil Microemulsions. In: *Chemistry of Materials*, 2000, **12**(5), 1354–1360.
58. **Chen, G., Guan, H.T., Dong, C.J., Wang, Y.D.** Synthesis of Core-Shell Carbon Sphere@Nickel Oxide Composites and Their Application for Supercapacitors. In: *Ionics*, 2018, **24**(2), 513–521.
59. **Yang, G.W.** Laser Ablation in Liquids: Applications in the Synthesis of Nanocrystals. In: *Progress in Materials Science*, 2007, **52**(4), 648–698.
60. **Nelson, P.A., Elliott, J.M., Attard, G.S., Owen, J.R.** Mesoporous Nickel/Nickel Oxide a Nanoarchitected Electrode. In: *Chemistry of Materials*, 2002, **14**(2), 524–529.
61. **Zhou, W.J., Zhao, D.D., Xu, M.W., Xu, C.L., Li, H.L.** Effects of the Electrodeposition Potential and Temperature on the Electrochemical Capacitance Behavior of Ordered Mesoporous Cobalt Hydroxide Films. In: *Electrochimica Acta*, 2008, **53**, 7210–7219.
62. **Therese, G.H.A., Kamath, P.V.** Electrochemical Synthesis of Metal Oxides and Hydroxides. In: *Chemistry of Materials*, 2000, **12**(5), 1195–1204.
63. **Shahrokhian, S., Rahimi, S., Mohammadi, R.** Nickel-Cobalt Layered Double Hydroxide Ultrathin Nanosheets Coated on Reduced Graphene Oxide Nanosheets/Nickel Foam for High Performance Asymmetric Supercapacitors. In: *International Journal of Hydrogen Energy*, 2018, **43**(4), 2256–2267.
64. **Coviello, D., Contursi, M., Toniolo, R., Casella, I.G.** Electrochemical and Spectroscopic Investigation of a Binary Ni-Co Oxide Active Material Deposited on Graphene/Polyvinyl Alcohol Composite Substrate. In: *Journal of Electroanalytical Chemistry*, 2017, **791**, 117–123.
65. **Adan-Mas, A., Duarte, R.G., Silva, T.M., Guerlou-Demourgues, L., Montemor, M.F.G.** Enhancement of the Ni-Co Hydroxide Response as Energy Storage Material by Electrochemically Reduced Graphene Oxide. In: *Electrochimica Acta*, 2017, **240**, 323–340.
66. **Jiang, L., Sui, Y., Qi, J., Chang, Y., He, Y., Meng, Q., Wei, F., Sun, Z., Jin, Y.** Hierarchical Ni-Co Layered Double Hydroxide Nanosheets on Functionalized 3D-RGO Films for High Energy Density Asymmetric Supercapacitor. In: *Applied Surface Science*, 2017, **426**, 148–159.
67. **Balram, A., Zhang, H., Santhanagopalan, S.** Enhanced Oxygen Evolution Reaction Electrocatalysis via Electrodeposited Amorphous α -Phase Nickel-Cobalt Hydroxide Nanodendrite Forests. In: *ACS Applied Materials & Interfaces*, 2017, **9**(34), 28355–28365.
68. **Nguyen, T., Boudard, M., Carmezim, J.M., Montemor, M.F.** Layered Ni(OH)₂-Co(OH)₂ Films Prepared by Electrodeposition as Charge Storage Electrodes for Hybrid Supercapacitors. In: *Scientific Reports*, 2017, **7**, 39980.
69. **Sun, S., Xu, Z.J.** Composition Dependence of Methanol Oxidation Activity in Nickel-Cobalt Hydroxides and Oxides: An Optimization Toward Highly Active Electrodes. In: *Electrochimica Acta*, 2015, **165**, 56–66.
70. **Wang, Y., Cheng, K., Cao, D., Yang, F., Yan, P., Zhang, W., Wang, G.** Preparation of NiCo₂O₄ Nanosheet Arrays and Its High Catalytic Performance for H₂O₂ Electroreduction. In: *Fuel Cells*, 2015, **15**(2), 298–305.

71. **Nguyen, V.H., Shim, J.J.** Three-Dimensional Nickel Foam/Graphene/NiCo₂O₄ as High-Performance Electrodes for Supercapacitors. In: *Journal of Power Sources*, 2015, **273**, 110–117.
72. **Banu, A., Marcu, M., Alexandrescu, E., Anghel, E.M.** Electrochemical Deposition And Characterization of Polypyrrole Coatings Doped with Nickel Cobalt Oxide for Environmental Applications. In: *Journal of Solid State Electrochemistry*, 2014, **18**(10), 2661–2671.
73. **Zeng, Z., Xiao, B., Zhu, X., Zhu, J., Xiao, D., Zhu, J.** Flower-like Binary Cobalt-Nickel Oxide with High Performance for Supercapacitor Electrode via Cathodic Electrodeposition. In: *Ceramics International*, 2017, **43**, S633–S638.
74. **Kothari, R., Buddhi, D., Sawhney, R.L.** Comparison of Environmental and Economic Aspects of Various Hydrogen Production Methods. In: *Renewable and Sustainable Energy Reviews*, 2008, **12**(2), 553–563.
75. **Nath, K., Das, D.** Production and Storage of Hydrogen: Present Scenario and Future Perspective. In: *Journal of Scientific & Industrial Research*, 2007, **66**, 701–709.
76. **Vincent, I., Bessarabov, D.** Low Cost Hydrogen Production by Anion Exchange Membrane Electrolysis: A Review. In: *Renewable and Sustainable Energy Reviews*, 2018, **81**(2), 1690–1704.
77. **Holladay, J.D., Hu, J., King, D.L., Wang, Y.** An Overview of Hydrogen Production Technologies. In: *Catalysis Today*, 2009, **139**(4), 244–260.
78. **Turner, J., Sverdrup, G., Mann, M.K., Maness, P.C., Kroposki, B., Ghirardi, M., Evans, R.J., Blake, D.** Renewable Hydrogen Production. In: *International Journal of Energy Research*, 2008, **32**(5), 379–407.
79. **Dominkovic, D.F., Bacekovic, I., Pedersen, A.S., Krajacic, G.** The Future of Transportation in Sustainable Energy Systems: Opportunities and Barriers in a Clean Energy Transition. *Renewable and Sustainable Energy Reviews*, 2018, **82**(2), 1823–1838.
80. **Abbasi, T., Abbasi, S.A.** ‘Renewable’ Hydrogen: Prospects and Challenges. In: *Renewable and Sustainable Energy Reviews*, 2011, **15**(6), 3034–3040.
81. **Trotochaud, L., Boettcher, S.W.** Precise Oxygen Evolution Catalysts: Status and Opportunities. In: *Scripta Materialia*, 2014, **74**, p. 25–32.
82. **Cheng, Y., Jiang, S.P.** Advances in Electrocatalysts for Oxygen Evolution Reaction of Water Electrolysis – From Metal Oxides to Carbon Nanotubes. In: *Progress in Natural Science: Materials International*, 2015, **25**, 545–553.
83. **Burke, M.S., Enman, L.J., Batchellor, A.S., Zou, S., Boettcher, S.W.** Oxygen Evolution Reaction Electrocatalysis on Transition Metal Oxides and (Oxy)Hydroxides: Activity Trends and Design Principles. In: *Chemistry of Materials*, 2015, **27**, 7549–7558.
84. **Trasatti, S.** Work Function, Electronegativity and Electrochemical Behaviour of Metals: III. Electrolytic Hydrogen Evolution in Acid Solutions. In: *Journal of Electroanalytical Chemistry and Interfacial Electrochemistry*, 1972, **39**(1), 163–184.
85. **Kelly, T.G., Lee, K.X., Chen, J.G.** Pt-Modified Molybdenum Carbide for the Hydrogen Evolution Reaction: From Model Surfaces to Powder Electrocatalysts. In: *Journal of Power Sources*, 2014, **271**, 76–81.

86. **Jaramillo, T.F., Jorgensen, K.P., Bonde, J., Nielsen, J.H., Horch, S., Chorkendorff, J.** Identification of Active Edge Sites for Electrochemical H₂ Evolution from MoS₂ Nanocatalysts. In: *Science*, 2007, **317**(5834), 100–102.
87. **Kibsgaard, J., Chen, Z., Reinecke, B.N., Jaramillo, T.F.** Engineering the Surface Structure of MoS₂ to Preferentially Expose Active Edge Sites for Electrocatalysis. In: *Nature Materials*, 2012, **11**, 963–969.
88. **Voiry, D., Yamaguchi, H., Li, J., Silva, R., Alves, D.C.B., Fujita, T., Chen, M., Asefa, T., Shenoy, V.B., Eda, G., Chhowalla, M.** Enhanced Catalytic Activity in Strained Chemically Exfoliated WS₂ Nanosheets for Hydrogen Evolution. In: *Nature Materials*, 2013, **12**(9), 850–855.
89. **Popczun, E.J., McKone, J.R., Read, C.G., Biacchi, A.J., Wiltrout, A.M., Lewis, N.S., Schaak, R.** Nanostructured Nickel Phosphide as an Electrocatalyst for the Hydrogen Evolution Reaction. In: *Journal of the American Chemical Society*, 2013, **135**(25), 9267–9270.
90. **Mardosaite, R., Valatka, E.** Structure and Electrocatalytic Properties of Amorphous Cobalt-Sulphide Films on FTO Substrate. In: *Chalcogenide Letters*, 2017, **14**(5), 171–179.
91. **Tian, J., Liu, Q., Asiri, A.M., Sun, X.** Self-Supported Nanoporous Cobalt Phosphide Nanowire Arrays: An Efficient 3D Hydrogen-Evolving Cathode over the Wide Range of pH 0–14. In: *Journal of the American Chemical Society*, 2014, **136**(21), 7587–7590.
92. **Zheng, Y., Jiao, Y., Zhu, Y., Li, L.H., Han, Y., Chen, Y., Du, A., Jaroniec, M., Qiao, S.Z.** Hydrogen Evolution by a Metal-Free Electrocatalyst. In: *Nature Communications*, 2014, **5**, Article No. 3783.
93. **Doyle, R.L., Lyons, M.E.G.** An Electrochemical Impedance Study of the Oxygen Evolution Reaction at Hydrated Iron Oxide in Base. In: *Physical Chemistry Chemical Physics*, 2013, **15**(14), 5224–5237.
94. **Doyle, R.L., Godwin, I.J., Brandon, M.P., Lyons, M.E.G.** Redox and Electrochemical Water Splitting Catalytic Properties of Hydrated Metal Oxide Modified Electrodes. In: *Physical Chemistry Chemical Physics*, 2013, **15**(33), 13737–13783.
95. **Trasatti, S.** Advances in Materials for Electrocatalysis. In: *Portugaliae Electrochimica Acta*, 2001, **19**, 197–208.
96. **Roginskaya, Y.E., Morozova, O.V., Lubnin, E.N., Ulitina, Y.E., Lopukhova, G.V., Trasatti, S.** Characterization of Bulk and Surface Composition of Co_xNi_{1-x}O_y Mixed Oxides for Electrocatalysis. In: *Langmuir*, 1997, **13**(17), 4621–4627.
97. **Lodi, G., Sivieri, E., De Battisti, A., Trasatti, S.** Ruthenium Dioxide-Based Film Electrodes. In: *Journal of Applied Electrochemistry*, 1978, **8**(2), 135–143.
98. **Carugati, A., Lodi, G., Trasatti, S.** Fractional Reaction Orders in Oxygen Evolution from Acidic Solutions at Ruthenium Oxide Anodes. In: *Materials Chemistry*, 1981, **6**(4–5), 255–266.
99. **Villullas, H.M., Mattos-Costa, F.I., Bulhoes, L.O.S.** Oxygen Evolution on Platinum Modified Ti/RuO₂ Sol-Gel Films. In: *Journal of Electroanalytical Chemistry*, 2003, **545**, 89–97.

100. **Burke, L.D., Lyons, M.E.G.** *Electrochemistry of Hydrous Oxide Films*. Boston, USA: Springer, 1986.
101. **Burke, L.D., O'Sullivan, E.J.M.** Oxygen Gas Evolution on Hydrous Oxides – An Example of Three-Dimensional Electrocatalysis? In: *Journal of Electroanalytical Chemistry*, 1981, **117**(1), 155–160.
102. **Burke, L.D., Casey, M.I., Cunnane, V.J., Murphy, O.J., Twomey, T.A.M.** Evidence for the Formation of a Cationic Surface Layer on Silver, Copper and Gold Under Potential Cycling Conditions: A Possible Interpretation of the Electromagnetic Field Effect Involved in Sers Phenomena. In: *Journal of Electroanalytical Chemistry*, 1985, **189**(2), 353–362.
103. **Dau, H., Limberg, C., Reier, T., Risch, M., Roggan, S., Strasser, P.** The Mechanism of Water Oxidation: from Electrolysis via Homogeneous to Biological Catalysis. In: *ChemCatChem*, 2010, **2**(7), 724–761.
104. **Ozkan Zayim, E., Turhan, I., Tepehan, F.Z., Ozer, N.** Sol-Gel Deposited Nickel Oxide Films for Electrochromic Applications. In: *Solar Energy Materials and Solar Cells*, 2008, **92**(2), 164–169.
105. **Subramanian, V., Zhu, H.W., Vajtai, R., Ajayan, P.M., Wei, B.Q.** Hydrothermal Synthesis and Pseudocapacitance Properties of MnO₂ Nanostructures. In: *Journal of Physical Chemistry B*, 2005, **109**(43), 20207–20214.
106. **Toupin, M., Brousse, T., Belanger, D.** The Influence of Microstructure on the Charge Storage Properties of Chemically Synthesized Manganese Dioxide. In: *Chemistry of Materials*, 2002, **14**(9), 3946–3952.
107. **Porqueras, I., Bertran, E.** Electrochromic Behaviour of Nickel Oxide Thin Films Deposited by Thermal Evaporation. In: *Thin Solid Films*, 2001, **398/399**, 41–44.
108. **Taguchi, A., Inoue, S., Akamaru, S., Hara, M., Watanabe, K., Abe, T.** Phase Transition and Electrochemical Capacitance of Mechanically Treated Managanese Oxides. In: *Journal of Alloys and Compounds*, 2006, **414**(1–2), p. 137-141.
109. **Lee, H.Y., Goodenough, J.B.** Supercapacitor Behavior with KCl Electrolyte. In: *Journal of Solid State Chemistry*, 1999, **144**(1), 220–223.
110. **Dai, Y., Wang, K., Zhao, J., Xie, J.** Manganese Oxide Film Electrodes Prepared by Electrostatic Spray Deposition for Electrochemical Capacitors from the KMnO₄ Solution. In: *Journal of Power Sources*, 2006, **161**(1), 737–742.
111. **Wu, Y. G., Wu, G.M., Ni, X.Y., Wu, X.** Ion Transport in Electrochromic Nickel Oxide Thin Films. In: *Solar Energy Materials and Solar Cells*, 2000, **63**(2), 217–226.
112. **Subramanian, B., Mohamed Ibrahim, M., Senthikumar, V., Murali, K.R., Vidhya, V.S., Sanjeerviraja, C., Jayachandran, M.** Optoelectronic and Electrochemical Properties of Nickel Oxide (NiO) Films Deposited by DC Reactive Magnetron Sputtering. In: *Physica B: Condensed Matter*, 2008, **403**(21–22), 4104–4110.
113. **Djufors, B., Broughton, J.N., Brett, M.J., Ivey, D.G.** Production of Capacitive Films from Mn Thin Films: Effects of Current Density and Film Thickness. In: *Journal of Power Sources*, 2006, **156**(2), 741–747.
114. **Kong, D., Wang, J., Shao, H., Zhang, J., Cao, C.** Electrochemical Fabrication of a Porous Nanostructured Nickel Hydroxide Film Electrode with Superior

Pseudocapacitive Performance. In: *Journal of Alloys and Compounds*, 2011, **509**(18), 5611–5616.

115. **Barauskiene, I., Valatka, E.** Electrocatalytic and Pseudocapacitive Properties of Cobalt (hydro)oxide Films on Sintered Metal Fiber Filter. In: *Materials for Renewable and Sustainable Energy*, 2018, **7**(1), 1–10.

116. **Xiao, F., Xu, Y.** Pulse Electrodeposition of Manganese Oxide for High-Rate Capability Supercapacitors. In: *International Journal of Electrochemical Science*, 2012, **7**(8), 7440–7450.

117. **Lyons, M.E.G., Cakara, A., O'Brien, P., Godwin, I., Doyle, R. L.** Redox, pH Sensing and Electrocatalytic Water Splitting Properties of Electrochemically Generated Nickel Hydroxide Thin Films in Aqueous Alkaline Solution. In: *International Journal of Electrochemical Science*, 2012, **7**(12), 11768–11795.

118. **Hutton, L.A., Vidotti, M., Patel, A.N., Newton, M. E., Unwin, P.R., MacPherson, J.V.** Electrodeposition of Nickel Hydroxide Nanoparticles on Boron-Doped Diamond Electrodes for Oxidative Electrodes for Oxidative Electrocatalysis. In: *Journal of Physical Chemistry C*, 2011, **115**(5), 1649–1658.

119. **Cherchour, N., Deslouis, C., Messaoudi, B., Pailletet, A.** pH Sensing in Aqueous Solutions Using a MnO₂ Thin Film Electrodeposited on a Glassy Carbon Electrode. *Electrochimica Acta*, 2011, **56**(27), 9746–9755.

120. **El-Deab, M.S., Awad, M.I., Mohammad, A.M., Ohsaka, T.** Enhanced Water Electrolysis: Electrocatalytic Generation of Oxygen Gas at Manganese Oxide Nanorods Modified Electrodes. In: *Electrochemistry Communications*, 2007, **9**(8), 2082–2087.

121. **Kanan, M.W., Nocera, D.G.** *In Situ* Formation of an Oxygen-Evolving Catalyst in Neutral Water Containing Phosphate and Co²⁺. In: *Science*, 2008, **321**, 1072–1075.

122. **Galan-Mascaros, J.R.** Water Oxidation at Electrodes Modified with Earth-Abundant Transition-Metal Catalysts. In: *Chemelectrochem*, 2015, **2**(1), 37–50.

123. **Lutterman, D.A., Surendranath, Y., Nocera, D.G.** A Self-Healing Oxygen-Evolving Catalyst. In: *Journal of American Chemical Society*, 2009, **131**(11), 3838–3839.

124. **He, J.F., Peng, Y.H., Sun, Z.H., Cheng, W.R., Liu, Q.H., Feng, Y.J., Jiang, Y., Hu, F.C., Pan, Z.Y., Bian, Q., Wei, S.Q.** Realizing High Water Splitting Activity on Co₃O₄ Nanowire Arrays under Neutral Environment. In: *Electrochimica Acta*, 2014, **119**, 64–71.

125. **Surendranath, Y., Kanan, M.W., Nocera, D.G.** Mechanistic Studies of the Oxygen Evolution Reaction by a Cobalt-Phosphate Catalyst at Neutral pH. In: *Journal of the American Chemical Society*, 2010, **132**(46), 16501–16509.

126. **Kanan, M.W., Yano, J., Surendranath, Y., Dinca, M., Yachandra, V.K., Nocera, D.G.** Structure and Valency of a Cobalt-Phosphate Water Oxidation Catalyst Determined by *In Situ* X-ray Spectroscopy. In: *Journal of the American Chemical Society*, 2010, **132**(39), 13692–13701.

127. **Grzelczak, M., Zhang, J., Pfrommer, J., Hartmann, J., Dress, M., Antonietti, M., Wang, X.** Electro- and Photochemical Water Oxidation on Ligand-Free Co₃O₄ Nanoparticles with Tunable Sizes. In: *ACS Catalysis*, 2013, **3**(3), 383–388.

128. **Zhang, Y., Cui, B., Yao, Z., Qin, Z., Deng, X., Li, J., Lin, H.** Hierarchical Cobalt-Based Hydroxide Microspheres for Water Oxidation. In: *Nanoscale*, 2014, **6**(6), 3376–3383.
129. **Marsh, D.A., Yan, W.B., Liu, Y., Hemminger, J.C., Penner, R.M., Borovik, A.S.** Water Oxidation Using a Cobalt Monolayer Prepared by Underpotential Deposition. In: *Langmuir*, 2013, **29**(47), 14728–14732.
130. **Dinca, M., Surendranath, Y., Nocera, D.G.** Nickel-Borate Oxygen-Evolving Catalyst that Functions under Benign Conditions. In: *Proceedings of the National Academy of Science*, 2010, **107**(23), 10337–10341.
131. **Bediako, D.K., Surendranath, Y., Nocera, D.G.** Mechanistic Studies of the Oxygen Evolution Reaction Mediated by a Nickel-Borate Thin Film Electrocatalyst. In: *Journal of the American Chemical Society*, 2013, **135**(9), 3662–3674.
132. **Lyons, M.E.G., Doyle, R.L., Godwin, I., O'Brien, P., Russel, L.** Hydrous Nickel Oxide: Redox Switching and the Oxygen Evolution Reaction in Aqueous Alkaline Solution. In: *Journal of Electrochemical Society*, 2012, **159**(12), H932–H944.
133. **Gao, M., Sheng, W., Zhuang, Z., Fang, Q., Gu, S., Jiang, J., Yan, Y.** Efficient Water Oxidation Using Nanostructured a-nickel Hydroxide as an Electrocatalyst. In: *Journal of the American Chemical Society*, 2014, **136**(19), 7077–7084.
134. **Yagi, S., Yamada, I., Tsukasaki, H., Seno, A., Murakami, M., Fujiji, H., Chen, H., Umezawa, N., Abe, H., Nishiyama, N., Mori, S.** Covalency-Reinforced Oxygen Evolution Reaction Catalyst. In: *Nature Communications*, 2015, **6**, 8249.
135. **Zhu, Y., Zhou, W., Yu, J., Chen, Y., Liu, M., Shao, Z.** Enhancing Electrocatalytic Activity of Perovskite Oxides by Tuning Cation Deficiency for Oxygen Reduction and Evolution Reactions. In: *Chemistry of Materials*, 2016, **28**(6), 1691–1697.
136. **Li, M., Xiong, Y., Liu, X., Bo, X., Zhang, Y., Han, C., Guo, L.** Facile Synthesis of Electrospun MFe_2O_4 ($M=Co, Ni, Cu, Mn$) Spinel Nanofibers with Excellent Electrocatalytic Properties for Oxygen Evolution and Hydrogen Peroxide Reduction. In: *Nanoscale*, 2015, **7**(19), 8920–8930.
137. **Chen, Z., Kronawitter, C.X., Koel, B.E.** Facet-Dependent Activity and Stability of Co_3O_4 Nanocrystals towards the Oxygen Evolution Reaction. In: *Physical Chemistry Chemical Physics*, 2015, **17**(43), 29387–29393.
138. **Lu, Z., Wang, H., Kong, D., Yan, K., Hsu, P.C., Zheng, G., Yao, H., Liang, Z., Sun, X., Cui, Y.** Electrochemical Tuning of Layered Lithium Transition Metal Oxides for Improvement of Oxygen Evolution Reaction. In: *Nature Communications*, 2014, **5**, 4345.
139. **Jiang, J., Li, Y., Liu, J., Huang, X., Yuan, C., Lou, X.W.** Recent Advances in Metal Oxide-Based Electrode Architecture Design for Electrochemical Energy Storage. In: *Advanced Materials*, 2012, **24**(38), 5166–5180.
140. **Yu, X., Hua, T., Liu, X., Yan, Z., Xu, P., Du, P.** Nickel-Based Thin Film on Multiwalled Carbon Nanotubes as an Efficient Bifunctional Electrocatalyst for Water Splitting. In: *ACS Applied Materials & Interfaces*, 2014, **6**(17), 15395–15402.

141. **Wu, J., Xue, Y., Yan, X., Yan, W., Cheng, Q., Xie, Y.** Co₃O₄ Nanocrystals on Single-Walled Carbon Nanotubes as a Highly Efficient Oxygen-Evolving Catalyst. In: *Nano Research*, 2012, **5**(8), 521–530.
142. **Mette, K., Bergmann, A., Tessonnier, J.P., Havecker, M., Yao, L., Ressler, T., Schlogl, R., Strasser, P., Behrens, M.** Nanostructured Manganese Oxide Supported on Carbon Nanotubes for Electrocatalytic Water Splitting. In: *ChemCatChem*, 2012, **4**(6), 851–862.
143. **Lu, X., Zhao, C.** Highly Efficient and Robust Oxygen Evolution Catalysts Achieved by Anchoring Nanocrystalline Cobalt Oxides Onto Mildly Oxidized Multiwalled Carbon Nanotubes. In: *Journal of Materials Chemistry A*, 2013, **1**(39), 12053–12059.
144. **Zhao, Y., Nakamura, R., Kamiya, K., Nakanishi, S., Hashimoto, K.** Nitrogen-Doped Carbon Nanomaterials as non-Metal Electrocatalysts for Water Oxidation. In: *Nature Communications*, 2013, Article No. 2390.
145. **Chen, Y.L., Li, J.H., Hong, Z.H., Shen, B., Lin, B.Z., Gao, B.F.** Origin of the Enhanced Visible-Light Photocatalytic Activity of CNT Modified g-C₃N₄ for H₂ Production. In: *Physical Chemistry Chemical Physics*, 2014, **16**(17), 8106–8113.
146. **Ma, T.Y., Dai, S., Jaroniec, M., Qiao, S.Z.** Graphitic Carbon Nitride Nanosheet-Carbon Nanotube Three-Dimensional Porous Composites as High-Performance Oxygen Evolution Electrocatalysts. In: *Angewandte Chemie International Edition*, 2014, **53**(28), 7281–7285.
147. **Chen, S., Duan, J., Jaroniec, M., Qiao, S.Z.** Nitrogen and Oxygen Dual-Doped Carbon Hydrogel Film as a Substrate-Free Electrode for Highly Efficient Oxygen Evolution Reaction. In: *Advanced Materials*, 2014, **26**(18), 2925–2930.
148. **Egdell, R.G., Goodenough, J.B., Hamnett, A., Naish, C.J.** Electrochemistry of Ruthenates. Part 1. – Oxygen Reduction on Pyrochlore Ruthenates. In: *Journal of the Chemical Society, Faraday Transactions 1: Physical Chemistry in Condensed Phases*, 1983, **79**(4), 893–912.
149. **Burke, L.D., Lyons, M.E.G., Whelan, D.P.** Influence of pH on the Reduction of Thick Anodic Oxide Films on Gold. In: *Journal of Electroanalytical Chemistry*, 1982, **139**(1), 131–142.
150. **Benson, P., Briggs, G.W.D., Wynne-Jones, W.F.K.** The Cobalt Hydroxide Electrode – I. Structure and Phase Transitions of the Hydroxides. In: *Electrochimica Acta*, 1964, **9**(3), 275–280.
151. **Rovetta, A.A.S., Browne, M.P., Harvey, A., Godwin, I.J., Coleman, J.N., Lyons, M.E.G.** Cobalt Hydroxide Nanoflakes and Their Application as Supercapacitors and Oxygen Evolution Catalysts. In: *Nanotechnology*, 2017, **28**, 375–401.
152. **Bockris, J.O., Otagawa, T.** Mechanism of Oxygen Evolution on Perovskites. In: *Journal of Physical Chemistry*, 1983, **87**(15), 2960–2971.
153. **Bockris, J.O., Otagawa, T.** The Electrocatalysis of Oxygen Evolution on Perovskites. In: *Journal of Electrochemical Society*, 1984, **131**(2), 290–302.
154. **Rossmesl, J., Qu, Z.W., Zhu, H., Kroes, G.J., Norskov, J.K.** Electrolysis of Water on Oxide Surfaces. In: *Journal of Electroanalytical Chemistry*, 2007, **607**(1–2), 83–89.

155. **Busch, M., Ahlberg, E., Panas, I.** Electrocatalytic Oxygen Evolution from Water on a Mn(III-V) Dimer Model Catalyst – A DTF Perspective. In: *Physical Chemistry Chemical Physics*, 2011, **13**(33), 15069–15076.
156. **Wang, L.P., Wu, Q., Van Voorhis, T.** Acid-Base Mechanism for Ruthenium Water Oxidation Catalysts. In: *Inorganic Chemistry*, 2010, **49**(10), 4543–4553.
157. **Willems, H., Kobussen, A.G.C., De Wit, J.H.W., Broers, G.H.J.** The Oxygen Evolution Reaction on Cobalt: Part I. Reaction Order Experiments and Impedance Measurements. In: *Journal of Electroanalytical Chemistry*, 1984, **170**(1–2), 227–242.
158. **Kobussen, A.G.C., Broers, G.H.J.** The Oxygen Evolution on $\text{La}_{0.5}\text{Ba}_{0.5}\text{CoO}_3$: Theoretical Impedance Behaviour for a Multi-Step Mechanism Involving Two Adsorbates. In: *Journal of Electroanalytical Chemistry*, 1981, **126**(1–3), 221–240.
159. **Pandolfo, T., Ruiz, V., Sivakkumar, S., Nerkar, J.** *General Properties of Electrochemical Capacitors*. Weinheim, Germany: Wiley-VCH Verlag GmbH & Co. KGaA, 2013.
160. **Halper, M.S., Ellenbogen, J.C.** *Supercapacitors: A Brief Overview*. Virginia, USA: The MITRE Corporation, 2006.
161. **Conway, B.** *Electrochemical Supercapacitors: Scientific Fundamentals and Technological Applications*. New York: Kluwer-Plenum, 1999.
162. **Burke, A.** Ultracapacitors: Why, How and Where Is the Technology. In: *Journal of Power Sources*, 2000, **91**(1), 37–50.
163. **Kotz, R., Carlen, M.** Principles and Applications of Electrochemical Capacitors. In: *Electrochimica Acta*, 2000, **45**(15–16), 2483–2498.
164. **Yu, A., Davies, A., Chen, Z.** *Electrochemical Supercapacitors*. Weinheim, Germany: Wiley-VCH Verlag GmbH & Co. KGaA, 2012.
165. **Okonkwo, P.C., Collins, E., Okonkwo, E.** *Application of Biopolymer Composites In Super Capacitors*. Amsterdam, the Netherlands: Elsevier, 2017.
166. **Arulepp, M., Permann, L., Leis, J., Perkson, A., Rumma, K., Janes, A., Lust, E.** Influence of the Solvent Properties on the Characteristics of a Double Layer Capacitor. In: *Journal of Power Sources*, 2004, **133**(2), 320–328.
167. **Sato, T., Masuda, G., Takagi, K.** Electrochemical Properties of Novel Ionic Liquids for Electric Double Layer Capacitor Applications. In: *Electrochimica Acta*, 2004, **49**, 3603–3611.
168. **Tsuda, T., Hussey, C.L.** Electrochemical Applications of Room-Temperature Ionic Liquids. In: *Electrochemical Society Interface*, 2007, **16**, 42–49.
169. **Sugimoto, W., Yokoshima, K., Murakami, Y., Takasu, Y.** Charge Storage Mechanism of Nanostructured Anhydrous and Hydrous Ruthenium-Based Oxides. In: *Electrochimica Acta*, 2006, **52**(4), 1742–1748.170.
170. **Zhang, J., Kong, L.B., Li, H., Luo, Y.C., Kang, L.** Synthesis of Polypyrrole Film by Pulse Galvanostatic Method and Its Application as Supercapacitor Electrode Materials. In: *Journal of Materials Science*, 2010, **45**(7), 1947–1954.
171. **Yan, J., Fan, Z., Wei, T., Qian, W., Zhang, M., Wei, F.** Fast and Reversible Surface Redox Reaction of Graphene– MnO_2 Composites as Supercapacitor Electrodes. In: *Carbon*, 2010, **48**(13), 3825–3833.
172. **Shi, F., Wang, X., Gu, C., Tu, J.** Metal Oxide/Hydroxide-Based Materials for Supercapacitors. In: *RSC Advances*, 2014, **4**, 41910–41921.

173. **Liu, S., Sun, S., You, X.Z.** Inorganic Nanostructured Materials for High Performance Electrochemical Supercapacitors. In: *Nanoscale*, 2014, **6**, 2037–2045.
174. **Wang, G., Zhang, L., Zhang, J.** A Review of Electrode Materials for Electrochemical Supercapacitors. In: *Chemical Society Reviews*, 2012, **41**, 797–828.
175. **Pang, S.C., Anderson, M.A., Chapman, T.W.** Novel Electrode Materials for Thin-Film Ultracapacitors: Comparison of Electrochemical Properties of Sol-Gel Derived and Electrodeposited Manganese Oxide. In: *Journal of Electrochemical Society*, 2000, **147**(2), 444–450.
176. **Toupin, M., Brousse, T., Belanger, D.** Charge Storage Mechanism of MnO₂ Electrode Used in Aqueous Electrochemical Capacitor. In: *Chemistry of Materials*, 2004, **16**(16), 3184–3190.
177. **Im, D., Manthiram, A.** Nanostructured Lithium Manganese Oxide Cathodes Obtained by Reducing Lithium Permanganate with Methanol. In: *Journal of Electrochemical Society*, 2002, **149**(8), A1001–A1007.
178. **Lee, H.Y., Kim, S.W., Lee, H.Y.** Expansion of Active Site Area and Improvement of Kinetic Reversibility in Electrochemical Pseudocapacitor Electrode. In: *Electrochemical and Solid-State Letters*, 2001, **4**(3), A19–A22.
179. **Broughton, J.N., Brett, M.J.** Variations in MnO₂ Electrodeposition for Electrochemical Capacitors. In: *Electrochimica Acta*, 2005, **50**(24), 4814–4819.
180. **Yoo, H.N., Park, D.H., Hwang, S.J.** Effects of Vanadium- and Iron- Doping on Crystal Morphology and Electrochemical Properties of 1D Nanostructured Manganese Oxides. In: *Journal of Power Sources*, 2008, **185**(2), 1374–1379.
181. **Ko, J.M., Kim, K.M.** Electrochemical Properties of MnO₂/Activated Carbon Nanotube Composite as an Electrode Material For Supercapacitor. In: *Materials Chemistry and Physics*, 2009, **114**(2–3), 837–841.
182. **Reddy, A.L.M., Shaijumon, M.M., Gowda, S.R., Ajayan, P.M.** Multisegmented Au-MnO₂/Carbon Nanotube Hybrid Coaxial Arrays for High-Power Supercapacitor Applications. In: *Journal of Physical Chemistry C*, 2010, **114**(1), 658–663.
183. **Deng, L., Zhu, G., Wang, J., Kang, L., Liu, Z.H., Yang, Z., Wang, Z.** Graphene-MnO₂ and Graphene Asymmetrical Electrochemical Capacitor with a High Energy Density in Aqueous Electrolyte. In: *Journal of Power Sources*, 2011, **196**(24), 10782–10787.
184. **Wang, J.G., Yang, Y., Huang, Z.H., Kang, F.** Coaxial Carbon Nanofibers/MnO₂ Nanocomposites as Freestanding Electrodes for High-Performance Electrochemical Capacitors. In: *Electrochimica Acta*, 2011, **56**(25), 9240–9247.
185. **Lang, X.Y., Yuan, H.T., Iwasa, Y., Chen, M.W.** Three-Dimensional Nanoporous Gold for Electrochemical Supercapacitors. In: *Scripta Materialia*, 2011, **64**(9), 923–926.
186. **Jaidev, Jafri, R.I., Mishra, A.K., Ramaprabhu, S.** Polyaniline-MnO₂ Nanotube Hybrid Nanocomposite as Supercapacitor Electrode Material in Acidic Electrolyte. In: *Journal of Materials Chemistry*, 2011, **21**(44), 17601–17605.
187. **Chen, W., Rakhi, R.B., Hu, L., Xie, X., Cui, Y., Alshareef, H.N.** High-Performance Nanostructured Supercapacitors on a Sponge. In: *Nano Letters*, 2011, **11**(12), 5165–5172.

188. **Cheng, J., Cao, G.P., Yang, Y.S.** Characterization of Sol-Gel-Derived NiO_x Xerogels as Supercapacitors. In: *Journal of Power Sources*, 2006, **159**, 734–741.
189. **Wu, M.S., Wang, M.J., Jow, J.J.** Fabrication of Porous Nickel Oxide Film with Open Macropores by Electrophoresis and Electrodeposition for Electrochemical Capacitors. In: *Journal of Power Sources*, 2010, **195**(12), 3950–3955.
190. **Xia, X.H., Tu, J.P., Zhang, Y.Q., Mai, Y.J., Wang, X.L., Gu, C.D., Zhao, X. B.** Three-Dimensional Porous nano-Ni/Co(OH)₂ Nanoflake Composite Film: A Pseudocapacitive Material with Superior Performance. In: *Journal of Physical Chemistry C*, 2011, **115**(45), 22662–22668.
191. **Nam, K.W., Kim, K.H., Lee, E.S., Yoon, W.S., Yang, X.Q., Ki, K.B.** Pseudocapacitive Properties of Electrochemically Prepared Nickel Oxides on 3-Dimensional Carbon Nanotube Film Substrates. In: *Journal of Power Sources*, 2008, **182**(2), 642–652.
192. **Jayashree, R.S., Kamath, P.V.** Suppression of the $\alpha \rightarrow \beta$ -nickel Hydroxide Transformation in Concentrated Alkali: Role of Dissolved Cations. In: *Journal of Applied Electrochemistry*, 2001, **31**(12), 1315–1320.
193. **Li, J.T., Zhao, W., Huang, F.Q., Manivannan, A., Wu, N.Q.** Single-Crystalline Ni(OH)₂ and NiO Nanoplatelet Arrays as Supercapacitor Electrodes. In: *Nanoscale*, 2011, **3**(12), 5103–5109.
194. **Patil, U.M., Gurav, K.V., Fulari, V.J., Lokhande, C.D., Joo, O.S.** Characterization of Honeycomb-Like “ β -Ni(OH)₂” Thin Films Synthesized by Chemical Bath Deposition Method and Their Supercapacitor Application. In: *Journal of Power Sources*, 2009, **188**(1), 338–342.
195. **Ren, Y., Gao, L.A.** From Three-Dimensional Flower-Like α -Ni(OH)₂ Nanostructures to Hierarchical Porous NiO Nanoflowers: Microwave-Assisted Fabrication and Supercapacitor Properties. In: *Journal of the American Ceramic Society*, 2010, **93**(11), 3560–3564.
196. **Du, H.M., Jiao, L.F., Cao, K.Z., Wang, Y.J., Yuan, H.T.** Polyol-Mediated Synthesis of Mesoporous α -Ni(OH)₂ with Enhanced Supercapacitance. In: *ACS Applied Materials & Interfaces*, 2013, **5**(14), 6643–6648.
197. **Yang, G.W., Xu, C.L., Li, H.L.** Electrodeposited Nickel Hydroxide on Nickel Foam with Ultrahigh Capacity. In: *Chemical Communications*, 2008, **48**, 6537–6539.
198. **Wang, H.L., Casalongue, H.S., Liang, Y.Y., Dai, H.J.** Ni(OH)₂ Nanoplates Grown on Graphene as Advanced Electrochemical Pseudocapacitor Materials. In: *Journal of the American Chemical Society*, 2010, **132**(21), 7472–7477.
199. **Chen, S., Zhu, J.W., Zhou, H., Wang, X.** One-Step Synthesis of Low Density Carbon Nanotube-Doped Ni(OH)₂ Nanosheets with Improved Electrochemical Performances. In: *RSC Advances*, 2011, **1**(3), 484–489.
200. **Srinivasan, V., Weidner, J.W.** Capacitance Studies of Cobalt Oxide Films Formed via Electrochemical Precipitation. In: *Journal of Power Sources*, 2002, **108**(1–2), 15–20.
201. **Liu, T.C., Pell, W.G., Conway, B.E.** Stages in the Development of Thick Cobalt Oxide Films Exhibiting Reversible Redox Behavior and Pseudocapacitance. In: *Electrochimica Acta*, 1999, **44**(17), 2829–2842.

202. **Zhang, Y.Q., Li, L., Shi, S.J., Xiong, Q.Q., Zhao, X.Y., Wang, X.L., Gu, C.D., Tu, J. P.** Synthesis of Porous Co_3O_4 Nanoflake Array and Its Temperature Behavior as Pseudo-Capacitor Electrode. In: *Journal of Power Sources*, 2014, **256**, 200–205.
203. **Yang, Q., Lu, Z.Y., Chang, Z., Zhu, W., Sun, J.Q., Liu, J.F., Sun, X.M., Duan, X.** Hierarchical Co_3O_4 Nanosheet@nanowire Arrays with Enhanced Pseudocapacitive Performance. In: *RSC Advances*, 2012, **2**(4), 1663–1668.
204. **Xia, X.H., Tu, J.P., Zhang, Y.Q., Mai, Y.J., Wang, X.L., Gu, C.D., Zhao, X.B.** Freestanding Co_3O_4 Nanowire Array for High Performance Supercapacitors. In: *RSC Advances*, 2012, **2**(5), 1835–1841.
205. **Wang, H., Holt, C.M., Li, Z., Tan, X., Amirkhiz, B.S., Xu, Z., Olsen, B.C., Stephenson, T., Mitlin, D.** Graphene-Nickel Cobaltite Nanocomposite Asymmetrical Supercapacitor with Commercial Level Mass Loading. In: *Nano Research*, 2012, **5**(9), 605–617.
206. **Yuan, C.Z., Yang, L., Hou, L.R., Shen, L.F., Zhang, X.G., Lou, X.W.** Growth of Ultrathin Mesoporous Co_3O_4 Nanosheet Arrays on Ni Foam for High-Performance Electrochemical Capacitors. In: *Energy & Environmental Science*, 2012, **5**(7), 7883–7887.
207. **Zhang, F., Yuan, C.Z., Lu, X.J., Zhang, L.J., Che, Q., Zhang, X.G.** Facile Growth of Mesoporous Co_3O_4 Nanowire Arrays on Ni Foam for High Performance Electrochemical Capacitors. In: *Journal of Power Sources*, 2012, **203**, 250–256.
208. **Ren, X.H., Fan, H.Q., Ma, J.W., Wang, C., Zhang, M.C., Zhao, N.** Hierarchical Co_3O_4 /PANI Hollow Nanocages: Synthesis and Application for Electrode Materials of Supercapacitors. In: *Applied Surface Science*, 2018, **441**, 194–203.
209. **Xu, J., Gao, L., Cao, J.Y., Wang, W.C., Chen, Z.D.** Preparation and Electrochemical Capacitance of Cobalt Oxide (Co_3O_4) Nanotubes as Supercapacitor Material. In: *Electrochimica Acta*, 2010, **56**(2), 732–736.
210. **Gupta, V., Gupta, S., Miura, N.** Al-Substituted α -cobalt Hydroxide Synthesized by Potentiostatic Deposition Method as an Electrode Material for Redox-Supercapacitors. In: *Journal of Power Sources*, 2008, **177**(2), 685–689.
211. **Zhou, W.J., Xu, M.W., Zhao, D.D., Xu, C.L., Li, H.L.** Electrodeposition and Characterization of Ordered Mesoporous Cobalt Hydroxide Films on Different Substrates for Supercapacitors. In: *Microporous and Mesoporous Materials*, 2009, **117**(1–2), 55–60.
212. **Jagdale, A.D., Jamadade, V.S., Pusawale, S.N., Lokhande, C.D.** Effect of Scan Rate on the Morphology of Potentiodynamically Deposited $\text{b-Co}(\text{OH})_2$ and Corresponding Supercapacitive Performance. In: *Electrochimica Acta*, 2012, **78**, 92–97.
213. **Frackowiak, E., Jurewicz, K., Lota, K., Beguin, F.** Supercapacitors Based on Conducting Polymers/Nanotubes Composites. In: *Journal of Power Sources*, 2006, **153**(2), 413–418.
214. **Frackowiak, E.** *Electrode Materials with Pseudocapacitive Properties*. Weinheim, Germany: Wiley-VCH Verlag GmbH & Co. KGaA, 2013.

215. **Khomenko, V., Frackowiak, E., Beguin, F.** Determination of the Specific Capacitance of Conducting Polymer/Nanotubes Composite Electrodes Using Different Cell Configurations. In: *Electrochimica Acta*, 2005, **50**(12), 2499–2506.
216. **Wang, H., Has, Q., Yang, X., Lu, L., Wang, X.** Graphene Oxide Doped Polyaniline for Supercapacitors. In: *Electrochemistry Communications*, 2009, **11**(6), 1158–1161.
217. **Schultz, B., Diesel, B., Orgzall, I., Diez, I., Xu, C.** Aspects of Morphology Control during the Oxidative Synthesis of Electrically Conducting Polymers. In: *High Performance Polymers*, 2009, **21**(5), 633–652.
218. **Fang, Y., Liu, J., Yu, D.J., Wicksted, J.P., Kalkan, K., Topal, C.O., Flanders, B.N., Wu, J., Li, J.** Self-Supported Supercapacitor Membranes: Polypyrrole-Coated Carbon Nanotube Networks Enabled by Pulsed Electrodeposition. In: *Journal of Power Sources*, 2010, **195**(2), 674–679.
219. **Mujawar, S.H., Ambade, S.B., Battumur, T., Ambade, R.B., Lee, S.H.** PANI Nanotubes on a Titanium Nanotube Template Using Electrochemical Polymerization. In: *Electrochimica Acta*, 2011, **56**(12), 4462–4466.
220. **Zhan, H., Cao, G., Wang, Z., Yang, Y., Shi, Z., Gu, Z.** Tube-Covering-Tube Nanostructured Polyaniline/Carbon Nanotube Array Composite Electrode with High Capacitance and Superior Rate Performance as well as Good Cycling Stability. In: *Electrochemistry Communications*, 2008, **10**(7), 1056–1059.
221. **Yuan, C., Zhang, X., Gao, B., Li, J.** Synthesis and Electrochemical Capacitance of Mesoporous $\text{Co}(\text{OH})_2$. In: *Materials Chemistry and Physics*, 2007, **101**(1), 148–152.
222. **Taberna, P., Simon, P.** *Electrochemical Techniques*. Weinheim, Germany: Wiley-VCH Verlag GmbH & Co. KGaA, 2013.
223. **Gupta, V., Kusahara, T., Toyama, H., Gupta, S., Miura, N.** Potentiostatically Deposited Nanostructured $\alpha\text{-Co}(\text{OH})_2$: A High Performance Electrode Material for Redox-Capacitors. In: *Electrochemistry Communications*, 2007, **9**(9), 2315–2319.
224. **Baciu, A., Remes, A., Ilinoiu, E., Manea, F., Picken, S.J., Schoonman, J.** Carbon Nanotubes Composite for Environmentally Friendly Sensing. In: *Environmental Engineering and Management Journal*, 2012, **11**(2), 239–246.
225. **Fotouhi, L., Fatollahzadeh, M., Heravi, M.M.** Electrochemical Behavior and Voltammetric Determination of Sulfaguanidine at a Glassy Carbon Electrode Modified with a Multi-Walled Carbon Nanotube. In: *International Journal of Electrochemical Science*, 2012, **7**(5), 3919–3928.
226. **Zhang, J., Gao, L.** Synthesis of Highly Dispersed Platinum Nanoparticles on Multiwalled Carbon Nanotubes and Their Electrocatalytic Activity toward Hydrogen Peroxide. In: *Journal of Alloys and Compounds*, 2010, **505**(2), 604–608.
227. **Liu, P.F., Yang, S., Zheng, L.R., Zhang, B., Yang, H.G.** Electrochemical Etching of α -cobalt Hydroxide for Improvement of Oxygen Evolution Reaction. In: *Journal of Materials Chemistry A*, 2016, **4**, 9578–9584.
228. **Qorbani, M., Naseri, N., Moshfegh, A.Z.** Hierarchical $\text{Co}_3\text{O}_4/\text{Co}(\text{OH})_2$ Nanoflakes as a Supercapacitor Electrode: Experimental and Semi-Empirical Model. In: *ACS Applied Materials & Interfaces*, 2015, **7**(21), 11172–11179.

229. **Gholivand, M.B., Shamsipur, M., Shamizadeh, M., Moradian, R., Asrinchap, B.** Cobalt Oxide Nanoparticles as a Novel High-Efficiency Fiber Coating for Solid Phase Microextraction of Benzene, Toluene, Ethylbenzene and Xylene from Aqueous Solutions. In: *Analytica Chimica Acta*, 2014, **822**, 30–36.
230. **Yuranov, I., Kiwi-Minsker, L., Renken, A.** Structured Combustion Catalysts Based on Sintered Metal Fibre Filters. In: *Applied Catalysis B: Environmental*, 2003, **43**(3), 217–227.
231. **Yang, W., Gao, Z., Ma, J., Wang, J., Zhang, X., Liu, L.** Two-Step Electrodeposition Construction of Flower-on-Sheet Hierarchical Cobalt Hydroxide Nano-Forest for High-Capacitance Supercapacitors. In: *Dalton Transactions*, 2013, **42**, 15706–15715.
232. **Delmas, C., Foussier, C., Hagenmuller, P., Ackerman, J.F.** *The Alkali Ternary Oxides A_xCoO_2 and A_xCrO_2 ($A=Na,K$)*. USA: John Wiley & Sons, 1983.
233. **Trasatti, S., Petrii, O.A.** Real Surface Area Measurements in Electrochemistry. In: *Pure and Applied Chemistry*, 1991, **63**(5), 711–734.
234. **Hutchings, G.S., Zhang, Y., Li, J., Yonemoto, B.T., Zhou, X., Zhu, K., Jiao, F.** *In Situ* Formation of Cobalt Oxide Nanocubanes as Efficient Oxygen Evolution Catalysts. In: *Journal of the American Chemical Society*, 2015, **137**(12), 4223–4229.
235. **Menezes, P.W., Indra, A., Gonzalez-Flores, D., Sahraie, N.R., Zaharieva, I., Schwarze, M., Strasser, P., Dau, H., Driess, M.** High-Performance Oxygen Redox Catalysis with Multifunctional Cobalt Oxide Nanochains: Morphology-Dependent Activity. In: *ACS Catalysis*, 2015, **5**(4), 2017–2027.
236. **Raouf, J.B., Chekin, F., Ehsani, V.** Cobalt Oxide Nanoparticle-Modified Carbon Nanotubes as an Electrocatalysts for Electrocatalytic Evolution of Oxygen Gas. In: *Bulletin of Materials Science*, 2015, **38**(1), 135–140.
237. **Yu, J., Chen, G., Sunarso, J., Zhu, Y., Ran, R., Zhu, Z., Zhou, W., Shao, Z.** Cobalt Oxide and Cobalt-Graphitic Carbon Core-Shell Based Catalysts with Remarkably High Oxygen Reduction Reaction Activity. In: *Advanced Science*, 2016, **3**, Article No.1600060.
238. **Zhang, Y., Ding, F., Deng, C., Zhen, S., Li, X., Xue, Y., Yan, Y.M., Sun, K.** Crystal Plane-Dependent Electrocatalytic Activity of Co_3O_4 toward Oxygen Evolution Reaction. In: *Catalysis Communications*, 2015, **67**, 78–82.
239. **Ghanem, M.A., Al-Mayouf, A.M., Arunachalam, P., Abiti, T.** Mesoporous Cobalt Hydroxide Prepared Using Liquid Crystal Template for Efficient Oxygen Evolution in Alkaline Media. In: *Electrochimica Acta*, 2016, **207**, 177–186.
240. **Chen, Z., Chen, Y., Zuo, C., Zhou, S., Xiao, A.G., Pan, A.X.** Hydrothermal Synthesis of Porous $Co(OH)_2$ Nanoflake Array Film and Its Supercapacitor Application. In: *Bulletin of Materials Science*, 2013, **36**(2), 239–244.
241. **Spataru, N., Terashima, C., Tokuhira, K., Sutanto, I., Tryk, D.A., Park, S.M., Fujishima, A.** Electrochemical Behavior of Cobalt Oxide Films Deposited at Conductive Diamond Electrodes. In: *Journal of the Electrochemical Society*, 2003, **150**, E337–E341.
242. **Doyle, R.L., Lyons, M.E.G.** *The Oxygen Evolution Reaction: Mechanistic Concepts and Catalyst Design*. Switzerland: Springer International Publishing, 2016.

243. **Suen, N.T., Hung, S.F., Quan, Q., Zhang, N., Xu, Y.J., Chen, H.M.** Electrocatalysis for the Oxygen Evolution Reaction: Recent Development and Future Perspectives. In: *Chem. Soc. Rev.*, 2017, **46**, 337–365.
244. **Ramsundar, R.M., Debgupta, J., Pillai, V.K., Joy, P.A.** Co_3O_4 Nanorods-Efficient non-Noble Metal Electrocatalyst for Oxygen Evolution at Neutral pH. In: *Electrocatalysis*, 2015, **6**(4), 331–340.
245. **Bikkarolla, S.K., Papakonstantinou, P.** CuCo_2O_4 Nanoparticles on Nitrogenated Graphene as Highly Efficient Oxygen Evolution Catalyst. In: *Journal of Power Sources*, 2015, **281**, 243–251.
246. **Jin, H., Wang, J., Su, D., Wei, Z., Pang, Z., Wang, Y.** *In Situ* Cobalt-Cobalt Oxide/N-Doped Carbon Hybrids as Superior Bifunctional Electrocatalysts for Hydrogen and Oxygen Evolution. In: *Journal of the American Chemical Society*, 2015, **137**(7), 2688–2694.
247. **Ju, H., Li, Z., Xu, Y.** Electro-Catalytic Activity of Ni–Co-Based Catalysts for Oxygen Evolution Reaction. In: *Materials Research Bulletin*, 2015, **64**, 171–174.
248. **Du, J., Chen, C., Cheng, F., Chen, J.** Rapid Synthesis and Efficient Electrocatalytic Oxygen Reduction/Evolution Reaction of CoMn_2O_4 Nanodots Supported on Graphene. In: *Inorganic Chemistry*, 2015, **54**(11), 5467–5474.
249. **Cady, C.W., Gardner, G., Maron, Z.O., Retuerto, M., Go, Y.B., Segan, S., Greenblat, M., Dismukes, G.C.** Tuning the Electrocatalytic Water Oxidation Properties of AB_2O_4 Spinel Nanocrystals: A (Li, Mg, Zn) and B (Mn, Co) Site Variants of LiMn_2O_4 . In: *ACS Catalysis*, 2015, **5**(6), 3403–3410.
250. **Hu, H., Guan, B., Xia, B., Lou, X.W.** Designed Formation of $\text{Co}_3\text{O}_4/\text{NiCo}_2\text{O}_4$ Double-Shell Nanocages with Enhanced Pseudocapacitive and Electrocatalytic Properties. In: *Journal of the American Chemical Society*, 2015, **137**(16), 5590–5595.
251. **Jang, D.M., Kwak, I.H., Kwon, E.L., Jung, C.S., Im, H.S., Park, K., Park, J.** Transition-Metal Doping of Oxide Nanocrystals for Enhanced Catalytic Oxygen Evolution. In: *Journal of Physical Chemistry C*, 2015, **119**(4), 1921–1927.
252. **Zhu, Q., Lin, L., Jiang, Y.F., Xie, X., Yuan, C.Z., Xu, A.W.** Carbon Nanotube/S–N–C Nanohybrids as High Performance Bifunctional Electrocatalysts for both Oxygen Reduction and Evolution Reactions. In: *New Journal of Chemistry*, 2015, **39**(8), 6289–6296.
253. **Chen, H., Cong, T.N., Yang, W., Tan, C., Li, Y., Ding, Y.** Progress in Electrical Energy Storage System: A Critical Review. In: *Progress in Natural Science*, 2009, **19**, 291–312.
254. **Lokhande, C.D., Dubal, D.P., Joo, O.S.** Metal Oxide Thin Film Based Supercapacitors. In: *Current Applied Physics*, 2011, **11**, 255–270.
255. **Yadav, A.A., Chavan, U.J.** Electrochemical Supercapacitive Performance of Spray Deposited Co_3O_4 Thin Film Nanostructures. In: *Electrochimica Acta*, 2017, **232**, 370–376.
256. **Cussler, E.L.** *Diffusion: Mass Transfer in Fluid Systems*. Cambridge: Cambridge University Press, 2009.
257. **Liao, Q., Li, N., Jin, S., Yang, G., Wang, C.** All-Solid-State Symmetric Supercapacitor Based on Co_3O_4 Nanoparticles on Vertically Aligned Graphene. In: *ACS Nano*, 2015, **9**(5), 5310–5317.

258. **Chen, Z., Cai, L., Yang, X., Kronawitter, C., Guo, L., Shen, S., Koel, B.E.** Reversible Structural Evolution of NiCoO_xH_y during the Oxygen Evolution Reaction and Identification of the Catalytically Active Phase. In: *ACS Catalysis*, 2018, **8**(2), 1238–1247.
259. **Jayashree, R.S., Vishnu Kamath, P.** Nickel Hydroxide Electrodeposition from Nickel Nitrate Solutions: Mechanistic Studies. In: *Journal of Power Sources*, 2001, **93**, 273–278.
260. **Pauporte, T., Mendoza, L., Cassir, M., Bernard, M.C., Chivot, J.** Direct Low-Temperature Deposition of Crystallized CoOOH Films by Potentiostatic Electrolysis. In: *Journal of the Electrochemical Society*, 2005, **152**(2), C49–C53.
261. **Jayashree, R.S., Vishnu Kamath, P.** Factors Governing the Electrochemical Synthesis of a-nickel (II) Hydroxide. In: *Journal of Applied Electrochemistry*, 1999, **29**, p. 449–454.
262. **Raveau, B., Seikh, M.** *Cobalt Oxides: From Crystal Chemistry to Physics*. Heidelberg, Germany: Wiley-VCH Verlag GmbH & Co. KGaA, 2012.
263. **Kuang, W., Wu, X., Han, E.H.** The Oxidation Behaviour of 304 Stainless Steel in Oxygenated High Temperature Water. In: *Corrosion Science*, 2010, **52**, 4081–4087.
264. **Li, D., Yu, F., Yu, Z., Sun, X., Li, Y.** Three-Dimensional Flower-like Co(OH)₂ Microspheres of Nanoflakes/Nanorods Assembled on Nickel Foam as Binder-Free Electrodes for High Performance Supercapacitors. In: *Materials Letters*, 2015, **158**, 17–20.
265. **Li, Y., Qiu, W., Qin, F., Fang, H., Hadjiev, V.G., Litvinov, D., Bao, J.** Identification of Cobalt Oxides with Raman Scattering and Fourier Transform Infrared Spectroscopy. In: *Journal of Physical Chemistry C*, 2016, **120**, 4511–4516.
266. **Hadjiev, V.G., Iliev, M.N., Vergilov, I.V.** The Raman Spectra of Co₃O₄. In: *Journal of Physics C: Solid State Physics*, 1988, **21**, L199–L201.
267. **He, X., Song, X., Qiao, W., Li, Z., Zhang, X., Yan, S., Zhong, W., Du, Y.** Phase- and Size-Dependent Optical and Magnetic Properties of CoO Nanoparticles. In: *Journal of Physical Chemistry C*, 2015, **119**, 9550–9559.
268. **Chuminjak, Y., Daothong, S., Kuntarug, A., Phokharatkul, D., Horprathum, M., Wisitsoraat, A., Tuantranont, A., Jakmunee, J., Singjai, P.** High-Performance Electrochemical Energy Storage Electrodes Based on Nickel Oxide-Coated Nickel Foam Prepared by Sparking Method. In: *Electrochimica Acta*, 2017, **238**, 298–309.
269. **Mironova-Ulmane, N., Kuzmin, A., Steins, I., Grabis, J., Sildos, I., Pars, M.** Raman Scattering in Nanosized Nickel Oxide NiO. In: *Journal of Physics: Conference Series*, 2007, **93**, 1–5.
270. **Windish Jr., C.F., Exarhos, G.J., Ferris, K.F., Engelhard, M.H., Stewart, D.C.** Infrared Transparent Spinel Films with p-Type Conductivity. In: *Thin Solid Films*, 2001, **398–399**, 45–52.
271. **Umeshbabu, E., Rajeshkhanna, G., Justin, P.J., Ranga Rao, G.** Magnetic, Optical and Electrocatalytic Properties of Urchin and Sheaf-Like NiCo₂O₄ Nanostructures. In: *Materials Chemistry and Physics*, 2015, **165**, 235–244.

272. **Zhao, D., Zhou, W., Li, H.** Effects of Deposition Potential and Anneal Temperature on the Hexagonal Nanoporous Nickel Hydroxide Films. In: *Chemistry of Materials*, 2007, **19**, 3882–3891.
273. **Chanda, D., Hnat, J., Bystron, T., Paidar, M., Bouzek, K.** Optimization of Synthesis of the Nickel-Cobalt Oxide Based Anode Electrocatalyst and of the Related Membrane-Electrode Assembly for Alkaline Water Electrolysis. In: *Journal of Power Sources*, 2017, **347**, 247–258.
274. **Iliev, M.N., Silwal, P., Loukya, B., Datta, R., Kim, D.H., Todorov, N.D., Pachauri, N., Gupta, A.** Raman Studies of Cation Distribution and Thermal Stability of Epitaxial Spinel NiCo₂O₄ Films. In: *Journal of Applied Physics*, 2013, **114**, Article No. 033514.
275. **Alsabet, M., Grden, M., Jerkiewicz, G.** Electrochemical Growth of Surface Oxides on Nickel. Part 3: Formation of β -NiOOH in Relation to the Polarization Potential, Polarization Time, and Temperature. In: *Electrocatalysis*, 2015, **6**, p. 60–71.
276. **Fabbri, E., Habereeder, A., Waltar, K., Kötzer, R., Schmidt, T.J.** Developments and Perspectives of Oxide-Based Catalysts for the Oxygen Evolution Reaction. In: *Catalysis Science & Technology*, 2014, **4**, 3800–3821.
277. **Trotochaud, L., Ranney, J.K., Williams, K.N., Boettcher, S.W.** Solution-Cast Metal Oxide Thin Film Electrocatalysts for Oxygen Evolution. In: *Journal of the American Chemical Society*, 2012, **134**, 17253–17261.
278. **Smith, R.D.L., Prevot, M.S., Fagan, R.D., Trudel, S., Berlinguette, C.P.** Water Oxidation Catalysis: Electrocatalytic Response to Metal Stoichiometry in Amorphous Metal Oxide Films Containing Iron, Cobalt, and Nickel. In: *Journal of American Chemical Society*, 2013, **135**(31), 11580–11586.
279. **Song, F., Hu, X.** Exfoliation of Layered Double Hydroxides for Enhanced Oxygen Evolution Catalysis. In: *Nature Communications*, 2014, **5**, 1–9.
280. **Shinagawa, T., Garcia-Esparza, A.T., Takahashi, K.** Insight on Tafel Slopes from a Microkinetic Analysis of Aqueous Electrocatalysis for Energy Conversion. In: *Scientific Reports*, 2015, **5**, Article No. 13801.
281. **Gualdron-Reyes, A.F., Dominguez-Velez, V., Morales-Morales, J.A., Cabanzo, R., Melendez, A.M.** Effect of Substrate Nature on the Electrochemical Deposition of Calcium-Deficient Hydroxyapatites. In: *Journal of Physics: Conference series*, 2017, **786**(012030),
282. **Liu, C., Yu, Z., Neff, D., Zhamu, A., Jang, B.Z.** Graphene-Based Supercapacitor with an Ultrahigh Energy Density. In: *Nano Letters*, 2010, **10**, 4863–4868.
283. **Dubal, D.P., Holze, R., Gomez-Romero, P.** Development of Hybrid Materials Based On Sponge Supported Reduced Graphene Oxide and Transition Metal Hydroxides for Hybrid Energy Storage Devices. In: *Scientific Reports*, 2014, **4**, 7349.
284. **Pell, W.G., Conway, B.E.** Peculiarities and Requirements of Asymmetric Capacitor Devices Based on Combination of Capacitor and Battery-Type Electrodes. In: *Journal of Power Sources*, 2004, **136**, 334–345.

LIST OF PUBLICATIONS AND PROCEEDINGS ON THE THEME OF DISSERTATION

Publications corresponding to the list of *Clarivate Analytics Web of Science* database

1. [S2; DE] Barauskienė, Ieva; Valatka, Eugenijus. Electrocatalytic and pseudocapacitive properties of cobalt (hydro)oxide films on sintered metal fiber filter // *Materials for Renewable and Sustainable Energy*. Berlin: Springer. ISSN 2194-1459. eISSN 2194-1467. 2018, Vol. 7, iss. 1, article 1, p. 1–10. DOI: 10.1007/s40243-017-0108-2. [Emerging Sources Citation Index (Web of Science); Scopus] [CiteScore: 1.93, SNIP: 0.740, SJR: 0.535 (2016, Scopus JM)] [FOR: 03P] [Contribution: 0.500]
2. [S1; PL] Barauskienė, Ieva; Valatka, Eugenijus. Synthesis, structure and capacitive properties of cobalt hydroxide films on stainless steel substrates // *Central European journal of chemistry*. Warsaw: De Gruyter Open. ISSN 1895-1066. 2014, vol. 12, iss. 11, p. 1206–1211. DOI: 10.2478/s11532-014-0570-y. [SpringerLink; Science Citation Index Expanded (Web of Science)] [CiteScore: 1.13, SNIP: 0.643, SJR: 0.348 (2014, Scopus JM)] [FOR: 03P] [Contribution: 0.500]

Publications in Proceedings of Conferences

1. [P1e; LT] Barauskienė, Ieva; Valatka, Eugenijus. Comparison of structure and capacitive behavior of cobalt(II) hydroxide films on stainless steel substrates from different electrolytes // *Chemistry and chemical technology: proceedings of the international conference, 25 April, 2014 / Kaunas University of Technology*. Kaunas: Technologija. ISSN 2351-5643. 2014, p. 159–162. [FOR: 03P] [Contribution: 0.500]
2. [T1e; LT] Barauskienė, Ieva; Valatka, Eugenijus. Synthesis and pseudocapacitive behaviour of porous cobalt hydroxide films on stainless steel mesh // *EcoBalt 2013: 18th international scientific conference, October 25-27, 2013 Vilnius, Lithuania : book of abstracts*. Vilnius: Vilniaus universiteto leidykla, 2013. ISBN 9786094592416, p. 75. [M.kr.: 03P] [Contribution: 0,500]
3. [P1e; LT] Barauskienė, Ieva; Valatka, Eugenijus. Structure and capacitive characteristics of cobalt hydroxide films on stainless steel substrates // *Chemistry and chemical technology of inorganic materials: proceedings of scientific conference chemistry and chemical technology / Kaunas University of Technology*. Kaunas: Technologija. ISSN 2029-9222. 2012, p. 85-89. [Contribution: 0,500]

SL344. 2018-12-03, 14,75 leidyb. apsk. 1. Tiražas 12 egz. Užsakymas 314.
Išleido Kauno technologijos universitetas, K. Donelaičio g. 73, 44249 Kaunas
Spausdino leidyklos „Technologija“ spaustuvė, Studentų g. 54, 51424 Kaunas